

University of Alberta

Design of an in situ-castable bioceramic bone tissue scaffold

by

Caitlin Micaela Guzzo

A thesis submitted to the Faculty of Graduate Studies and Research
in partial fulfilment of the requirements for the degree of

Master of Science

in

Materials Engineering

Department of Chemical and Materials Engineering

University of Alberta

© Caitlin Micaela Guzzo, 2020

Abstract

Bone defects are treated with bone grafts, replacing damaged or diseased bone tissue with either natural bone or bone substitutes. Synthetic graft materials, particularly bioactive glasses, have been developed to overcome the immunological and structural limitations of natural bone grafts. However, the success of bioactive glasses is limited by current approaches to fabrication of bioceramic scaffolds, of which no technique meets the design criteria for an ideal synthetic bone tissue scaffold; namely, formability, geometric stability, porosity, load-bearing capacity, bioactivity, and resorbability. To fulfil these design criteria, this work proposes a new approach to bioactive glass ceramic scaffold fabrication, producing an all-ceramic porous scaffold that can be cast *in situ* to repair bone defects. This ambient temperature and pressure process utilises a reaction with a liquid ceramic precursor to form a silicate-glass binder phase which consolidates bioactive glass frit. The resultant composite paste can be applied conformally to unique wound geometries before reacting with carbon dioxide gas to set into a rigid, load-bearing scaffold with an interconnected network of open pores. The effect of composition on the fulfilment of the design criteria was investigated via characterisation of the composite morphology, mechanical properties, and *in vitro* immersion response in simulated body fluid. It was shown that the composite scaffolds designed, produced, and analysed in this research fulfilled all established design criteria, signifying their potential success as bone tissue scaffolds.

Preface

Portions of the research presented in this thesis have been submitted for publication as C. M. Guzzo, J. A. Nychka “*Fabrication of a Porous and Formable Ceramic Composite Bone Tissue Scaffold at Ambient Temperature,*” Metallurgical and Materials Transactions A; and C. M. Guzzo, J. A. Nychka “*In vitro response of a porous and formable ceramic composite bone tissue scaffold,*” Journal of the Mechanical Behavior of Biomedical Materials; both manuscripts are currently under review. I, C. M. Guzzo, was responsible for conceptualisation, methodology, investigation, data collection and analysis, visualisation, and manuscript composition. J. A. Nychka was the supervisory author and was involved in conceptualisation, methodology, visualisation, funding acquisition, and manuscript composition.

Acknowledgements

First and foremost, I would like to express my appreciation to my supervisor and mentor, Dr. John Nychka, with whom I have been fortunate enough to work with since September 2016 as an undergraduate student. I have grown tremendously as a scientist under his guidance—learning about how to learn, and thinking about how to think. I am particularly thankful for his unyielding dedication to my growth and development; no superlatives can truly capture my gratitude, so instead: thank you.

I am indebted to my friends and colleagues in the mati research team for their support and suggestions over the years; many thanks to John, Jolene, Jonathan, Kalan, Kallie, Kendra, Kevin, Mary, Marzieh, Nicole, Omnath, Scott, and Terry.

I am exceptionally grateful for the knowledge and support provided by the professors, students, and technical staff that assisted me in the acquisition and analysis of characterisation data.

I would like to thank Piotr Nicewicz (Department of Mechanical Engineering) for his assistance in collecting optical particle size analysis data. I would also like to thank Dr. Michael Doschak (Faculty of Pharmacy and Pharmaceutical Sciences) for his guidance in collecting and analysing micro-CT data. I would like to thank Ereddad Kharraz (Faculty of Agricultural, Life, and Environmental Sciences) for performing gas pycnometry. I would also like to thank I would also like to thank Nathan Gerein and Guibin Ma (Department of Earth and Atmospheric Sciences) for their assistance in capturing VP-SEM images and EDX data. I would like to thank Rebecca Funk and Katie Nichols (Department of Earth and Atmospheric Sciences) for the collection of XRD data. I would also like to thank Wayne Moffat, Jennifer Jones, and Minh Tang Duc Hoang (Department of Chemistry) for conducting FTIR.

This work was supported by the Natural Sciences and Engineering Research Council of Canada (RGPIN2014-05419).

Table of Contents

List of Tables	x
List of Figures	xii
List of Symbols	xvii
List of Abbreviations	xx
Chapter One — Introduction	1
Bibliography - Chapter One	5
Chapter Two — Background and Literature Review	6
2.1 Bone Tissue Scaffolds	6
2.1.1 Synthetic Bone Tissue Scaffolds.....	7
2.2 Biomaterials	8
2.2.1 Bioceramics and Bioactive Glasses	9
2.2.1.1 <i>Mechanisms of Bioactivity in Bioactive Glass</i>	10
2.2.1.2 <i>Osteoconduction and Osteoinduction</i>	14
2.2.1.3 <i>Osseointegration and Osseoincorporation</i>	15
2.3 Processing of Bioactive Glasses	17
2.3.1 History of Bioactive Glass	17
2.3.2 State of the Art—Bone Tissue Scaffolds	18
2.3.2.1 <i>Sol-gel Synthesis</i>	18
2.3.2.2 <i>Foaming Methods</i>	19
2.3.2.3 <i>Porogens</i>	20

2.3.2.4 Additive Manufacturing and Fused Deposition Modelling	20
2.3.2.5 Sintering and Thermal Consolidation.....	21
2.3.2.6 Freeze-drying and Thermal Separation	21
2.3.2.7 Sponge Replication	21
2.3.2.8 Pastes and Packed Powders.....	22
2.4 Soluble Polysilicates and Sodium Silicate	22
2.4.1 Sodium Silicates in Biomedical Applications	25
2.5 Design of Synthetic Bone Tissue Scaffolds.....	26
2.5.1 Design Criteria in Literature.....	26
2.5.2 Design Criteria in This Research.....	28
Bibliography – Chapter Two	32
Chapter Three — Experimental Design.....	39
3.1 Materials.....	39
3.2 Sample Preparation	40
3.2.1 Preparation of Composite Scaffolds	40
3.2.1.1 Preparation of Optical Light Microscopy Specimens.....	46
3.2.2 Preparation of 45S5 Bioactive Glass	49
3.2.3 Preparation of Sodium Silicate.....	51
3.2.3.1 Preparation of Sodium Silicate Gas Pycnometry Specimens.....	51
3.2.3.2 Preparation of Sodium Silicate in vitro Specimens	51
3.3 Characterisation	52
3.3.1 Imaging Particle Size Analysis	53

3.3.1.1 <i>Sampling Method</i>	55
3.3.2 Sodium Silicate Reaction Kinetics	55
3.3.3 Formability and Geometric Stability Evaluation	56
3.3.4 Imaging	58
3.3.4.1 <i>Macrographs</i>	58
3.3.4.2 <i>Optical Light Microscopy</i>	58
3.3.4.3 <i>Scanning Electron Microscopy</i>	59
3.3.4.4 <i>Micro-Computed Tomography</i>	60
3.3.5 Gas Pycnometry	61
3.3.5.1 <i>Gas Pycnometry Data Analysis</i>	63
3.3.6 Mechanical Strength Testing	66
3.3.7 <i>in vitro</i> Immersion Tests	68
3.3.8 Energy-dispersive X-ray Spectroscopy.....	70
3.3.9 X-ray Diffractometry.....	71
3.3.10 Fourier Transform Infrared Spectroscopy	72
Bibliography – Chapter Three	74
Chapter Four — Results and Discussion	76
4.1 Materials Characterisation	76
4.1.1 Physical Characterisation of Bioactive Glass Frit.....	76
4.1.1.1 <i>Manual Tap Density</i>	76
4.1.1.2 <i>Optical Particle Size Analysis and Scanning Electron Microscopy</i>	76

4.1.2 Sodium Silicate Setting Reaction Kinetics	79
4.2 Formability	83
4.3 Geometric Stability	84
4.4 Porosity	87
4.4.1 Optical Light Microscopy with Epoxy Infiltration.....	87
4.4.3 Scanning Electron Microscopy	89
4.4.3 Gas Pycnometry	90
4.4.4 Micro-Computed Tomography	92
4.5 Load-Bearing Capacity	96
4.5.1 Scanning Electron Microscopy Fractography.....	100
4.6 Bioactivity.....	102
4.6.1 Macro <i>in vitro</i> Behaviour.....	102
4.6.2 Scanning Electron Microscopy with Energy-dispersive X-ray Spectroscopy	105
4.6.2.1 <i>in vitro Gel Formation</i>	114
4.6.3 X-ray Diffractometry.....	116
4.6.4 Fourier Transform Infrared Spectroscopy.....	117
4.7 Resorbability.....	120
Bibliography – Chapter Four.....	121
Chapter Five — Conclusions and Future Work.....	124
5.1 Conclusions	124
5.2 Future Work.....	129

Bibliography – Chapter Five.....	131
Bibliography.....	132
Appendix I—Sodium Silicate Characterisation	148
A1.1 Density Comparison	132
A1.2 Contact Angle Comparison.....	133
A1.3 Fourier Transform Infrared Spectroscopy Comparison	134
Bibliography – Appendix I.....	136
Appendix II—Fabrication of Specimen Moulds.....	137
A2.1 Specimen Mould A.....	137
A2.2 Specimen Mould B.....	138
A2.2.1 Choice of VPS Dental Impression Material.....	139
A2.3 Specimen Moulds C and D.....	140
Bibliography – Appendix II	141
Appendix III—Viability of <i>in vitro</i> Immersion Tests.....	142
Bibliography – Appendix III	144
Appendix IV—Specimen Surface Area Approximation	145
Bibliography – Appendix IV.....	147
Appendix V—FTIR Characterisation of <i>in vitro</i> Residue	148
Bibliography – Appendix V.....	151

List of Tables

Table 2-1. Current synthetic bone tissue scaffold processing methods evaluated against the design criteria used in this research.	31
Table 3-1. Specimen type identification and association with materials characterisation techniques.....	42
Table 3-2. Minimum residence moulding time for composites (prior to moulding). Additional time was accrued between de-moulding and mechanical testing.....	44
Table 3-3. Relationship between initial nominal wt% of aqueous sodium silicate and final vol% of set sodium silicate of the composite specimens, determined via gas pycnometry (Chapter 4.4.3).	46
Table 3-4. Design criteria, characterisation techniques, and expected outcomes used to evaluate this research.....	52
Table 3-5. Geometry of specimens used to investigate sodium silicate reaction kinetics ...	56
Table 3-6. Reagents required for preparing 1000 mL of SBF, presented in the order of addition.....	69
Table 3-7. Expected ion concentrations and pH of SBF prepared in accordance with the method developed by Kokubo and Takadama.....	70
Table 4-1. Background-corrected diameter, circularity, and convexity values for bioactive glass frit.....	77
Table 4-2. Mass loss data from sodium silicate setting kinetics and Michalis-Menten equation modelling.....	79
Table 4-3. Average 2-dimensional pore size as a function of binder phase vol%, determined via OLM.....	89
Table 4-4. Average binder coating thickness as a function of binder phase vol%, determined via OLM.....	89

Table 4-5. Composition of composite scaffolds determined by gas pycnometry.....	91
Table 4-6. Average open porosity as a function of composite composition for micro-CT investigations	93
Table 4-7. Surface area to volume ratio (SA/V) of set scaffolds as a function of binder phase, as determined by micro-CT.....	93
Table 4-8. Unconfined compressive strength of ceramic composite scaffolds as a function of binder amount.....	97
Table 4-9. pH measurements of spent SBF during <i>in vitro</i> immersion testing.	104
Table 4-10. Size of hierarchical surface features on 14 day <i>in vitro</i> specimens as a function of composition.....	109
Table 5-1. Summary evaluation of design criteria explored in this thesis.....	128
Table A1-1. Contact angle measurements and standard deviation for the old-batch aqueous sodium silicate used in this study (A) and new-batch as-received sodium silicate (B).....	133

List of Figures

Figure 1-1. Map of design criteria interdependence.	3
Figure 2-1. Ternary phase diagram of the $\text{SiO}_2\text{-CaO-Na}_2\text{O}$ system at 6 wt% P_2O_5	10
Figure 2-2. Sequence of surface reactions that take place at the bioactive glass/tissue interface.....	11
Figure 2-3. Schematic depiction of the fate of cells involved in bone repair.	15
Figure 2-4. Ternary phase diagram of the $\text{SiO}_2\text{-Na}_2\text{O-H}_2\text{O}$ system.....	23
Figure 2-5. Reaction of aqueous sodium silicate with carbon dioxide gas.	24
Figure 3-1. 45S5 bioactive glass, as (a) 12 mm diameter rods, (b) discs sectioned from rods, and (c) +355 μm frit.	40
Figure 3-2. Schematic depiction of specimen mixing technique	41
Figure 3-3. As-fabricated disc and cylinder specimens	43
Figure 3-4. Process flow diagram depicting composite specimen fabrication process.....	43
Figure 3-5. Process flow diagrams depicting the characterisation paths of (a) A-type and (b) B-type specimens.	45
Figure 3-6. Process flow diagram depicting the sample preparation of optical light microscopy specimens.	48
Figure 3-7. Bioactive glass disc mounted (centre) to polishing jig with Crystalbond 509 thermoplastic wax.....	50
Figure 3-8. Set sodium silicate specimen prepared for <i>in vitro</i> immersion tests.....	51
Figure 3-9. Schematic depiction of the minimum convex hull of a particle.....	54

Figure 3-10. (a) Oblique view of 3D-printed original positive mould and (b) plan view of custom Reprorubber negative mould from which positive composite scaffolds were fabricated to assess formability and geometric stability.....	57
Figure 3-11. Schematic depiction of a gas pycnometer	62
Figure 3-12. Kinetics data and curve fit for the mass loss during setting of bulk aqueous sodium silicate in air at 294 K (21 °C)	65
Figure 3-13. Schematic of unconfined mechanical crush testing in accordance with ASTM D7012 67.....	67
Figure 4-1. Volume-weighted size distribution of bioactive glass frit (in grey, left y-axis) overlaid with the undersize distribution (in red, right y-axis).	78
Figure 4-2. SE SEM micrograph of as-received bioactive glass frit, showing angular morphology and rough, stepped surface features indicative of cleavage fracture	78
Figure 4-3. Schematic depiction of COs gas diffusion through sodium silicate specimens in (a) droplet and (b) disc geometry, during setting in ambient conditions on an impermeable substrate (i.e. Parafilm M).....	80
Figure 4-4. Kinetics data and curve fit for the mass loss during setting of bulk aqueous sodium silicate in air at 294 K (21 °C), for droplet geometry and disc geometry	81
Figure 4-5. Schematic depiction of the ‘moving front’ of set material through bulk sodium silicate during setting in ambient conditions.....	82
Figure 4-6. Cylinder specimens (Type B) prepared using 7.4, 11.4, 16.1, and 29.4 vol% binder phase (left to right respectively).....	83
Figure 4-7. Manual compression and shearing of unset composite paste (within the manipulation time)	85
Figure 4-8. 3D printed positive mould (left); 7.4 vol% set specimens de-moulded from the mould shown in Figure A2-3b (middle); image created from superposing the set paste and	

positive mould images to highlight the different in edge profile, and geometry (right; false-coloured positive mould).....	86
Figure 4-9. Bright-field OLM images of (a) 7.4, (b) 11.4, and (c) 16.1 vol% binder composites after epoxy vacuum- infiltration.	88
Figure 4-10. Back-scattered electron (BSE) SEM micrographs of (a) 7.4, (b), 11.4, and (c) 16.1 vol% composites.....	90
Figure 4-11. Volume percent of each constituent phase in set composite scaffolds, as determined by gas pycnometry.	91
Figure 4-12. Thin-section axial micro-CT reconstructions at height fractions, h, centred at 0, 0.5, 1.0 of each specimen, illustrating the distribution of phases as a function of height and composition (black = porosity; light grey = bioactive glass frit; grey = binder).	94
Figure 4-13. Thin vertical sections of micro-CT reconstructions for the various composite compositions.	95
Figure 4-14. Digital 3D reconstructions of composite scaffold specimens.....	95
Figure 4-15. Unconfined compression strength testing data as a function of composite composition (vol% binder).	98
Figure 4-16. Inset images: time lapse photographs of 16.1 vol% binder compression specimens illustrating fracture in (a) single shear and (b) mixed failure modes.....	99
Figure 4-17. Correlation plots of UCS as a function of specimen age at testing, overlaid with best-fit linear regression (red line).	99
Figure 4-18. BSE SEM micrographs of (a) as-moulded and (b) post UCS tested (fractured) composite specimens, showing the increased extent of delamination and spallation of the binder phase that occurs after compressive failure.	101
Figure 4-19. Petri dishes with a) control and (b–d) composite scaffold specimens after 3 days <i>in vitro</i> immersion	103

Figure 4-20. Stereomicrographs of composite specimens following 14 days <i>in vitro</i> immersion.....	103
Figure 4-21. SEM BSE micrographs of <i>in vitro</i> specimens at 0, 1, 3, and 14 days immersion, at (a) low magnification and (b) high magnification.....	107
Figure 4-22. SEM-EDX element maps for the various controls and scaffolds after 14 days immersion in SBF.....	108
Figure 4-23. Schematic representation of the hierarchical structure of surface minerals as a function of binder phase, showing (a) low-binder composites and (b) high-binder composites after 14 days <i>in vitro</i> immersion.	110
Figure 4-24. Schematic depiction of composite specimen <i>in vitro</i> behaviour. 7.4, 11.4, and 16.1 indicate the vol% of binder phase in each specimen composition.	111
Figure 4-25. Bright-field OLM micrographs of (a) 7.4, (b) 11.4, and (c) 16.1 vol% binder phase specimens.	111
Figure 4-26. a) BSE SEM micrograph of a 16.1 vol% binder phase specimen after 14 days of <i>in vitro</i> immersion, depicting the difference in mineralization between the (b) inner and (c) outer specimen surfaces.....	113
Figure 4-27. Schematic of <i>in vitro</i> swelling of composite binder phase, shown (a) as moulded, before immersion; (b) immediately upon immersion, before hydration and swelling of the binder layer; and after swelling takes place in (c) low-binder and (d) high-binder composites. Insets show the path length difference for ion diffusion in (e) low-binder and (f) high-binder composites.....	113
Figure 4-28. Schematic depiction of possible gel formation mechanisms of composite specimens <i>in vitro</i> . Bioactive glass is denoted as ‘BAG’; calcium phosphate minerals are denoted as ‘CaP’. BSE SEM micrographs depict (a) single gel layer formation and (b) multiple gel layer formation.....	115
Figure 4-29. BSE SEM micrograph of a 45S5 glass frit particle within a 11.4 vol% binder composite scaffold specimen as manufactured.....	116

Figure 4-30. a) XRD patterns and b) FTIR spectra of <i>in vitro</i> specimens illustrating chemical changes and surface mineralization.....	119
Figure A1-1. Contact angle comparison of the aqueous sodium silicate used in this study (A) and as-received sodium silicate (B) on a borosilicate glass substrate	133
Figure A1-2. FTIR spectra of set old-batch sodium silicate used in this study (blue) and new-batch as-received sodium silicate (red).....	135
Figure A2-1. Moulds prepared for A-type specimens	137
Figure A2-2. Moulds prepared for B-type specimens, showing (a) the components of the mould prior to assembly and (b) the completed mould.....	139
Figure A2-3. (a) Oblique view of 3D-printed original positive mould and (b) plan view of custom Reprorubber negative mould from which positive composite scaffolds were fabricated to assess formability and geometric stability.....	140
Figure A3-1. Stereomicrographs of 0, 1, 3, 7, and 14-day <i>in vitro</i> specimens of monolithic 45S5 bioactive glass.....	143
Figure A5-1. FTIR spectra of residue obtained from 11.4 and 16.1 vol% composite specimens after 14 days <i>in vitro</i> immersion.....	149
Figure A5-2. FTIR spectra of residue obtained from 11.4 vol% specimen after 3 days <i>in vitro</i> immersion.....	150

List of Symbols

A	Kinetic parameter equivalent to maximum mass loss (dimensionless)
A_o	Cross-sectional area (mm ²)
$A_{particle}$	Area of a particle (μm ²)
B	Kinetic parameter equivalent to 50% reaction completion point (hours)
C	Circularity (dimensionless)
C_x	Convexity (dimensionless)
d	Unconfined compression test: displacement (mm) Bragg's law: lattice spacing (nm)
h	Height (mm)
h_o	Initial UCS sample height (mm)
I_B	Bioactivity index (dimensionless)
m	Mass (g)
m_t/m_i	Normalised mass loss (dimensionless)
n	Ideal gas law: number of moles of gas (dimensionless) Bragg's law: order of reflection (dimensionless integer)
n_s	Number of spheres occupying <i>in vitro</i> specimen volume (dimensionless)
P	Load during UCS test (N)
P_C	Convex hull perimeter of a particle (μm)
P_{max}	Maximum load before failure in UCS test (N)
R	Gas constant (J/mol·K)

r	Radius (mm)
Ref	Reflectance signal from FTIR spectroscopy (dimensionless)
SA_i	Surface area (mm ²)
T	Temperature (K)
t	Time (hours)
$t_{0.5BB}$	Time required for half of a surface to bond with living tissue (hours)
V	Volume (cm ³)
V_{min}	Calculated volume of a sample assuming zero closed pores (cm ³)
$vol\%$	Volume percent of a given constituent (dimensionless)
$wt\%$	Weight (mass) percent of a given constituent (dimensionless)

Greek Symbols

ε	Engineering strain (mm/mm)
ε_f	Maximum engineering strain during UCS test (mm/mm)
θ	Diffraction angle (°)
λ	Wavelength of X-rays (nm)
ρ_i	Density (g/cm ³)
σ	Stress (MPa)
σ_{UCS}	unconfined (uniaxial) compressive strength (MPa)

Subscripts

<i>BAG</i>	Bioactive glass
<i>C</i>	<i>in vitro</i> specimen
<i>reference chamber</i>	Pycnometry reference chamber
<i>occ</i>	Maximum volume of spheres occupying specimen volume
<i>S</i>	<i>in vitro</i> spherical particle approximation
<i>specimen</i>	Pycnometry specimen
<i>specimen chamber</i>	Pycnometry specimen chamber
<i>tested sample</i>	Pycnometry specimen at time of analysis
<i>t</i>	Value at time <i>t</i>
<i>tot</i>	Total surface area of spheres
<i>WG,l</i>	Liquid (aqueous) sodium silicate
<i>WG,s</i>	Solid (set) sodium silicate

List of Abbreviations

ACP	Amorphous calcium phosphate
AP	Alkaline phosphate
BAG	Bioactive glass
BSE	Backscattered electrons
BMP	Bone morphogenic protein
ECM	Extracellular matrix
EDX	Energy-dispersive X-ray spectroscopy
FTIR	Fourier-transform infrared spectroscopy
HA	Hydroxyapatite
HCA	Hydroxycarbonate apatite (hydroxy-carbonylapatite)
micro-CT	Micro-computed tomography
OCP	Octacalcium phosphate
OLM	Optical light microscopy
PSA	Particle size analysis
SBF	Simulated body fluid
SE	Secondary electrons
SEM	Scanning electron microscopy
SFF	Solid free-from fabrication
SLS	Selective laser sintering
SS	Sodium silicate
SSI	Surgical site infections
UCS	Unconfined/uniaxial compressive strength
VPS	Vinyl polysiloxane
XRD	X-ray diffractometry

Chapter One

Introduction¹

Bones possess the remarkable ability for self-repair, wherein broken or diseased bone is replaced by new bone growth. However, for many individuals, this healing process will not occur without the use of bone grafts to repair the damaged bone. Bone grafts are medical implants used to provide the body with the necessary support to regrow bone when it otherwise cannot. These materials encourage healing by providing a scaffold for new bone growth, structural support, and an ideal environment for bone healing. Though autografts are often considered the “gold standard” in bone repair, as they provide excellent bone-bonding and tissue replacement, the use of a patient’s own bone as a graft material is fraught with limitations [1]. As autografts require an additional surgery to harvest graft material, the risk of complications and infections is high—surgical site infections are particularly common following orthopaedic surgery, increasing healthcare costs and recovery time [2]. The use of bone scaffold materials, such as bioactive glasses, presents a means to ameliorate the risks of autografts and reduce the incidence of post-surgical complications.

Bioactive glasses were invented in 1969, with Larry Hench’s 45S5 Bioglass being the first artificial material found to form a chemical bond with bone [3]. This discovery sparked the advent of bioceramics as bone tissue substitutes that encouraged the formation of new bone while simultaneously corroding in the body, to be entirely replaced by native bone [4, 5]. The use of bioactive glasses as synthetic bone tissue scaffolds, designed to overcome the limitations of autografts, has become widespread clinical practice. However, the use of bioactive glasses is restricted by the use of traditional ceramic processing techniques to produce scaffolds; as such, “*the design criteria for an ideal scaffold for bone regeneration have not yet been fulfilled*” ([6], p.1280).

¹ Portions of this chapter have been submitted for publication in Metallurgical and Materials Transaction A: C. M. Guzzo and J. A. Nychka, “*Fabrication of a Porous and Formable Ceramic Composite Bone Tissue Scaffold at Ambient Temperature,*” Under Review, submitted 12-01-2019.

A considerable limitation of bioactive glass is its very nature—as a ceramic material, the typical processing techniques (i.e., sintering) required to fabricate it into a porous scaffold are incompatible with *in situ* biological applications. These ceramic processing techniques, (e.g., foaming, sponge replication, foaming, laser-sintering, or freeze-drying) require thermal consolidation and the use of additives to suppress crystallisation, which reduce the bioactivity of the material. Moreover, the use of traditional ceramic processing techniques necessitates that the scaffold be first produced *ex situ*, requiring more bone to be surgically removed to allow insertion of shapes created by the processing method [7]. Even the production of ‘custom’ implant geometries via solid freeform fabrication (SFF), such as additive manufacturing, does not allow for the conformal application of a scaffold to undercuts. The use of SFF techniques also requires the use of a 3-D model of the bone defect, usually acquired by micro-CT—the time and cost required for the production of these custom shapes is prohibitive for widespread clinical use [7]. An ideal scaffold material would not be bound by the need for typical ceramic processing techniques, nor would it require additional imaging or manufacturing infrastructure.

“The specific research question addressed in this work is: how can synthetic bone tissue scaffolds be produced to be formable and porous so that they may prompt bone-tissue regrowth in a safe, real-time wound-customisable, and effective manner?” [8, p. 1]. The concept presented herein is the use of a liquid silicate precursor—sodium silicate—as a binder phase in a bioactive glass-based composite. Aqueous sodium silicate reacts with carbon dioxide gas to form a densified silicate glass, a characteristic that enables the composite material to initially take the form of a formable paste, which then sets into a rigid, porous scaffold once applied *in situ*. Medical carbon dioxide gas supply is currently present in all standard operating rooms. This formable tissue scaffold will circumvent the limitations associated with traditional ceramic processing; in particular, the creation of an interconnected porous network without thermal consolidation and the ability to implant a truly conformal scaffold without additional CT scans, 3-D models, or time-consuming custom fabrication.

The work presented in this thesis is a proof-of-concept study that investigates if an *in situ*-castable scaffold can be produced with appropriate porosity, mechanical properties, and *in vitro* bioactivity response. The effect of composition on these characteristics is then

assessed to determine the optimal scaffold composition. Further investigation of these material characteristics *in vivo* is planned, but was outside the scope of this study.

This research was undertaken by first establishing a set of design criteria to evaluate both the state of the art and the research presented in this work. Six design criteria were determined to be necessary in the design of a successful synthetic bone graft; namely formability, geometric stability, porosity, load-bearing capacity, bioactivity, and resorbability. The criteria presented are in agreement with findings and concepts in literature, such as presented in [7, 9, 10, 11]. It should be noted that no current single technology is capable of achieving *all* criteria.

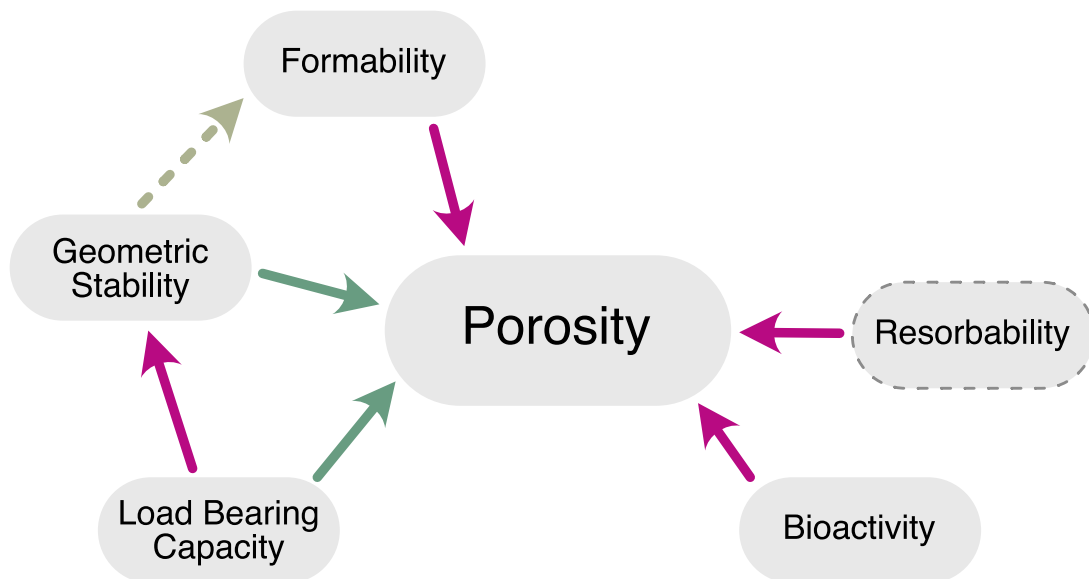


Figure 1-1. Map of design criteria interdependence. Arrows indicate which design criteria are dependent; pink arrows indicate a corresponding relationship and green arrows indicate an inverse relationship. Dashed arrows indicate a dependent relationship only in the context of how design criteria were evaluated in this work. Dashed borders indicate design criteria that were assessed indirectly. Adapted from [8].

Figure 1-1 illustrates the interdependent nature of the design criteria; though all of the design criteria are in some way connected, the verification of appropriate porosity was emphasised in this work—porosity is of paramount importance for scaffold success.

A review of literature presented in Chapter 2 introduces bone grafts, synthetic bone tissue scaffolds, as well as the materials used in this research. Additionally, Chapter 2.5 establishes the design criteria used to assess current synthetic bone graft technologies and guide the development of the composite material investigated herein. The experimental design of this work, including processing and characterisation, is detailed in Chapter 3. Results of this work are discussed with respect to each design criterion in Chapter 4. Porosity of the composites was investigated via optical light microscopy (OLM) with epoxy infiltration (Chapter 4.4.1), scanning electron microscopy (SEM; Chapter 4.4.2), gas pycnometry (Chapter 4.4.3), and micro-computed tomography (micro-CT; Chapter 4.4.4). Formability of the unset paste and geometric stability of the set scaffold are necessarily evident during processing, and as such were established in the preliminary feasibility trials involving mould fidelity and reproduction resolution (Chapter 4.2, 4.3). Porosity was expected to be inversely proportional to the material's load-bearing behaviour—this relationship was explored with unconfined compression strength testing to establish the extent to which porosity influenced compressive strength (Chapter 4.5). Bioactivity and indirect indicators of resorbability were assessed *in vitro*; surface mineralisation was investigated with multiple characterisation techniques to identify and confirm the presence of biominerals (Chapter 4.6). The effect of composite composition and porosity on mineral formation was analysed via SEM with energy-dispersive X-ray spectroscopy (EDX; Chapter 4.6.2), X-ray diffractometry (XRD; Chapter 4.6.3), and Fourier-transform infrared spectroscopy (FTIR; Chapter 4.6.4). The synthesis of this research, areas of future work, and final recommendations are presented in Chapter 5.

Bibliography – Chapter One

- [1] J. R. Jones, P. D. Lee and L. L. Hench, "Hierarchical porous materials for tissue engineering," *Philosophical Transactions of the Royal Society: A*, vol. 364, pp. 263-281, 2006.
- [2] A. Bachoura, T. G. Guitton, R. M. Smith, M. S. Vrahas, D. Zurakowski and D. Ring, "Infirmity and Injury Complexity are Risk Factors for Surgical-site Infection after Operative Fracture Care," *Clinical Orthopaedics and Related Research*, vol. 469, no. 9, pp. 2621-2630, 2011.
- [3] J. R. Jones, "Review of bioactive glass : from Hench to hybrids," *Acta Biomaterialia*, vol. 9, pp. 4457-4486, 2012.
- [4] L. L. Hench, "Challenges for Bioceramics in the 21st Century," *American Ceramic Society Bulletin*, vol. 84, no. 9, pp. 18-21, 2005.
- [5] J. Wilson, A. Yli-Urpo and H. Risto-Pekka, "Bioactive glasses: clinical applications," in *An Introduction to Bioceramics*, Singapore, World Scientific, 1993, pp. 63-74.
- [6] J. R. Jones, "New trends in bioactive scaffolds: The importance of nanostructure," *J. Euro. Ceram. Soc.*, vol. 29, pp. 1275-1281, 2009.
- [7] F. Baino, G. Novaira and C. Vitale-Brovarone, "Bioceramics and scaffolds: A winning combination for tissue engineering," *Frontiers in Bioengineering and Biotechnology*, vol. 3, pp. 1-17, 2015.
- [8] C. M. Guzzo and J. A. Nychka, "Fabrication of a Porous and Formable Ceramic Composite Bone Tissue Scaffold at Ambient Temperature," *Metallurgical and Materials Transactions A*, Under Review, 2020.
- [9] P. Chicolata, V. Kulda and V. Babuska, "Fabrication of scaffolds for bone-tissue regeneration," *Materials*, vol. 12, no. 568, pp. 1-25, 2019.
- [10] H. Qu, H. Fu, Z. Han and Y. Sun, "Biomaterials for bone tissue engineering scaffolds: A Review," *RSC Advances*, vol. 9, no. 45, pp. 26252-26262, 2019.
- [11] E. Fiume, J. Barberi, E. Verné and F. Baino, "Bioactive Glasses : From Parent 45S5 Composition to Scaffold-Assisted Tissue-Healing Therapies," *Journal of Functional Biomaterials*, vol. 9, no. 24, pp. 1-33, 2018.

Chapter Two

Background and Literature Review¹

2.1 Bone Tissue Scaffolds

Bone grafts are medical implants used to provide the body with the necessary support to regrow bone when it otherwise cannot. These grafts are most commonly used in elderly patients and individuals with musculoskeletal disorders, such as osteoporosis. In 2006 alone, expenditures related to musculoskeletal diseases was estimated to be 7.4% of US GDP [1], and this number is expected to increase due to an aging population.

Fractured bones are among the most common injuries, with 6.3 million fractures occurring annually in the United States [2]. The majority of fractures will heal without major intervention and require only immobilisation in a cast or splint. However, this bone healing process does not always occur naturally—for elderly patients, or patients with osteoporosis, bone cancer, osteomyelitis (an infection of the bone), or any illness that causes them to be immunocompromised, the body cannot regrow bone independently. Without the use of a repair material, such as a bone graft, the bone defect will never completely heal. Bone grafts are materials that are used to repair broken or missing bone. These materials are placed in the bone defect, encouraging healing by providing a scaffold for new bone growth, structural support, and the necessary environment for bone growth.

The “gold standard” in bone grafting are *autografts*, which are comprised of bone harvested from the patient’s own body. Autografts offer the best healing outcomes with no risk of rejection, but multiple issues limit their success. All autografts require additional surgery to harvest the bone, which carries significant risk of infection—especially in elderly and immunocompromised patients. Surgical site infections (SSI), which are especially

¹ Portions of this chapter have been submitted for publication in Metallurgical and Materials Transaction A: C. M. Guzzo and J. A. Nychka, “*Fabrication of a Porous and Formable Ceramic Composite Bone Tissue Scaffold at Ambient Temperature*,” Under Review, submitted 12-01-2019.

common in surgeries involving implants [3], double the rate of rehospitalisation. Orthopaedic SSI increase healthcare costs more than three times by extending hospital stays by a median of 2 weeks [4]. The recovery time for many bone-related surgeries is several months to years (e.g., 1-2 years for a tooth extraction and placement of a prosthetic tooth [5]) with complications and delays (most commonly due to infection), multiple surgeries, pain, anxiety, and other psychological considerations [6, 4].

In addition, harvesting bone often results in *donor site morbidity* (any complications at the donor site following graft surgery) [7]. In healthy patients, incidence of ambulation difficulty was found to be 50.7% and incidence of pain was found to be 26.1%, 2 years after bone harvesting [8]. The incidence of donor site morbidity in the elderly, immunocompromised, or patients with osteoporosis—the patients most likely to need bone grafts—is higher than in healthy patients. Furthermore, if a patient is unable to regrow their original bone defect without a bone graft, it is unlikely that the bone removed from the donor site will heal, which effectively shifts the bone defect to the donor site. The amount of bone that can be harvested safely is very thus limited, and often insufficient to be used as an autograft [9].

As an alternative to autografts, *allografts* (bone donated from a living patient or non-living donor) are sometimes used to repair bone defects—unfortunately, allografts are considerably less effective at healing bone, and carry significant risk of rejection and infection. The supply of compatible allografts is often limited and difficult to predict, and incur significant costs due to the extensive harvesting, processing, and storage procedures [9].

2.1.1 Synthetic Bone Tissue Scaffolds

In response to the myriad limitations of autografts and allografts, synthetic bone graft materials have been developed. These bone graft substitutes are designed to provide the healing and structural capabilities of autografts, without the need for additional surgeries or supply constraints. Though the first successful bone graft substitute was effectively calcium

sulphate (Plaster of Paris), used in 1892 [10], the first material specifically engineered to repair bone defects was not brought to market until 1991 [11].

To produce a successful synthetic scaffold material, it is necessary to map the advantages of autografts to synthetic scaffold design criteria. These design criteria are then used to guide the development of a bone graft substitute that is, ideally, as successful as an autograft. These design criteria are presented in further detail Chapter 2.5.

Synthetic bone tissue scaffolds can be produced from many materials, including polymers, calcium phosphates, ceramics, and composites thereof [12, 13, 9, 14, 15]. A plethora of processing techniques have been developed to produce tissue scaffolds from these materials, as explored in further detail in Chapter 2.3.2. While the use of bone graft substitutes is increasing [12], no product on the market fully satisfies the need for a material that performs as well as autografts without the associated risks.

2.2 Biomaterials

Bioactivity, as a characteristic of biomaterials, refers to the ability of a material to induce a specific, desirable response when implanted in the body [16]. These responses can include tissue regeneration, cell differentiation and proliferation, or otherwise repairing injury. Bioactive interactions involve an interfacial bond between bioactive material and the body; the *bioactivity index* of a material (I_B), defined as the time required for bond formation, is a parameter used to assess bioactivity. This parameter is calculated as per Equation 2.1, where $t_{0.5bb}$ is the time required for half of the material surface to form a bond with physiological tissue [17].

$$I_B = 100/t_{0.5bb} \quad (2.1)$$

2.2.1 Bioceramics and Bioactive Glasses

In bioceramics, the property of bioactivity is divided into two classes: Class A and Class B bioactivity. Class A materials exhibit rapid bone bonding, soft tissue bonding, and bone proliferation, while Class B materials bond slowly with bone, and do not exhibit soft tissue bonding or complete bone proliferation [18]. Class A bioceramics release specific concentrations of soluble silica and Ca^{2+} ions, promoting both intracellular and extracellular responses that induce mineralisation and cell colonisation, encouraging the rapid formation of new bone. In contrast, any bone bonding properties of Class B materials is due only to extracellular effects [17]. The compositional ranges of Class A and Class B bioactive glasses is shown in the ternary phase diagram in Figure 2-1. Class A materials are preferable, as Class B materials have low survivability when implanted, and can induce complications such as peri-implantitis [10]. Both classes of bioactive ceramics exhibit *osteointegration*, which is the ability bond chemically to biological tissue without forming fibrous tissue around the bone or promoting an inflammatory immunological response. The bioactive characteristics of bioceramics for bone repair can be described as *osteoconductivity*, *osteogenicity*, and *osteoinductivity*; osteoconductivity refers to the ability of osteoblasts and osteoprogenitor cells to attach to the material, osteogenicity refers to the ability of osteoblasts to mineralise and form a substrate for new bone, and osteoinductivity refers to the ability of the material to induce the differentiation of osteoprogenitor cells into osteoblasts. These characteristics are detailed in Chapters 2.2.1.2 and 2.2.1.3.

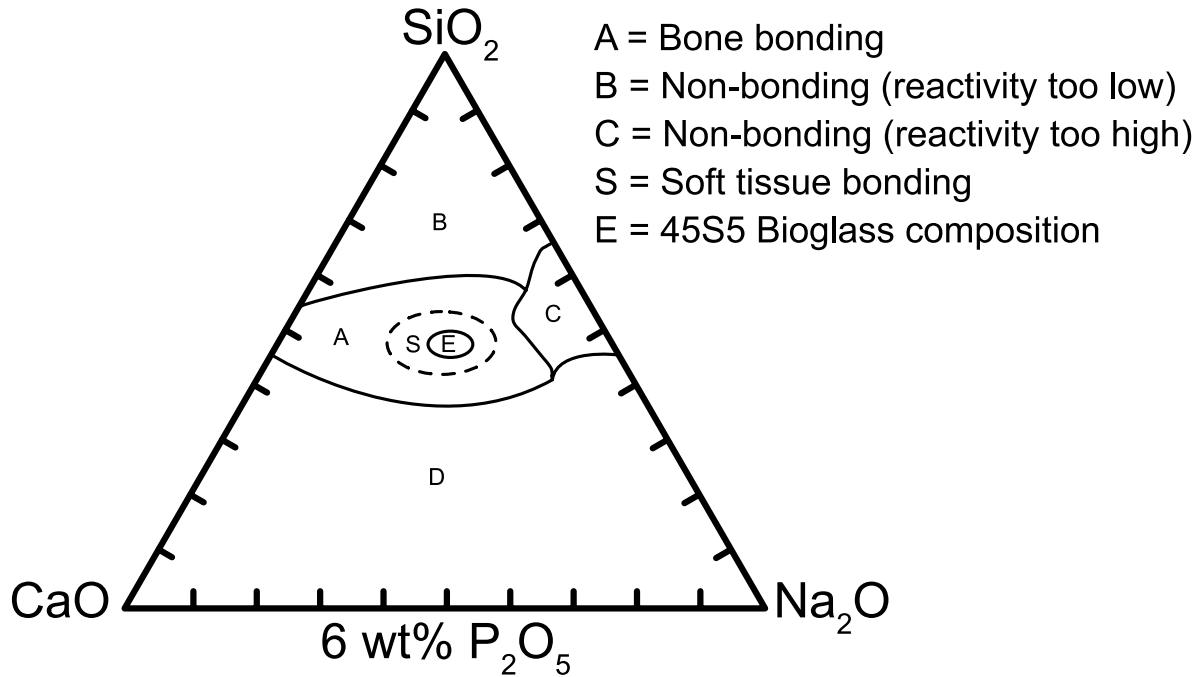


Figure 2-1. Ternary phase diagram of the SiO_2 - CaO - Na_2O system at 6 wt% P_2O_5 . Regions B, C, and D are not bioactive and do not induce a desirable response when implanted. Region A indicates compositions of bioactive glass that are at least Class B bioactive, with the inner region of S indicating Class A bioactivity (bonds to bone and soft tissues and activates genes necessary for osteogenesis). Region E indicates the composition of 45S5 Bioglass, the first bioactive glass developed and the most common composition in use today. Further details regarding 45S5 Bioglass are presented in Chapter 2.3.1. Adapted from [17].

2.2.1.1 Mechanisms of Bioactivity in Bioactive Glass

The mechanisms by which bioactive glasses bond to living tissue can be summarised as an eleven-stage process, as illustrated in Figure 2-2 below. These 11 stages can be separated into two phases; Phase I (stages 1-5 in Figure 2-2) involves chemistry alone, while Phase II relies on biology to effect chemical changes [8]. Phase I results in the formation and crystallisation of a hydroxycarbonate apatite (HCA) film from amorphous calcium phosphate (ACP). Phase II then interacts with biological moieties, using dissolved surface products from the bioactive glass to induce osteogenesis and crystallise the extracellular matrix (ECM) [17]. Phase I is observable with *in vitro* immersion in simulated body fluid, while Phase II requires the presence of cells and biological factors.

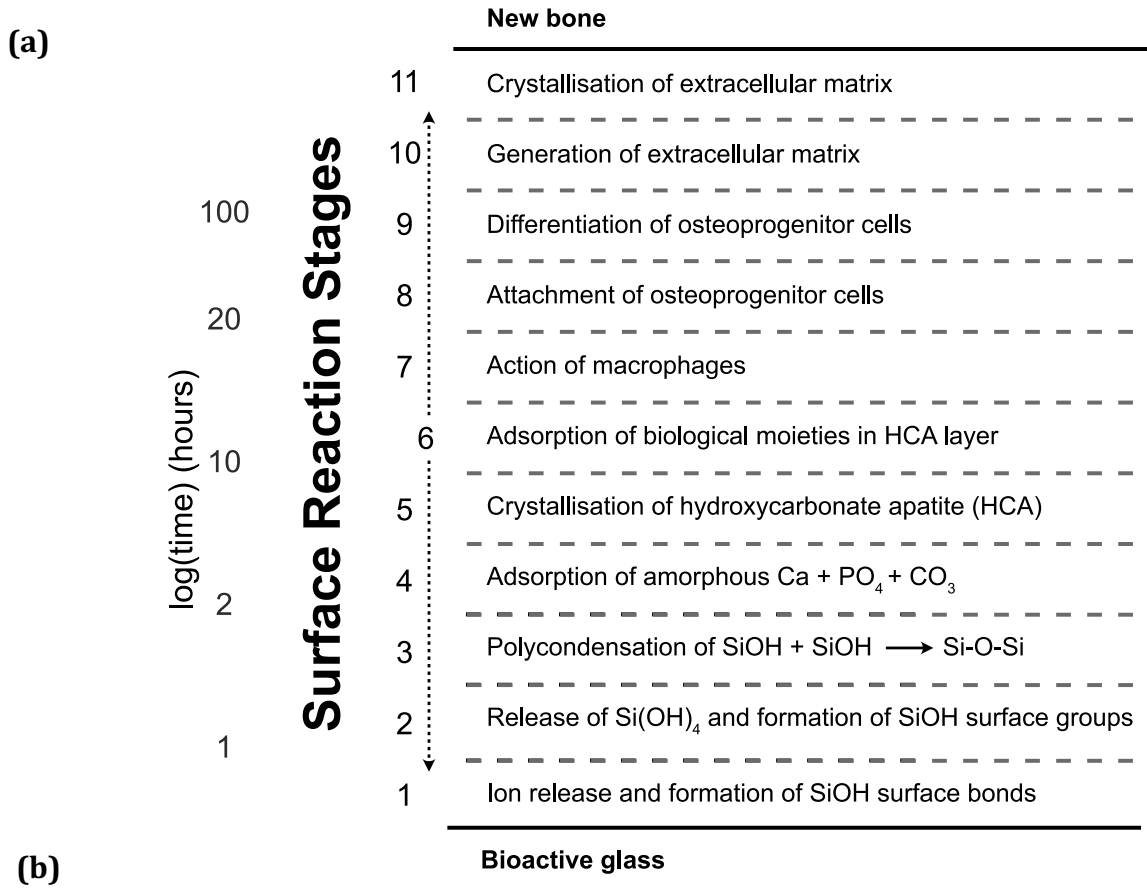
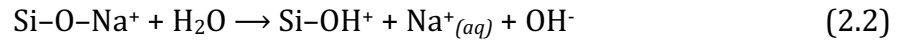


Figure 2-2. Sequence of surface reactions that take place at the bioactive glass/tissue interface; (a) shown with approximate timeframe (adapted from Hench et al., 2020 [19]); (b) schematically illustrated (adapted from Ducheyne and Qiu, 1999 [20]).

Phase I begins within minutes of implantation, proceeding as follows [21]:

1. The silicate matrix of the bioactive glass begins to dissolve, releasing Ca^{2+} , Na^+ , and PO_4^{3-} ions (if present) that exchange with H^+ and H_3O^+ ions present in the surrounding solution. In accordance with Equation 2.2, initial silanol bonds (Si-OH) form on the surface, and the alkaline ions increase the pH of the local environment [22].



2. Following an increase in pH due to the consumption of H^+ ions, the dissolution of Si-O-Si bonds breaks the silica network and releases soluble silica (Si(OH)_4), exposing silanol surface groups (Si-OH) to the solution. This process is described in Equation 2.3:



3. The polycondensation of these silanol functional groups facilitates the formation of a 1-2 μm silica gel layer, which is fully polymerised within 2 hours [19]. This amorphous gel layer is depleted in Na^+ and Ca^{2+} ions, which have been released into the aqueous environment. The silica gel layer exhibits a high specific surface area (up to $100 \text{ m}^2/\text{g}$) due to micro-porosity (pore diameter 30-50 \AA) [17].
4. Ca^{2+} and PO_4^{3-} ions migrate through the gel from both the bioactive glass and the solution, forming a second layer atop the silica-rich gel layer. This second layer is comprised of ACP ($\text{CaO-P}_2\text{O}_5$). The presence of octacalcium phosphate (OCP) has been observed to form as a metastable intermediate phase prior to ACP formation [23], or as a precursor to HCA formation [24, 14]
5. Hydroxyl and carbonate groups from solution are incorporated into the gel while the glass dissolution process continues. The ACP layer crystallises into HCA, forming a bilayer with the hydrated silica gel [25]. The HCA layer increases in thickness as a function of time, up to 100 μm . The surface of the HCA layer is compositionally and

structurally similar to the nanocrystalline mineral phase of natural bone, facilitating bonding between the implant and surrounding tissues [17].

Phase II, which is less fully understood than Phase I [23, 17], then progresses with the interaction of biological factors:

6. Several biological moieties, such as proteins and growth factors, are adsorbed to the surface of the implant. This process can begin concurrently with the preceding gel formation stages [17].
7. Macrophages act on the surface, preparing the implant for new tissue growth [25].
8. After approximately 12 hours, stem cells (osteoprogenitor cells) colonise the material surface [17].
9. The stem cells proliferate and differentiate to osteoblasts at a rapid rate, due to the upregulation of several gene families induced by the dissolution products of the bioactive glass [26].
10. Osteoblasts begin to produce bone growth factors and vascular development genes, resulting in cell attachment and mitosis, culminating in the production of ECM minerals [27].
11. After 6-12 days of implantation, the ECM matrix crystallises around mature osteocytes, forming new bone [25]. The formation of new bone with bioactive glasses extends beyond the implant-bone interface due to their highly osteogenic effects; this characteristic has been coined *osteoproduction* by Wilson and Low [28] to differentiate it from osteoinduction, which refers only to cell differentiation and bone growth at the implant interface [23].

The time sequence described above applies primarily to 45S5 bioactive glass, as compositional differences affect the rate and extent of bioactivity. Increasing the silica content beyond that of 45S5 (45 wt%) results in a decrease in bioactivity until 60 wt%, after which the material is no longer Class A bioactive. Compositions with less than 45 wt% silica dissolve more rapidly due to a poorly interconnected silica network, and thus mineralise in

shorter times. Moreover, the addition of metal cations (i.e., Al^{3+} , Ti^{4+} , Ta^{5+}) can substitute Ca^{2+} and Na^{+} ions in the above process, reducing bioactivity and rate of dissolution [17].

2.2.1.2 Osteoconduction and Osteoinduction

While both Class A and Class B bioactive glasses are *osteoconductive*—meaning that they support the growth of bone on their surface—only Class A materials are *osteoinductive*. Not only do osteoinductive materials provide a scaffold for bone growth, they also encourage surface colonisation by osteoprogenitor cells and growth of new bone (*osteogenesis*) [29]. Stimulation of osteoprogenitor cells into osteoblasts may take the form of normal bone growth during childhood, or repair after injury. In older adults, osteoprogenitor cells are ‘inactive’, and must be effectively re-activated by an appropriate chemical to undergo differentiation [30]. The incidence of osteoprogenitor cells present in older adults is very low (1/100 000), and thus it is critical that the few cells that are present receive the appropriate chemical signals from their environment in order to proceed to osteogenesis [25]. In the context of bioactive glasses, this environment occurs when ions (Si^{2+} and Ca^{2+}) from the implant material activate seven families of genes, which facilitate cell proliferation, differentiation, and new bone growth [27, 31, 32]. The activation of these genes ensures that as many cells as possible follow the route of differentiation, mitosis, and osteocyte maturation. Osteoblasts form mature osteocytes and crystallise the ECM via transport of ACP from mitochondria to vesicles that then deposit ACP in surrounding collagen fibrils [33]. The metastable ACP then crystallises into mature HA platelets, a process that has been observed to proceed via intermediate OCP formation due to the lower surface energy, and thus lower nucleation barrier, of OCP [14]. The fate of osteoprogenitor cells involved in the bioactive glass-mediated osteogenesis process is detailed schematically in Figure 2-3.

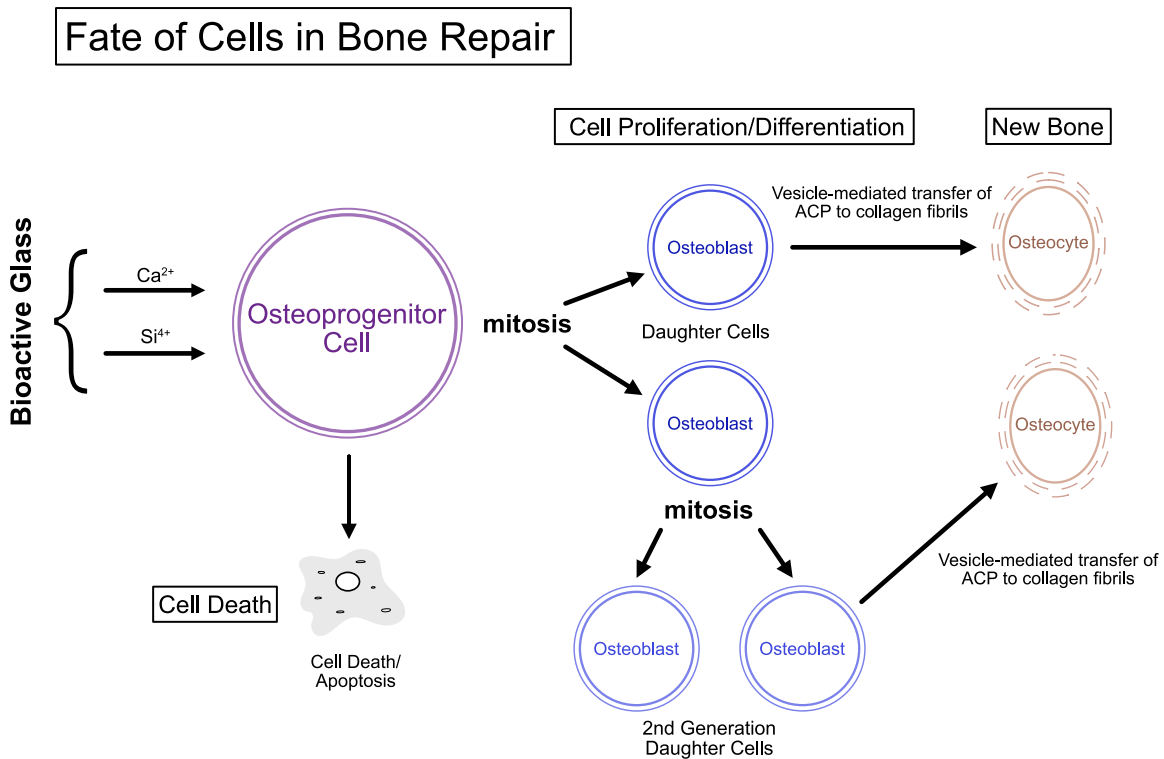


Figure 2-3. Schematic depiction of the fate of cells involved in bone repair. Osteoprogenitor cells may proceed to apoptosis (programmed cell death), or differentiate into osteoblasts and proliferate via mitosis, finally forming new bone (osteocytes) via the transport of ACP to surrounding collagen fibrils. Bioactive glass dissolution products (calcium and silicon ions) facilitate the cell proliferation and differentiation process. Adapted from Hench et al., 2010 [25].

The osteoinductive response is primarily controlled by composition, but morphology and porosity of the implant also affect cell attachment, and by extension, bone growth. Porous bioactive glasses have shown the highest rates of cell adhesion and differentiation, while implants with pore sizes $< 50 \mu\text{m}$ are unable to support bone and tissue infiltration. Additionally, pores must be interconnected to allow for vascularisation and nutrient diffusion throughout the new bone—a pore interconnection size of approximately $10 \mu\text{m}$ is necessary to permit these processes [8].

2.2.1.3 Osseointegration and Osseoincorporation

An ideal bioceramic for bone repair would undergo both *osseointegration*—the direct functional contact and chemical bonding between bone and implant—and

osseoincorporation—the controlled degradation of a biomaterial as it is replaced by new bone [34]. Excellent initial osseointegration encourages faster healing and better bonding with living tissues, while osseoincorporation facilitates the human body's own bone growth process, without leaving an implant behind. The complete dissolution of bioactive glasses after healing is desirable, as any implant will have interfacial interactions with the body that may potentially be harmful. Moreover, the mechanical properties of bioactive glasses are poor in comparison to human bone, and this discrepancy can lead to future issues if a long-term implant remains [35].

The dissolution of bioactive glass proceeds due to aqueous environments in addition to the action of cells described in Chapter 2.2.1.1. The environmental degradation process of bioactive glass (particularly 45S5) after HCA formation (Stage 5 in Figure 2-2) is described as follows, and occurs concomitantly with the cellular consumption of bioactive glass to form new bone as described in Chapter 2.2.1.1 [36, 37]:

- (i) Bodily fluid (*in vivo*) or SBF (*in vitro*) saturates the implant and penetrates pores, if present. Ions (particularly Na⁺) leach from the crystalline HCA phase, preferentially originating from favourable locations (dislocation and grain boundaries).
- (ii) The aqueous environment breaks the crystalline matrix into fine grains, simultaneously dissolving the glass matrix.
- (iii) Point defects generated by ion dissolution distort the crystalline lattice, leading to the development of an amorphous structure. The subsequent release of surface energy can be used as the necessary activation energy for this transition.

This degradation proceeds in conjunction with cell behaviour, will theoretically proceed until the entire implant has dissolved. However, porous scaffolds are necessary for complete degradation, as cell transport must be possible in order to colonise the implant surface if the material is to be completely resorbed. The above conversion and dissolution reactions can occur incompletely with bioactive glass monoliths *in vivo*. This resorption issue can lead to complications and poor performance, as addressed in Chapter 2.3.1.

2.3 Processing of Bioactive Glasses

2.3.1 History of Bioactive Glass

Though bioactive glasses pioneered the field of bioactive materials, they are relatively new in the field of materials science—the concept was first conceived in the late 1960s by Larry Hench. Responding to a question from an army colonel who asked why no materials could withstand the environment of the human body, Hench began researching materials that would bond with tissue without rejection. Choosing a near-eutectic composition for its ease of casting, the first paper was published in 1971, naming 45S5 Bioglass® as a Class A bioactive material [23, 38]. The name of 45S5 was chosen to reflect the composition, which is 45% SiO₂–24.5% Na₂O–24.5% CaO–6% P₂O₅ (wt%; recall Figure 2-1). The high CaO/P₂O₅ ratio of this composition renders the surface very reactive when implanted [17]. The specific mechanisms of bioactivity (recall Chapter 2.2.1.1) were subsequently investigated until 1985, when the first 45S5 medical device was approved for use—an ossicular reconstruction prosthesis used to treat hearing loss. Follow-up studies examining these implants over 10+ years have found them to be successful in the long term [39]. Research has been ongoing since, with composites and tissue scaffolding as specific areas of interest. Though 45S5 remains the most commonly used bioactive glass in clinical applications, several other formulations have been approved for orthopaedic bone grafting [30]. These bioactive glasses are used in a variety of applications ranging from bone-filling implants and stem cell engineering to control of infection/healing [40, 41]. In addition to bone bonding, a key property of bioactive glass is its inherent anti-bacterial nature [42]. The high local pH created by dissolution of bioactive glass, particularly 45S5, results in an environment wherein bacterial infections are harder to develop.

However, it is difficult to produce bioactive glass in a form that will completely resorb, acting as a temporary scaffold for the growth of native bone; monoliths resorb incompletely, only forming new bone on the surface of the material. While this is acceptable or desirable for some applications, it is not ideal for repair of bone defects; the best implant is a temporary

one [19]. An interconnected, porous scaffold of bioactive glass that can be conformally applied to a bone defect could circumvent resorption issues found in monoliths. Traditional ceramic processing methods, such as sintering, laser sintering, or hot isostatic pressing, are not feasible for use *in situ*, and may reduce bioactivity of the resultant scaffold [43]. This issue has been approached by altering chemistry, processing routes, and morphology of potential scaffolds; an overview of current advances is presented in Chapter 2.3.2.

2.3.2 State of the Art—Bone Tissue Scaffolds

Though bioactive glasses—particularly 45S5—exhibit great clinical potential, the issue of monolith bioactivity and osseoincorporation limits their success. In order to address the challenges associated with monolith implants, bone tissue scaffolds have been fabricated from bioactive glasses. Many processing techniques exist, and an overview of current strategies is summarised in Chapters 2.3.2.1-2.3.2.8. These techniques exhibit a range of advantages and disadvantages, with varying levels of utility, but currently no single bone scaffold fabrication route meets all established design criteria.

In addition to the processing routes described herein, a myriad of modifications are possible, such as the addition of growth factors (i.e., bone morphogenic protein; BMP) or doping with metal ions for antimicrobial (with silver) or angiogenesis-enhancing (with copper) effects [17, 44].

2.3.2.1 Sol-gel Synthesis

Sol-gel synthesis of bioactive glasses is the most common processing route for bioactive glass scaffolds, and is the second most common bioactive glass processing method after melt-quenching [17]. To produce bioactive glass via this wet synthesis route, liquid alkoxide or organometallic precursors (sol) and water are reacted. After silanol groups are produced, siloxane (Si–O–Si) bonds form and undergo polycondensation to produce a SiO₂ network (gel) [45]. Mechanical frothing is employed in conjunction with a surfactant or

gelling agent to generate pores, which are made permanent after aging and sintering [46]. Due to the nature of sol-gel production, bioactive glass scaffolds produced via this route are also inherently nanoporous and thus have far higher specific surface areas than traditional melt-derived glasses (50 m²/g or more as compared to 1 m²/g). This increased specific surface area generally results in higher levels of bioactivity and faster rates of degradation. However, this nanoporosity also renders sol-gel synthesised scaffolds highly brittle. Moreover, the sol-gel process does not produce formable scaffolds; though porous, these materials cannot be pressed into voids or easily formed to unique wound geometries [13].

2.3.2.2 Foaming Methods

Multiple foaming methods exist for the production of bioactive glass scaffolds, all of which utilise a gas to form pores within a bioactive ceramic. This gas can either be incorporated from an external source (injection, mechanical frothing, or via aerosol propellant), or evolved *in situ* [47]. The entrapped gas results in the creation of pores when the material is set (typically via thermal processing). Difficulties with foaming methods include low pore interconnectivity, which hinders osseointegration, a non-porous outer surface, and a lack of formability. To address surface porosity, *in situ* polymerisation foaming techniques have been developed, also known as gel-cast foaming. This process involves the combination of an aqueous ceramic solution, a water-soluble organic monomer, a polymerisation initiator, and catalyst. This mixture is mechanically agitated, and with the assistance of a surfactant, creates a ceramic foam. Despite the ability to form pores *in situ*, current foaming methods require high-temperature stabilisation (sintering and organic monomer burnout) and cannot be implanted while formable. Additionally, gel-cast foaming does not alleviate poor interconnectivity, and often results in scaffolds with inconsistent pore size and distribution [13, 46].

2.3.2.3 Porogens

The use of porogens (i.e., temporary space-holding materials) is yet another scaffold fabrication strategy. Porogens are typically water-soluble (e.g., NaCl), organic solvent-soluble (e.g., paraffin), or able to be burned out (e.g., polyethylene, rice husk starch consolidation) [48]. These porogens are combined with a bioceramic polymer and the mixture is compressed into a compact of the desired shape. The porogens are then removed via water, solvent, or thermal processing (burnout); thermal processing is necessary in each case to consolidate the ceramic powder into a rigid scaffold. Scaffolds produced with porogens typically have high mechanical properties, and open porous structures can be fabricated with this method, but pore interconnectivity and homogeneity are typically low. Since thermal consolidation is required before implantation, scaffolds produced with porogens are not formable *in situ* [13].

2.3.2.4 Additive Manufacturing and Fused Deposition Modelling

Solid freeform fabrication (SFF) techniques, such as additive manufacturing (3-D printing), stereolithography, and fused deposition modelling, are utilised to create bioactive scaffolds with precisely specified geometries. These strategies typically use a composite filament comprised of bioactive glass and a sacrificial binder phase, which is burned out during consolidation (sintering) after printing. High pore interconnectivity, material homogeneity, and custom shapes are possible with SFF [15]. However, multiple challenges limit the success of SFF produced scaffolds, including the need to obtain 3D models of the patient's bone defect via micro-computed tomography (micro-CT) or magnetic resonance imaging (MRI) prior to scaffold fabrication [46]. This additional step is time consuming and increases costs, adding to an already costly technique. Additionally, it is difficult to achieve the resolutions necessary for conformal bone defect repair; complex geometries such as undercuts further impede implantation [13].

2.3.2.5 Sintering and Thermal Consolidation

Thermal consolidation techniques, such as sintering, are conventional ceramic processing methods and can be used to fabricate porous scaffolds from bioceramic powders or fibres. Sintering can be applied to compacted powders, which coalesce and fuse under high temperature to form porous networks; however, many compositions of bioactive glass (particularly 45S5) devitrify under high temperatures, lowering bioactivity and mechanical properties. Alternatively, selective laser sintering (SLS) can be utilised to form precise geometries from a powder bed. Though SLS allows for custom shapes, much like the aforementioned SFF techniques, it encounters many of the same issues: namely, the need for 3D model acquisition and resolution limits [13, 46, 14, 25].

2.3.2.6 Freeze-drying and Thermal Separation

Thermal separation techniques employ temperature-induced phase separation between polymer, ceramic, or inorganic materials in suspension. Reducing the temperature causes the solvent to solidify first, forcing the ceramic/polymer into the interstitial spaces, taking the form of porous networks. The material is then lyophilised (freeze-dried) to evaporate the solid solvent via sublimation [46]. Though highly interconnected, the pore size distribution and dispersion of scaffolds produced in this method can be irregular and difficult to produce consistently [49]. This technique cannot be applied to bone defects directly, and thus lacks formability.

2.3.2.7 Sponge Replication

Sponge replication has become a very common method of bone tissue scaffold fabrication, owing to its simplicity, low cost, and consistency. Briefly, sponge replication involves impregnating a sponge (typically polyurethane) with a slurry of ceramic powder and binder phase (e.g., poly(vinyl alcohol) or colloidal silica). Excess slurry is removed by applying pressure to the sponge, leaving a uniform coating of ceramic slurry on the sponge structure. The sponge material is then removed via pyrolysis, which sinters the ceramic

slurry into a positive reproduction of the sponge template. Though this technique does not produce formable scaffolds, the sponge template can be made into a custom shape to improve implant integration. Challenges of sponge replication include low toughness and mechanical properties, owing to the mesoporous nature of the original sponge template [13, 17].

2.3.2.8 Pastes and Packed Powders

A simple workaround for aforementioned issues with bioactive glass monoliths is to pack ceramic powder into a bone defect, conformally filling the wound with a porous compact. Though this application does not technically produce a scaffold, many of the desired characteristics of a tissue scaffold are present. However, packed powder has effectively zero mechanical strength, and no dimensional stability. Issues with material migration limit the efficacy of this repair method [17]. Composite pastes comprised of bioceramics and formable binders, primarily used as bone cements, have been developed to address dimensional stability, but lack porosity [50]. Despite these challenges, many granular powders and pastes are clinically available, such as NovaBone® Morsels or ZimmerBiomet Equivabone® [17]. Though these formable methods are easy to apply conformally, they lack load-bearing capacity, dimensional stability (in packed powders), or porosity (in pastes).

2.4 Soluble Polysilicates and Sodium Silicate

Soluble polysilicates are liquid silicate alkali compounds (colloquially known as “liquid glass” or “waterglass”), derived from soda, potash, or lithia. Sodium silicates $((\text{Na}_2\text{O})_x \cdot \text{SiO}_2)_y$ are most common, comprised of compounds such as sodium metasilicate (Na_2SiO_3), sodium orthosilicate (Na_4SiO_4), sodium pyrosilicate ($\text{Na}_6\text{Si}_2\text{O}_7$), or some combination thereof [51, 52]. The ratio of sodium oxide (Na_2O) to silicon dioxide (SiO_2) in sodium silicates varies between 2:1 to 3.75:1, with varying dilution, pH, and viscosity [53].

Thus, the term ‘sodium silicate’ does not refer to one particular material, but rather a class of materials. The compositional range of liquid sodium silicates is shown in region 9 of the ternary phase diagram in Figure 2-4. These liquid polysilicates react with carbon dioxide gas to form a rigid, glassy silicate gel: hence the name “waterglass”.

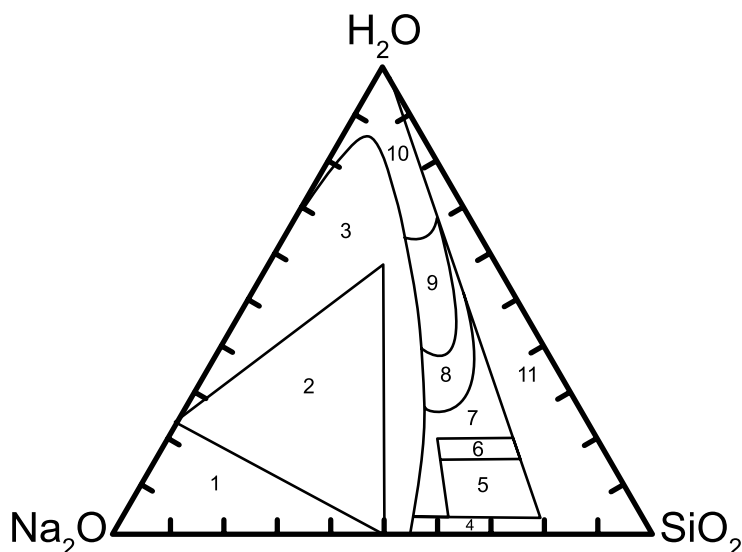


Figure 2-4. Ternary phase diagram of the $\text{SiO}_2\text{-Na}_2\text{O-H}_2\text{O}$ system. Aqueous sodium silicates are typically commercially produced in Region 9. Other regions are as follows: (1) anhydrous sodium orthosilicate and mixtures with NaOH; (2) crystalline alkaline silicates; (3) uneconomical partially crystallised mixtures; (4) glasses; (5) uneconomical hydrated glasses; (6) dehydrated liquids; (7) uneconomical semi-solids; (8) economical viscous liquids; (9) typical commercial liquids; (10) dilute liquids; (11) unstable liquids and gels. Adapted from Vail and Wills, 1952 [54].

The first record of liquid sodium silicate is attributed to Pliny the Elder (Gaius Plinius Secundus, AD 23/24-79) [55], who described a “strange translucent liquid [that] flowed forth in streams” [56] when Phoenician mariners heated sodium nitrate salts in contact with sand [57]. Soluble silicates were fabricated and documented by many alchemists and scholars in the 16th and 17th centuries, including Basilus Valentinus, Georgius Agricola, and Giambattista della Porta [57, 58]. Industrial use of aqueous sodium silicate was pioneered by Johann Nepomuk von Fuchs in 1825, who published a treatise outlining the industrial production and commercial use of soluble silicates. In subsequent years, liquid sodium silicates have been used in detergents, deflocculating agents for water treatment, adhesives,

corrugated paper production, cements, wood veneers, corrosion inhibitors, concrete, food preservatives, surgical bandages, and as a binder in sand casting [58, 57, 53].

One of the most common modern uses of soluble sodium silicates—hardening sand-casting cores—was patented in 1898 [59], became established in industry in the late 1950s, and became ubiquitous in the 1970s with the advent of additives and improved properties [60]. This process is remarkably similar to the concept proposed in this thesis—but instead of binding grains of bioactive glass, sodium silicate is used to bind grains of sand. These sand-sodium silicate composites harden and set when exposed to carbon dioxide gas, and are used as moulds, or ‘cores’, for metals casting [61].

Though sodium silicates have been observed for over 2000 years, and produced and utilised for over 500 years, the setting reaction that occurs with carbon dioxide gas has yet to be sufficiently confirmed [60]. Though the exact nature of the reaction is unclear, the prevailing theory can be summarised by Figure 2-5, below. The addition of CO₂ gas decreases the pH of the liquid silicate, leading to the formation of mono-silicic acid (Si(OH)₄) and sodium carbonate. The mono-silicic acid is unstable and polymerises with neighbouring OH-groups to form siloxane (Si–O–Si) bonds. This reaction results in the elimination of water and syneresis of the silica gel. The polymerised polysilicates are not of uniform size, and the size and distribution of silicate groups varies with the ratio and concentration of a given silicate solution.

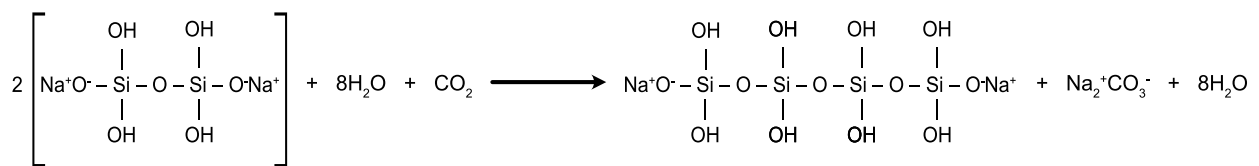


Figure 2-5. Reaction of aqueous sodium silicate with carbon dioxide gas, illustrating the formation of polysilicates from unstable (mono-silicic acid) due to the reduction of pH. Adapted from Yaw, 1982 [61].

Hydration of a 'set' sodium silicate gel (herein referred to as solid sodium silicate) can result in multiple cases of behaviour, contingent on many factors such as concentration of $(\text{Na}_2\text{O})_x \cdot \text{SiO}_2)_y$ species, presence of other ions, molar ratio, concentration of carbon dioxide gas, pH, and temperature. The behaviour of solid sodium silicate in aqueous solutions is highly dependent on pH, with pH values below 11.0 capable of causing precipitation or aggregation of sodium silicate species, depending on concentration [62]. In saline solutions, it has been posited that chloride ions are not directly involved in the gel formation process [62], while sodium ions have a marked influence on the hydrated gel, truncating the polymeric chains of siliceous material and lowering the structural integrity and cohesiveness of the gel [61]. Upon 're-hydration', solid silicate gels are capable of becoming fully soluble in an aqueous solution, again dependent on the aforementioned factors.

2.4.1 Sodium Silicates in Biomedical Applications

More recently, soluble silicates have been used in the fabrication of dense calcium phosphate-based bone cements [63, 64, 65] that are employed to hold metallic prosthetics in place. These materials have been shown to be biodegradable and resorbable, with sufficient compressive strength. However, these bone cements are not scaffolds, nor synthetic bone grafts; they do not fill voids, are typically not porous, nor inherently anti-bacterial, and do not permit rapid in-growth of bone tissue.

The majority of promising biomedical applications of sodium silicates are in composites, wherein the self-setting and mechanical properties of sodium silicate is leveraged with bioactive materials, such as bioactive glasses and calcium phosphate-based materials [66]. Sodium silicate gel coatings on polymeric substrates have been shown to biomineralise when immersed in simulated body fluid [67], acting as a nucleating agent for calcium phosphate minerals. Though their use is far from widespread, a few reports exist indicating the nascent promise of sodium silicates for biomedical materials.

2.5 Design of Synthetic Bone Tissue Scaffolds

2.5.1 Design Criteria in Literature

As aforementioned, the design of a successful bone tissue substitute material requires mapping the advantages of autografts to design criteria, ensuring that no additional limitations are introduced, and eliminating the need for additional surgeries and the risk of infection. Many reports exist defining these criteria, with a large degree of consensus between them [13, 46, 17, 35, 14, 15, 25, 68, 50]. Three sets of such criteria are provided as an example below:

Chen et al. established seven criteria: (1) the ability to deliver cells, (2) osteoconductivity, (3) biodegradability, (4) mechanical properties, (5) porous structure, (6) fabrication, and (7) commercialisation potential [46]. The *ability to deliver cells* was defined as the ability to foster cell attachment, differentiation, and proliferation without toxic effects; i.e., Class A bioactivity. *Osteoconductivity*, as defined in Chapter 2.2.1, refers to the ability of an implant to develop a functional bond with surrounding tissues. *Biodegradability* requires the material to degrade at rates suitable for tissue replacement. *Mechanical properties* were defined as “sufficient to provide mechanical stability to constructs in load bearing sites prior to synthesis of new extracellular matrix by cells” ([46], p. 5). Porosity was required to be open, interconnected, greater than 90%, with pore sizes between 300-500 μm . *Fabrication* was established to require that scaffolds be able to be produced to the unique geometric requirements of each patient. *Commercialisation potential* required feasibility for commercial production, distribution, and use.

Baino et al. defined nine criteria: (1) geometry, (2) bioactivity, (3) biocompatibility, (4) chemical and biological stability/biodegradability, (5) porous structure, (6) mechanical competence/compliance, (7) biological properties, (8) fabrication, and (9) commercialisation potential [13]. *Geometry* refers to the ability of a material to fill complex, 3-D bone defects. *Bioactivity* was defined as the ability to form a stable bond with surrounding tissues without the formation of scar or fibrous tissue. *Biocompatibility* was

established to require the ability of the material to support cellular activity without any toxic effects to the body. *Chemical and biological stability/biodegradability* was defined as either the ability to remain *in situ* indefinitely (if desired), or to degrade at an appropriate rate as the implant is replaced by host tissue. *Porous structure* required scaffold materials to have a high surface-area-to-volume ratio and interconnected pores with a minimum pore size of 100 μm . *Mechanical competence/compliance* referred to the material's ability to be withstand implantation and exhibit load-bearing capacity appropriate for the application, with sufficient compliance to soft tissues. *Biological properties* were defined as the ability to induce cell differentiation, angiogenesis, or an antibacterial effect, as required by the intended application. *Fabrication* requires scaffolds to be able to be produced in desired geometries, and *commercialisation potential* was defined as the ability of a scaffold to be produced sterile via automation, to standards necessary for clinical use.

Fiume et al. posited eight criteria: (1) biocompatibility/bioactivity, (2) bone bonding, (3) porous structure, (4) mouldability, (5) suitable degradation rate, (6) maintenance of properties during degradation, (7) fabrication and scalability, and (8) sterilisation [17]. *Biocompatibility/bioactivity* requires scaffold materials to promote anchoring of osteogenic cells without triggering an immune response or releasing cytotoxic substances. *Bone bonding* was defined as the “*capability to create a bond with living bone without the formation of a scar layer at the interface*” ([17], p. 17). *Porous structure* referred to the need for an interconnected, cell-permeable, highly porous (80-90 vol%) structure with pore diameters from 10-500 μm . *Mouldability* was defined as the ability of a scaffold material to be adapted to any shape and size of bone defects. *Suitable degradation rate* requires bone scaffolding materials to degrade at a rate that matches the growth of new bone, and *maintenance of properties during degradation* refers to appropriate bioactivity and mechanical properties during the resorption/new tissue growth process. *Fabrication and scalability* was defined as low-cost, feasible commercial production of the scaffold, and *sterilisation* requires scaffolds to be manufactured according to biomedical device regulations.

2.5.2 Design Criteria in This Research

In order to develop a synthetic bone graft material, the research within this thesis was evaluated against a set of design criteria, established by synthesising the concepts found in literature (Chapter 2.5.1). Six design criteria were determined to be necessary in the design of a successful synthetic bone graft, detailed below. In addition to these criteria, the work presented in this thesis was developed with the guiding philosophy of operating room feasibility and ease-of-use, by limiting commercialisation barriers by requiring no additional infrastructure or complex fabrication facilities.

The six design criteria used in this research were defined and justified as such:

1. Formability is necessary for successful synthetic bone tissue scaffolds, as it allows the material to conform to the unique surface of a bone defect—bone defects often have irregular, undercut geometries, and a bone graft material must be in intimate contact with the entire defect surface in order for bone regrowth to occur [13]. In addition, a bone graft that is completely conformal can result in enhanced load-bearing capabilities (due to a reduction in stress concentrations) and permit complete resorption (due to increased vascularisation). In this context, formability relates to the ability to be manipulated to fill a variety of geometries in real time (i.e., no advanced preparation or fabrication of the scaffold)—the material would be fabricated only when needed in surgery, by the surgeon for the specific wound to be treated.

2. Geometric stability of a bone tissue scaffold after implantation is necessary for complete healing—if the scaffold material is able to migrate from the wound site after implantation, bone regrowth may be reduced or entirely prevented. The scaffold must be able to remain in the wound geometry until sufficient healing and/or resorption are complete [13].

3. Successful scaffolds must have open, interconnected porosity networks with a large surface area to volume ratio [13]. Pores of at least 50-100 μm are necessary for tissue infiltration and the transport of osteoblasts and osteoprogenitor cells (cells necessary for

new bone growth to occur) [8, 13]. Highly porous bone graft materials with large porous interconnects have increased bioactivity and subsequent healing [69], but reduced mechanical strength. It is necessary to strike a balance between porosity and load-bearing capabilities, as both are required for a successful bone graft substitute [23].

4. A successful bone tissue scaffold material should possess **load-bearing capacity**, as the bone defect will encounter stresses during healing, even if patients are bedridden. However, completely restricting patients' movement results in severe complications; elderly patients and patients with osteoporosis are especially prone to losing additional bone mass, developing bed sores, and worsening healing outcomes. Synthetic bone tissue scaffolds do not necessarily need to be as strong as bone itself, as the defect site can be immobilized in a cast during healing, but must be able to withstand minor stresses in an ambulatory patient. As aforementioned, only interim strength is necessary to stabilize the implant until it has resorbed.

5. **Bioactivity**, in the context of bone graft substitutes, refers to the osteoconductivity, osteogenicity, and osteoinductivity of the material—in essence, the ability of the material to induce the regrowth of bone. Bioactivity is essential for a successful bone graft, as it is the property that induces healing and repair of a bone defect. Class A bioactivity is required for a successful bone graft substitute material.

6. Finally, an ideal bone graft will exhibit **resorbability**, as a permanent implant will always carry the risk of complications—peri-implantitis, which is inflammation around an osseointegrated implant that results in the loss of supporting bone, has an incidence rate of 80% in dental bone grafts [70, 71]. The interface between a foreign object and healed bone will always be weaker than native bone—if a bone graft material can completely resorb into the body upon healing, leaving nothing but the patient's own bone, the lifelong risks of an implant are eliminated. Throughout the resorption process, the mechanical properties and geometric stability of the scaffold must be maintained at a rate that is matched to the regrowth of new bone such that material migration or loss of structural support does not occur, and only release degradation products that are biologically safe.

The bone tissue scaffold technologies introduced in Chapter 2.3.2 are evaluated against these established design criteria in Table 2-1. No current technology is capable of fulfilling all design criteria simultaneously; notably, processing routes that produce load-bearing, geometrically stable materials do not produce formable scaffolds, and routes that are formable lack geometric stability or load-bearing capacity.

	Sol-gel Synthesis	Foaming Methods	Porogens	Additive Manufacturing	Sintering and Thermal Consolidation	Freeze-drying and Thermal Separation	Sponge Replication	Pastes	Packed Powders
Design Criteria	Formability	✗	✗	✗	✗	✗	✗	✓	✓
	Geometric Stability	✓	✓	✓	✓	✓	✓	✓	✗
	Porosity	✓	✓	✓	✓	✓	✓	✗	✓
	Load-bearing Capacity	✓	✓	✓	✓	✓	✓	✗	✗
	Bioactivity	✓	✓	✓	✓	✓	✓	✓	✓
	Resorbability	✓	✓	✓	✓	✓	✓	✗	✓

Table 2-1. Current synthetic bone tissue scaffold processing methods evaluated against the design criteria used in this research. No current technology fulfils all criteria simultaneously.

Bibliography – Chapter Two

- [1] L. Gaviria, L. Actis, T. Guda and J. Ong, “Bone Grafting Evolution,” in *Translating Biomaterials for Bone Graft: Bench-top to Clinical Applications*, Boca Raton, FL, CRC Press, 2017, pp. 3-21.
- [2] Centres for Disease Control and Prevention, “10 Leading Causes of Nonfatal Injury, United States,” National Center for Injury Prevention and Control, CDC, Atlanta, GA, 2016.
- [3] F. A. Al-Mulhim, M. A. Baragbah, M. Sadat-Ali, A. S. Alomran and M. Q. Azam, “Prevalence of Surgical Site Infection in Orthopedic Surgery: A 5-year Analysis,” *International Surgery*, vol. 99, pp. 264-268, 2014.
- [4] A. Bachoura, T. G. Guitton, R. M. Smith, M. S. Vrahas, D. Zurakowski and D. Ring, “Infirmary and Injury Complexity are Risk Factors for Surgical-site Infection after Operative Fracture Care,” *Clinical Orthopaedics and Related Research*, vol. 469, no. 9, pp. 2621-2630, 2011.
- [5] M. Bhola, A. L. Neely and S. Kolhatkar, “Immediate Implant Placement: Clinical Decisions, Advantages, and Disadvantages,” *Journal of Prosthodontics*, vol. 17, no. 7, pp. 576-81, 2008.
- [6] M. Ahn, K. An, J. Choi and D. Sohn, “Immediate Loading with Mini Dental Implants in the Fully Edentulous Mandible,” *Implant Dentistry*, vol. 13, no. 4, pp. 367-72, 2004.
- [7] J. S. Silber, G. D. Anderson, S. D. Daffner, B. T. Brislin, M. J. Leland, A. S. Hilibrand, A. R. Vaccaro and T. J. Albert, “Donor Site Morbidity After Anterior Iliac Crest Bone Harvest for Single-Level Anterior Cervical Discectomy and Fusion,” *Spine*, vol. 28, no. 2, pp. 134-139, 2003.
- [8] S. V. Dorozhkin, “Calcium Orthophosphates as Bioceramics: State of the Art,” *Journal of Functional Biomaterials*, vol. 1, pp. 22-107, 2010.
- [9] V. Campana, G. Milano, E. Pagano, M. Barba, C. Cicione, G. Salonna, W. Lattanzi and G. Logroscino, “Bone substitutes in orthopaedic surgery: from basic science to clinical practice,” *Journal of Materials Science: Materials in Medicine*, vol. 25, no. 10, pp. 2445-2461, 2014.

- [10] S. N. Parikh, "Bone graft substitutes: past, present, future.," *Journal of Postgraduate Medicine*, vol. 48, no. 2, pp. 142-148, 2002.
- [11] Datamonitor, "United States - Bone Graft Substitutes," Datamonitor, New York, NY, 2001.
- [12] American Academy of Orthopaedic Surgeons, "Bone-Graft Substitutes: Facts, Fictions & Applications," American Academy of Orthopaedic Surgeons, New Orleans, LA, 2003.
- [13] F. Baino, G. Novaira and C. Vitale-Brovarone, "Bioceramics and scaffolds: A winning combination for tissue engineering," *Frontiers in Bioengineering and Biotechnology*, vol. 3, pp. 1-17, 2015.
- [14] Z. Gou, A. Ballo and W. Xia, "Chapter 5: Biomimetic Preparation and Biomineralization of Bioceramics," in *Advanced Bioactive Inorganic Materials for Bone Regeneration and Drug Delivery*, Rolla, FL, CRC Press, 2013, pp. 117-146.
- [15] H. Qu, H. Fu, Z. Han and Y. Sun, "Biomaterials for bone tissue engineering scaffolds: A review," *RSC Advances*, vol. 9, no. 45, pp. 26252-26262, 2019.
- [16] X. Zhao, "Introduction to bioactive materials in medicine," in *Bioactive Materials in Medicine*, New York, Elsevier, 2011, pp. 1-13.
- [17] E. Fiume, J. Barberi, E. Verné and F. Baino, "Bioactive Glasses: From Parent 45S5 Composition to Scaffold-Assisted Tissue-Healing Therapies," *Journal of Functional Biomaterials*, vol. 9, no. 24, pp. 1-33, 2018.
- [18] L. L. Hench and E. Fielder, "3.1.4 Biological Gel-Glasses," in *Sol-Gel Technologies for Glass Producers and Users*, New York, Springer, 2004, p. 153.
- [19] L. L. Hench, D. L. Wheeler and D. C. Greenspan, "Molecular Control of Bioactivity in Sol-Gel Glasses," *Journal of Sol-Gel Science and Technology*, vol. 12, pp. 245-250, 1998.
- [20] P. Ducheyne and Q. Qiu, "Bioactive ceramics: The effect of surface reactivity on bone formation and bone cell function," *Biomaterials*, vol. 20, pp. 2287-2303, 1999.
- [21] L. Varila, S. Fagerlund, T. Lehtonen, J. Tuominen and L. Hupa, "Surface reactions of bioactive glasses in buffered solutions," *Journal of the European Ceramic Society*, vol. 32, pp. 2757-2763, 2012.

- [22] M. N. Rahaman, D. E. Day, B. S. Bal, Q. Fu, S. B. Jung, L. F. Bonewald and A. P. Tomsia, "Bioactive glass in tissue engineering," *Acta Biomaterialia*, vol. 7, no. 6, pp. 2355-2373, 2011.
- [23] J. R. Jones, "Review of bioactive glass: From Hench to hybrids," *Acta Biomaterialia*, vol. 9, pp. 4457-4486, 2013.
- [24] A. Lotsari, A. K. Rajasekharan, M. Halvarasson and M. Andersson, "Transformation of amorphous calcium phosphate to bone-like apatite," *Nature Communications*, vol. 9, no. 1, pp. 1-11, 2018.
- [25] L. L. Hench, D. E. Day, W. Höland and V. M. Rheinberger, "Glass and Medicine," *International Journal of Applied Glass Science*, vol. 1, no. 1, pp. 104-117, 2010.
- [26] P. Li, C. Ohtsuki, T. Kokubo, K. Nakanishi, N. Soga, T. Nakamura and T. Yamamuro, "Apatite Formation Induced by Silica Gel in a Simulated Body Fluid," *Journal of the American Ceramic Society*, vol. 75, no. 8, pp. 2094-2097, 1992.
- [27] G. Jell, I. Notingher, O. Tsigkou, P. Notingher, J. M. Polak, L. L. Hench and M. M. Stevens, "Bioactive glass-induced osteoblast differentiation: A noninvasive spectroscopic study," *Journal of Biomedical Materials Research*, vol. 86A, no. 1, pp. 31-40, 2007.
- [28] J. Wilson and S. B. Low, "Bioactive ceramics for periodontal treatment: comparative studies in the Patus monkey.," *Journal of Applied Biomaterials*, vol. 3, no. 2, pp. 123-129, 1992.
- [29] T. Albrektsson and C. Johansson, "Osteoinduction, osteoconduction and osseointegration," *European Spin Journal*, vol. 2S, pp. 96-101, 2001.
- [30] L. L. Hench, "The story of Bioglass (R)," *Journal of Materials Science: Materials in Medicine*, vol. 17, pp. 967-978, 2006.
- [31] R. Lanza, J. Gearhart, B. Hogan, D. Melton, R. Pedersen, J. Thomson and M. West, *Handbook of Stem Cells*, New York: Elsevier, 2004.
- [32] T. L. McCarthy, M. Centrella and E. Canalis, "Insulin-like growth factor (IGF) and bone.," *Connective Tissue Research*, vol. 20, no. 1-4, pp. 277-282, 1989.
- [33] S. Boonrungsiman, E. Gentleman, R. Carzaniga, N. D. Evans, D. W. McComb, A. E. Porter and M. M. Stevens, "The role of intracellular calcium phosphate in osteoblast-mediated

- bone apatite formation," *Proceedings of the National Academy of Sciences of the United States of America*, vol. 109, no. 35, pp. 14170-14175, 2012.
- [34] A. F. Mavrogenis, R. Dimitriou, J. Parvizi and G. C. Babis, "Biology of implant osseointegration.," *Journal of Musculoskeletal and Neuronal Interactions*, vol. 9, no. 2, pp. 61-71, 2009.
- [35] L.-C. Gerhardt and A. R. Boccaccini, "Bioactive Glass and Glass-Ceramic Scaffolds for Bone Tissue Engineering," *Materials*, vol. 3, pp. 3867-3910, 2010.
- [36] A. R. Boccaccini, Q. Chen, L. Lefebvre, L. Gremillard and J. Chevalier, "Sintering, crystallisation and biodegradation behaviour of Bioglass-derived glass-ceramics," *Faraday Discussions*, vol. 136, pp. 27-44, 2007.
- [37] J. A. Sanz-Herrera and A. R. Boccaccini, "Modelling bioactivity and degradation of bioactive glass based tissue engineering scaffolds," *International Journal of Solids and Structures*, vol. 48, no. 2, pp. 257-268, 2011.
- [38] I. Izqueirido-Barba, A. J. Salinas and M. Vallet-Regí, "Bioactive Glasses: From Macro to Nano," *International Journal of Applied Glass Science*, vol. 4, no. 2, pp. 149-161, 2013.
- [39] K. R. Rust, G. T. Singleton and P. J. Antonelli, "Bioglass middle ear prosthesis: long-term results," *American Journal of Otolaryngology*, vol. 17, pp. 371-374, 1996.
- [40] L. L. Hench, "Challenges for Bioceramics in the 21st Century," *American Ceramic Society Bulletin*, vol. 84, no. 9, pp. 18-21, 2005.
- [41] J. Wilson, A. Yli-Urpo and H. Risto-Pekka, "Bioactive glasses: clinical applications," in *An Introduction to Bioceramics*, Singapore, World Scientific, 1993, pp. 63-74.
- [42] S. Hu, J. Chang, M. Liu and C. Ning, "Study on antibacterial effect of 45S5 Bioglass," *Journal of Materials Science: Materials in Medicine*, vol. 20, no. 1, pp. 281-6, 2009.
- [43] P. Li, F. Zhang and T. Kokubo, "The effect of residual glassy phase in a bioactive glass-ceramic on the formation of its surface apatite layer in vitro," *Journal of Materials Science: Materials in Medicine*, vol. 3, pp. 452-256, 1992.
- [44] C. Wu, J. Chang and Y. Xiao, "Chapter 1: Mesoporous Bioactive Glasses for Drug Delivery and Bone Tissue Regeneration," in *Advanced Bioactive Inorganic Materials for Bone Regeneration and Drug Delivery*, Boca Raton, FL, CRC Press, 2013, pp. 1-24.

- [45] G. Kaur, G. Pickrell, N. Sriranganathan, V. Kumar and D. Homa, "Review and state of the art: Sol-gel and melt quenched bioactive glasses for tissue engineering.," *Journal of Biomedical Materials Research - Part B: Applied Biomaterials*, vol. 104, no. 6, pp. 1248-1275, 2016.
- [46] Q. Chen, J. Roether and A. Boccaccini, "Tissue Engineering Scaffolds from Bioactive Glass and Composite Materials," *Topics in Tissue Engineering*, vol. 4, no. 6, pp. 1-27, 2008.
- [47] Y. Zhang and C. Wu, "Chapter 7: Bioactive Inorganic and Organic Composite Materials for Bone Regeneration and Gene Delivery," in *Advanced Bioactive Inorganic Materials for Bone Regeneration and Drug Delivery*, Rolla, FL, CRC Press, 2013, pp. 177-211.
- [48] Y. Luo, A. Lode, C. Wu and M. Gelinsky, "Chapter 4: 3D Plotting of Bioceramic Scaffolds under Physiological Conditions for Bone Tissue Engineering," in *Advanced Bioactive Inorganic Materials for Bone Regeneration and Drug Delivery*, Rolla, FL, CRC Press, 2013, pp. 82-116.
- [49] L. Roseti, V. Parisi, M. Petretta, C. Cavallo, G. Desando, I. Bartolotti and B. Grigolo, "Scaffolds for Bone Tissue Engineering: State of the art and new perspectives," *Materials Science and Engineering C*, vol. 78, pp. 1246-1262, 2017.
- [50] M. Navarro, A. Michiardi, O. Castaño and J. A. Planell, "Biomaterials in orthopaedics," *Journal of the Royal Society: Interface*, vol. 5, no. 27, pp. 1137-1158, 2008.
- [51] G. Lagaly, W. Tufar, A. Minihan and A. Lovell, "Silicates," in *Ullman's Encyclopedia of Industrial Chemistry*, vol. 32, Weinheim, Wiley-VCH Verlag, 2012, pp. 509-572.
- [52] S. Ebnesajjad, "5.20.1: Soluble Silicates (Potassium and Sodium Silicate)," in *Adhesives Technology Handbook (Second Edition)*, Norwich, NY, William Andrew Publishing, 2009, pp. 63-135.
- [53] H.-J. Engelhardt and L. E. von Borstel, "The behaviour of sodium silicate solutions (water glass) in the saline environment and their use in salt mining," *Zeitschrift der Deutschen Gesellschaft für Geowissenschaften (German Journal of Geology)*, vol. 165, no. 1, pp. 115-122, 2014.
- [54] J. G. Vail and J. H. Wills, "Chapter 2: Present Practices," in *Soluble Silicates - Their Properties and Uses, Volumes 1-2; American Chemical Society, Monograph Series*, New York, NY, Book Division, Reinhold Publishing Corporation, 1952, pp. 16-43.

- [55] J. F. Healy, "18.2: Technology: Glass," in *Pliny the Elder on Science and Technology*, Oxford, UK, Oxford University Press, 1999, pp. 350-358.
- [56] Pliny, "Natural History, Volume X: Books 36-37. Translated by D. R. Eichholz," in *Loeb Classical Library 419*, Cambridge, MA, Harvard University Press, 1962, pp. 150-151.
- [57] H. B. Ellis, "Stabilization of soils with lime and sodium silicate," Iowa State University, Ames, IA, 1963.
- [58] J. G. Vail and J. H. Wills, "Chapter 1: The Beginnings," in *Soluble Silicates - Their Properties and Uses, Volumes 1-2; American Chemical Society, Monograph Series*, New York, NY, Book Division, Reinhold Publishing Corporation, 1952, pp. 4-15.
- [59] D. V. Atterton, "The carbon-dioxide process," *AFS Transactions*, vol. 64, pp. 14-18, 1956.
- [60] D. V. Atterton and J. V. Stevenson, "The Carbon Dioxide Process: A Look Back -- A Look Forward," *AFS Transactions*, vol. 89, pp. 55-64, 1981.
- [61] Y. Owusu, "Physical-chemistry study of sodium silicate as a foundry sand binder," *Advances in Colloid and Interface Science*, vol. 18, no. 1-2, pp. 57-91, 1982.
- [62] M. Tognonvi, S. Rossignol and J. Bonnet, "Physical-chemistry of sodium silicate gelation in an alkaline medium," *Journal of Sol-Gel Science and Technology*, vol. 58, no. 3, pp. 625-635, 2011.
- [63] V. S. Komlev, J. V. Rau, M. Fosca, A. S. Fomin, A. N. Gurin, S. M. Barinov and R. Caminiti, "Single-phase bone cement based on dicalcium phosphate dihydrate powder and sodium silicate solution," *Materials Letters*, vol. 73, pp. 115-118, 2012.
- [64] H. Zhou, T. J. Luchini, S. Bhaduri and L. Deng, "Silicon (Si) containing bone cements: a review," *Materials Technology: Advanced Biomaterials*, vol. 30, no. B4, pp. 229-236, 2015.
- [65] S. M. Kenny and M. Buggy, "Bone cements and fillers: a review," *Journal of Materials Science: Materials in Medicine*, vol. 14, no. 11, pp. 923-938, 2003.
- [66] Z. Huan and J. Chang, "Effect of sodium carbonate solution on self-setting properties of tricalcium silicate bone cement," *Journal of Biomaterials Applications*, vol. 23, no. 3, pp. 247-262, 2008.

- [67] A. L. Oliveira, P. B. Malafaya and R. L. Reis, "Sodium Silicate Gel Induced Self-Mineralization of Different Compact and Porous Polymeric Structures," *Key Engineering Materials*, Vols. 192-195, no. Bioceramics 13, pp. 75-78, 2001.
- [68] P. Chocholata, V. Kulda and B. Vaclav, "Fabrication of scaffolds for bone-tissue regeneration," *Materials*, vol. 12, no. 568, pp. 1-25, 2019.
- [69] L. L. Hench, "Bioceramics," *Journal of the American Ceramic Society*, vol. 81, no. 7, pp. 1705-1728, 1998.
- [70] A. Mombelli and N. P. Lang, "The diagnosis and treatment of peri-implantitis," *Periodontology 2000*, vol. 17, no. 1, pp. 63-76, 1998.
- [71] N. Zitmann and T. Berglundh, "Definition and prevalence of peri-implant diseases," *Periodontology*, vol. 35, no. s8, pp. 268-291, 2008.
- [72] B. M. Holzapfel, J. C. Reichert, J.-T. Schantz, U. Gbureck, L. Rackwitz, U. Nöth, F. Jakob, M. Rudert, J. Groll and D. W. Hutmacher, "How smart do biomaterials need to be? A translational science and clinical point of view," *Advanced Drug Delivery Reviews*, vol. 65, no. 4, pp. 581-603, 2013.

Chapter Three

Experimental Design¹

3.1 Materials

All composite scaffolds were fabricated with two components: bioactive glass frit and an aqueous sodium silicate liquid. The bioactive glass used in the composites was unannealed +355 μm 45S5 bioactive glass frit (Mo-Sci Health Care, L.L.C., North Rolla, MO), shown in Figure 3-1c. Size distribution was verified using optical particle size analysis, further explored in Chapter 3.3.1 Imaging Particle Size Analysis. This size distribution has been shown to maintain open porous networks when combined with a binder phase [1].

Aqueous sodium silicate solution (Fisher Scientific Company, Toronto, ON; CAS: 1344-09-08) was used as an air-setting binder in composite specimens, with a molar ratio of $\text{SiO}_2:\text{Na}_2\text{O}$ at 2.5:1. The aqueous sodium silicate used to produce the composite scaffolds differed from as-received sodium silicate due to its age (approximately 5 years); this discrepancy is further detailed in Appendix I.

Bioactive glass disc specimens were fabricated from melt cast, annealed and amorphous 12 mm diameter cylindrical rods of 45S5 bioactive glass (Figure 3-1a), also acquired from Mo-Sci Health Care.

All bioactive glass used in this study was melt-cast and amorphous with a nominal composition of 45 wt% SiO_2 , 24.5 wt% Na_2O , 24.5 wt% CaO , and 6 wt% P_2O_5 . All bioactive glass frit used was produced in the same batch.

¹ Portions of this chapter have been submitted for publication in Metallurgical and Materials Transaction A: C. M. Guzzo and J. A. Nychka, "Fabrication of a Porous and Formable Ceramic Composite Bone Tissue Scaffold at Ambient Temperature," Under Review, submitted 12-01-2019; Journal of the Mechanical Behaviour of Biomedical Materials: C. M. Guzzo and J. A. Nychka, "In vitro response of a porous and formable ceramic composite bone tissue scaffold," Under Review, submitted 02-01-2020.



Figure 3-1. 45S5 bioactive glass, as (a) 12 mm diameter rods, (b) discs sectioned from rods, and (c) +355 μm frit.

3.2 Sample Preparation

3.2.1 Preparation of Composite Scaffolds

To prepare the composite specimens, bioactive glass frit and aqueous sodium silicate were weighed with an analytical balance (P-214, Denver Instrument, Bohemia, NY, USA), combined in a polystyrene hexagonal weigh boat (15 mm depth, Fisher Scientific Company) and mixed with the bulb end of a 3.2 mL polyethylene transfer pipette (Fisher Scientific Company) for 30 seconds. Mixing was accomplished by stirring and shearing the mixture against the weigh boat, depicted schematically in Figure 3-2. The resulting paste was pressed by hand into A-, C-, and D-type custom moulds (Figure 3-3, Table 3-1). For B-type moulds, the paste was pressed into a custom mould with either a universal materials testing machine (Comprehensive Materials Testing System ME-8244, PASCO scientific, Roseville, CA; modified for constant strain rates through integration of a stepper motor and controller; SureStep 1288 oz-in, Automation Direct, GA, USA) or with a hand-operated drill press (Hausmann Xpert 12" drill press DP1200, Rona Inc., Boucherville, QC; modified with custom 12 mm diameter aluminium piston). Samples produced by each mould followed a different

testing and characterisation path, presented as a process flow diagram in Figure 3-4. The fabrication of the custom moulds is further detailed in Appendix II.

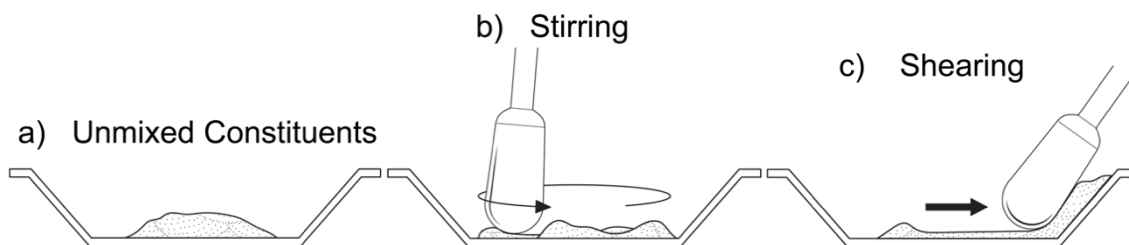


Figure 3-2. Schematic depiction of specimen mixing technique, showing (a) unmixed paste constituents, (b) stirring mixing technique, and (c) shearing mixing technique [2].

After compacting the paste to the desired height, specimens were left to set at room temperature (294 K; 21 °C). The total time elapsed between mixing and pressing was kept to less than 60 seconds to minimise the extent to which the aqueous sodium silicate reacted with atmospheric CO₂. Residence time before de-moulding varied with composition and mould size, as listed in Table 3-2. Residence times were determined through preliminary sodium silicate kinetics studies, further explored in Chapter 4.1.2; all specimens reached 75% of modelled maximum mass loss before de-moulding, and 95% of modelled maximum mass loss before characterisation. Residence time prior to de-moulding was found to be accelerated significantly through the application of compressed air to the exposed surface of the composite, whilst in the mould, such that de-moulding could be performed in under 10 minutes—however, acceleration of setting time was not in scope for this work.

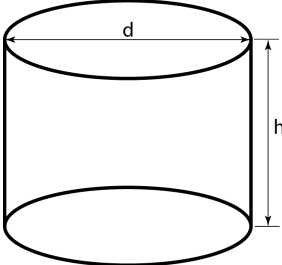
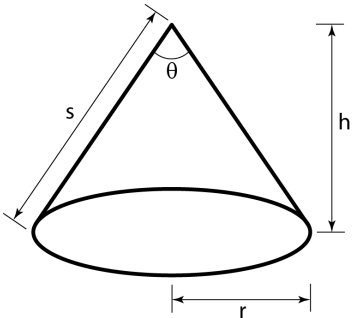
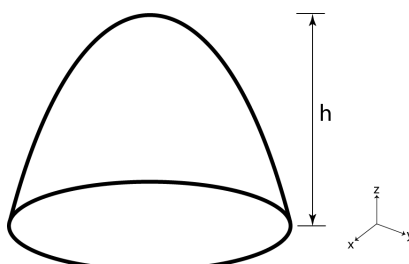
Geometry	Specimen Type	Characteristic Dimensional Description and Critical Dimensions (mm)	Characterisation Path
Right cylinder 	A	Aspect Ratio (h/d) = 0.27 h = 2.7 d = 10	Optical light microscopy (OLM); scanning electron microscopy (SEM); <i>in vitro</i> immersion; energy-dispersive x-ray spectroscopy (EDX); x-ray diffraction (XRD); Fourier-transform infrared spectroscopy (FTIR)
	B	Aspect Ratio (h/d) = 2.25 h = 27 d = 12	Mechanical strength testing (ASTM D7012); gas pycnometry; micro-computed tomography (micro-CT)
Right Circular Cone 	C	$x = r \cos \theta (h - u)/h$ $y = r \sin \theta (h - u)/h$ $z = u$ h = 20 $\theta = 28^\circ$ s = 22.4 r = 10	Formability, Geometric stability
Circular Paraboloid 	D	$z = -x^2/a^2 - y^2/b^2 + h$ a = b = 12 h = 20	Formability, Geometric stability

Table 3-1. Specimen type identification and association with materials characterisation techniques [2].

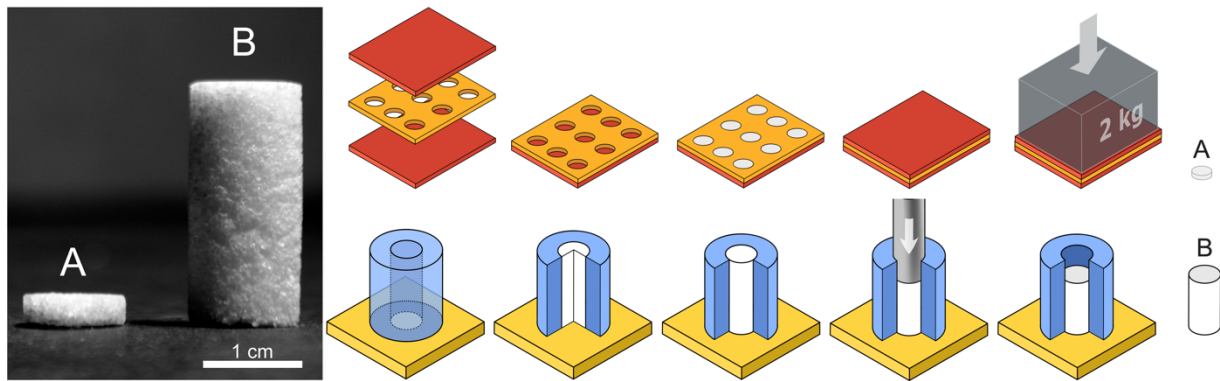


Figure 3-3. As-fabricated disc and cylinder specimens (at left). Custom moulds and procedure for moulding composite paste to produce the disc and cylindrical composite scaffold specimens [2].

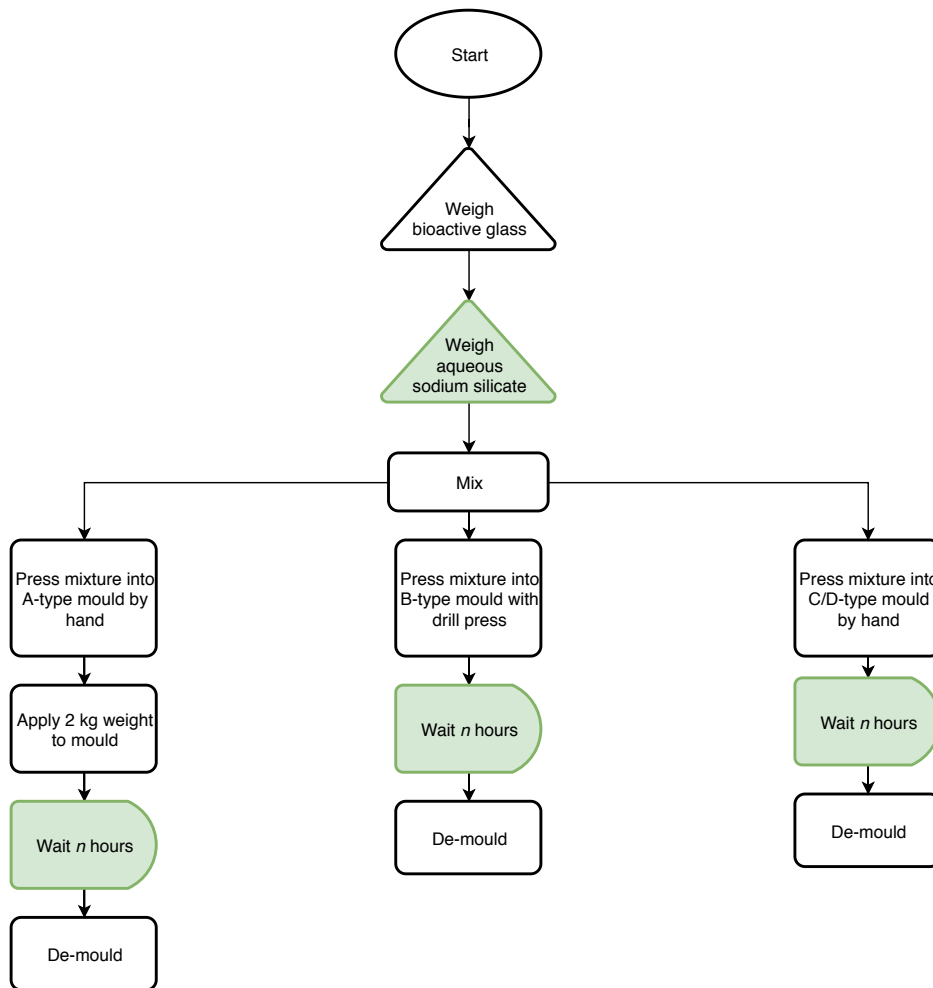


Figure 3-4. Process flow diagram depicting the composite specimen fabrication process. Green components indicate variation depending on chosen composition; for n values of mould residences times, see Table 3-2.

	Minimum residence time in mould (hours)	
	Mould A	Mould B²
Composition I	48	72
Composition II	96	120
Composition III	120	168

Table 3-2. Minimum residence moulding time for composites (prior to moulding). Additional time was accrued between de-moulding and mechanical testing [2].

² Similar minimum residence times were used for specimens of type C and D.

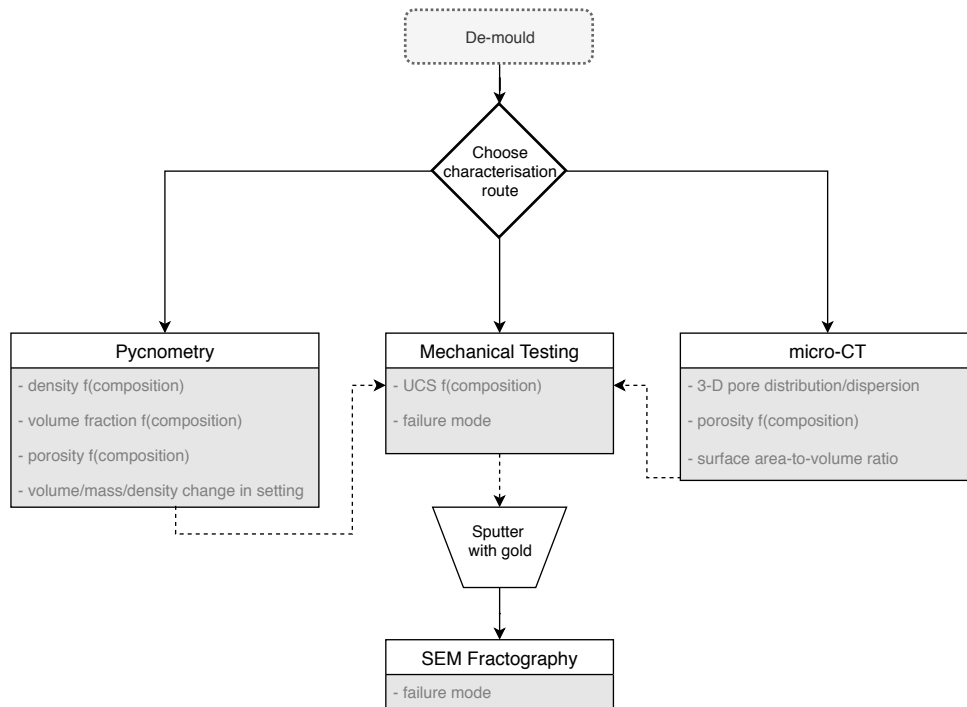
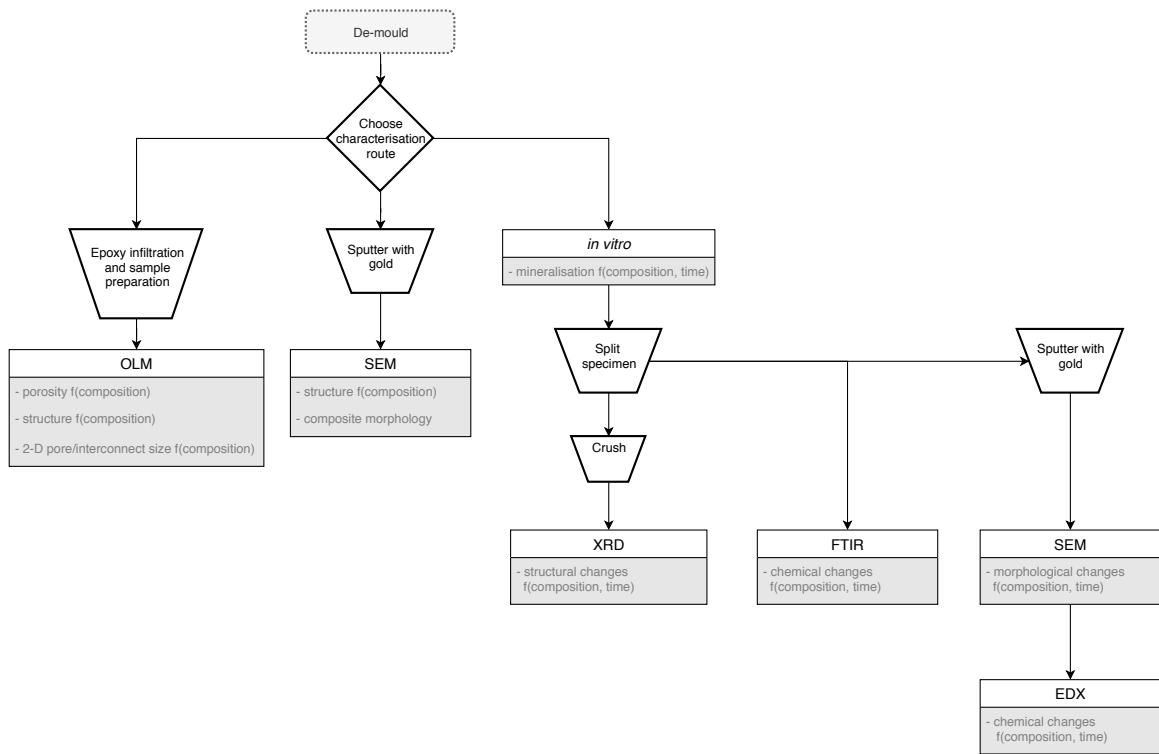


Figure 3-5. Process flow diagrams depicting the characterisation paths of (a) A-type and (b) B-type specimens. Dotted lines indicate that only certain specimens followed that characterisation path.

Three compositions were prepared with a nominal weight percent of aqueous sodium silicate. The relationships between the initial sodium silicate weight percent and the final, set volume percent of each phase are detailed in Table 3-3. The final composition values were determined using gas pycnometry, the results of which are detailed in Chapter 4.4.3.

In this work, compositions will be referred to according to their final volume percent of set binder phase—i.e., Composition I = 7.4 vol%, Composition II = 11.4 vol%, and Composition III = 16.1 vol%.

These three compositions were selected after preliminary screening trials that established the upper and lower limits of sodium silicate possible in the composite (not presented here). Composition I was the lowest proportion of sodium silicate necessary for a specimen to retain its geometry after setting, while Composition III was the highest proportion of sodium silicate found to possess formability as a paste and an open porous network after setting. Further details of the screening trials are located in Chapters 4.2 and 4.3.

	Initial wt% sodium silicate (aqueous)	Final vol% sodium silicate (set)
Composition I	18	7.4
Composition II	25	11.4
Composition III	32	16.1

Table 3-3. Relationship between initial nominal wt% of aqueous sodium silicate and final vol% of set sodium silicate of the composite specimens, determined via gas pycnometry (Chapter 4.4.3) [2].

3.2.1.1 Preparation of Optical Light Microscopy Specimens

Specimens prepared for optical light microscopy were mounted in cold-setting resin (QC Epoxy, LECO Corporation, St. Joseph, MI) tinted with blue dye (Oracet Blue B, Sigma-Aldrich Canada Co., Oakville, ON; CAS: 12769-16-3) and placed under vacuum (LAV-3 High

Vacuum Pump, Fischer Technical Company, Roselle, IL; used with Nalgene vacuum chamber, Nalge Company, Rochester, NY) and held below -140 kPa for 30 minutes to ensure infiltration of all open pores. Epoxy-mounted samples were then ground with silicon carbide grit paper (SiC Grit Paper, Allied High Tech Products, Rancho Dominguez, CA, USA), using isopropyl alcohol (Fisher Scientific Company; CAS: 67-63-0) as a lubricant. US grit sizes were used in the sequence 240, 320, 600, 800, 1200. Specimens were rinsed with isopropyl alcohol and swiped with an isopropyl alcohol-soaked lint-free cloth (KimWipes, Kimberley Clark, Irving, TX, USA) between each grinding step to avoid contamination between grit sizes.

Epoxy-mounted specimens were then polished with a diamond paste and an alcohol-based lubricant. Diamond paste sizes were used in the sequence 3, 1, and 0.5 μm . All grinding and polishing steps were conducted using a Twinprep 5 grinder/polisher (Allied High Tech Products). Samples were ultrasonically cleaned (3510 Ultrasonic Cleaner, Branson Ultrasonics, Danbury, CT, USA) in 150 mL of isopropyl alcohol for 5 minutes between each polishing step to avoid contamination between grit sizes. After all polishing steps were complete, specimens were ultrasonically cleaned in 150 mL of isopropyl alcohol for 30 minutes. The microscopy specimen preparation process, including all consumables and equipment used, is depicted as a process flow diagram in Figure 3-6.

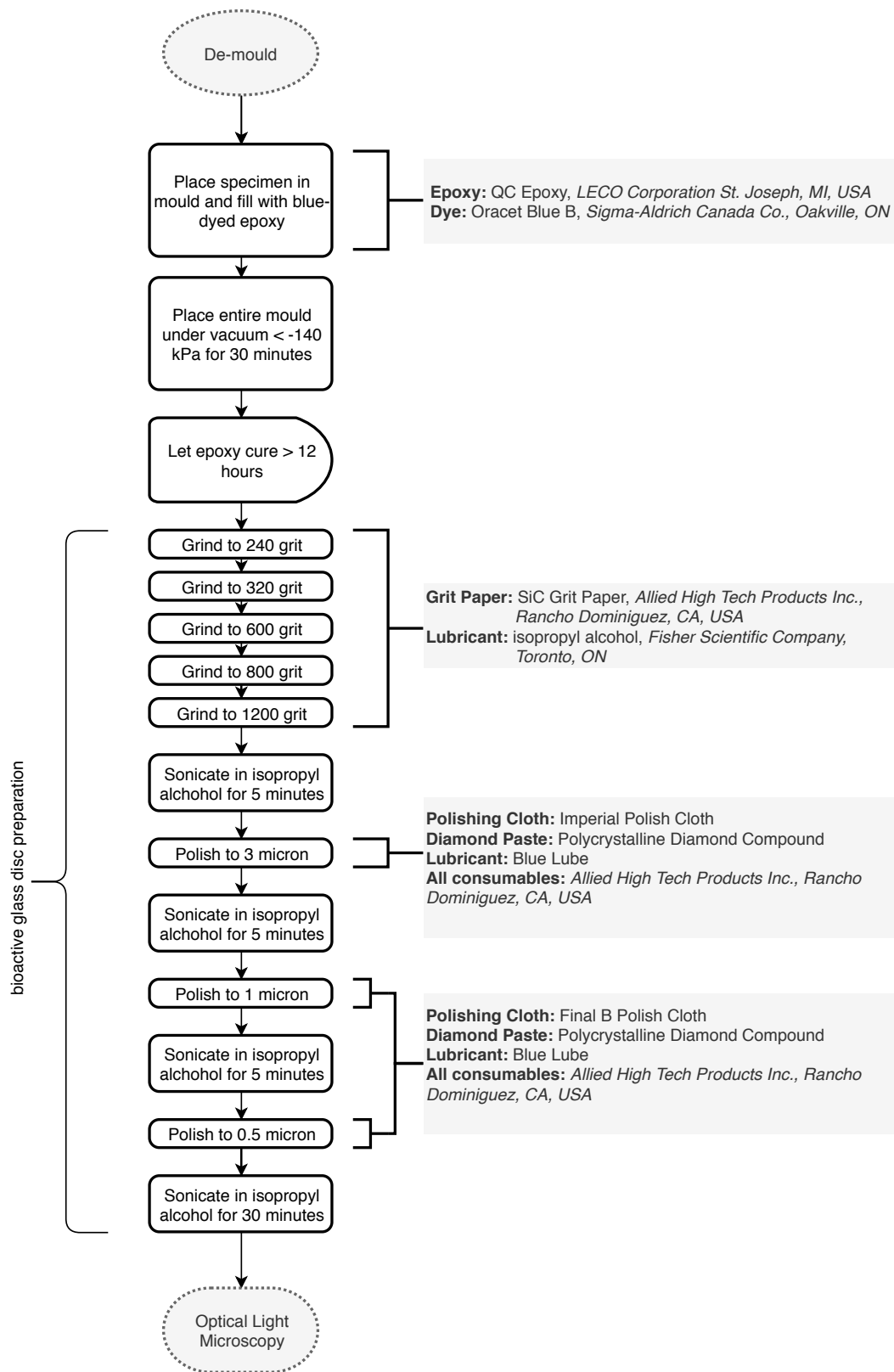


Figure 3-6. Process flow diagram depicting the sample preparation of optical light microscopy specimens. The curly brace indicates which processing steps apply to the preparation of bioactive glass disc control specimens.

3.2.2 Preparation of 45S5 Bioactive Glass

Control specimens of 45S5 bioactive glass were sectioned into 3 mm tall discs from cylindrical rods (12 mm diameter), previously shown in Figure 3-1a and b. Sectioning was conducted with a slow speed saw (Techcut 4, Allied High Tech Products Inc., Rancho Dominguez, CA, USA) equipped with a diamond wafering blade (Diamond Metal Bonded, Low Concentration, Allied High Tech Products Inc.) and isopropyl alcohol lubricant.

To facilitate grinding and polishing of the bioactive glass discs, each disc was mounted to a jig consisting of a piston and ring, according to the process described by Kashyap [3]. Prior to grinding and polishing, each disc was mounted to the piston using thermoplastic wax (Crystalbond 509, Electron Microscopy Sciences, Hatfield, PA, USA). Wax was placed on the piston, and the piston was heated to approximately 180°C on a hot plate (Cimarec HP130915, Thermo Fisher Scientific, Toronto, ON), melting the wax. The bioactive glass disc was placed on the melted wax and allowed to cool until the wax was solidified. The piston was then inserted into the ring, using the screw to hold the piston in a position where the top surface of the bioactive glass disc aligned with the surface of the ring. This alignment was accomplished by placing the jig upside down onto a Kimwipe and tightening the screw while pushing slightly harder on the piston than the ring. Alignment was verified by running the edge of a glass slide along the surface of the jig—if the glass slide caught on the glass disc, the jig was re-assembled. The assembled mounting jig with mounted specimen is shown in Figure 3-7.

The jig-mounted bioactive glass discs were then ground with silicon carbide grit paper isopropyl alcohol as a lubricant. US grit sizes were used in the sequence 240, 320, 600, 800, 1200. Glass discs were rinsed with isopropyl alcohol and swiped with an isopropyl alcohol-soaked lint-free cloth (KimWipes, Kimberley Clark, Irving, TX, USA) between each grinding step to avoid contamination between grit sizes.

The mounted discs were then polished with a diamond paste and an alcohol-based lubricant. Diamond paste sizes were used in the sequence 3, 1, and 0.5 μm . Glass discs were rinsed with isopropyl alcohol and swiped with an isopropyl alcohol-soaked lint-free cloth between each polishing step to avoid contamination between grit sizes. All grinding and

polishing steps were conducted using a Twinprep 5 grinder/polisher (Allied High Tech Products). After all polishing steps were complete, samples were dismounted by dissolving the thermoplastic mounting wax in acetone. Dismounted samples were then ultrasonically cleaned in 150 mL of isopropyl alcohol (Fisher Scientific Company) for 10 minutes (3510 Ultrasonic Cleaner, Branson Ultrasonics) The mounting, grinding, and polishing process was then repeated for the other side of the disc. The bioactive glass sample preparation process, including all consumables and equipment used, is indicated on the sample preparation process flow diagram in Figure 3-6.

Polished discs of bioactive glass were used in conjunction with bioactive glass frit as controls for *in vitro* mineralisation studies. The polished discs allowed for macroscopic visualisation of the mineral layer in addition to SEM, while the frit provided more comparable morphology and mineralisation kinetics to the composite scaffolds. Bioactive glass discs were used to assess the viability of the simulated body fluid (SBF) used in *in vitro* immersion tests; further details are presented in Appendix III.

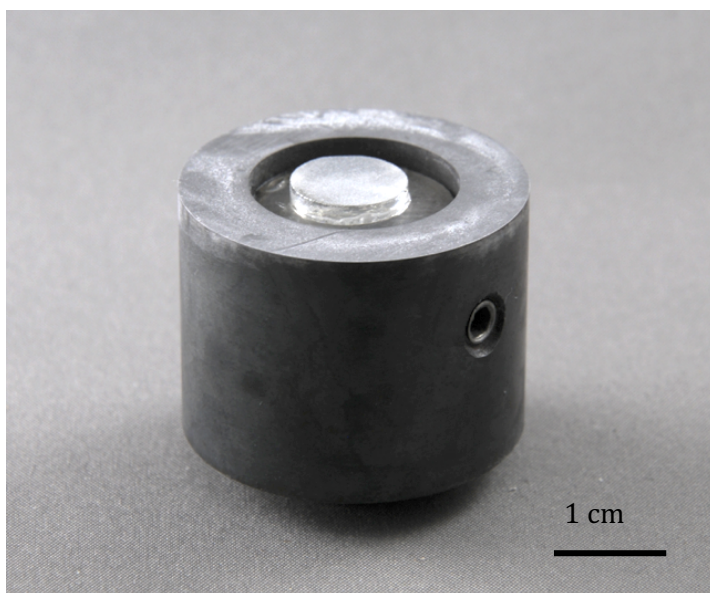


Figure 3-7. Bioactive glass disc mounted (centre) to polishing jig with Crystalbond 509 thermoplastic wax, shown here before grinding or polishing.

3.2.3 Preparation of Sodium Silicate

3.2.3.1 Preparation of Sodium Silicate Gas Pycnometry Specimens

To prepare sodium silicate specimens for gas pycnometry, droplets of aqueous sodium silicate were dispensed using a 3.2 mL polyethylene pipette (Fisher Scientific Company) onto a sheet of Parafilm M (Bemis Company Inc., Oshkosh, WI), and an analytical balance (P-214, Denver Instrument) was used to record the mass of the unset sodium silicate. Droplets were allowed to set in open air for 120 hours before removal from the Parafilm. The setting time of 120 hours was selected based on sodium silicate kinetics studies further detailed in Chapter 4.1.2; after 120 hours, all specimens had reached 95% of maximum normalised mass loss. Parafilm was chosen as its flexibility allowed the set droplets to be removed without fracture, limiting the risk of material loss.

3.2.3.2 Preparation of Sodium Silicate *in vitro* Specimens

Sodium silicate *in vitro* specimens were prepared using Parafilm M (Bemis Company Inc.) as a temporary substrate. A known mass of aqueous sodium silicate was dispensed onto the Parafilm using a 3.2 mL polyethylene pipette (Fisher Scientific Company), which then set in open air to form a rounded, oblong hemisphere (Figure 3-8). Parafilm was again chosen for its flexibility, which allowed the set specimens to be removed without fracture.



Figure 3-8. Set sodium silicate specimen prepared for *in vitro* immersion tests. The distortion of the fabric weave, visible through the specimen, indicates the uneven bottom surface and shrinkage void that formed during setting (further detailed in Chapter 4.1.2).

3.3 Characterisation

Design Criteria	Characterisation Technique	Expected Outcome
Materials Characterisation	Manual tap density	- Tap density - Packing factor
	Imaging particle size analysis	- Particle size distribution - Particle morphology
	Sodium silicate reaction kinetics	- Rate of binder phase setting reaction - Mass loss of set binder phase
Formability	Mould resolution	- Minimum vol% binder
	Compressibility	- Maximum vol% binder
Geometric Stability	De-moulded scaffold resolution	- Minimum vol% binder
Porosity	Optical light microscopy with epoxy infiltration	- 2-D pore size - 2-D binder layer thickness - 2-D pore distribution/dispersion
	Scanning electron microscopy	- Composite morphology - Phase distribution
	Gas pycnometry	- Open/closed porosity
	Micro-computed tomography	- Open/closed porosity - 3-D pore distribution/dispersion - Surface area-to-volume ratio
Load-bearing Capacity	Unconfined compression testing	- Uniaxial compression strength - Compressive failure mode
Bioactivity	<i>in vitro</i> immersion testing	- <i>in vitro</i> mineralisation
	Scanning electron microscopy with energy-dispersive X-ray spectroscopy	- <i>in vitro</i> morphological changes - <i>in vitro</i> chemical changes - Mineral feature size, distribution/dispersion
	X-ray diffraction	- Structure changes induced by <i>in vitro</i> chemical changes
	Fourier-transform infrared spectroscopy	- <i>in vitro</i> chemical changes
Resorbability	<i>in vitro</i> immersion testing	- <i>in vitro</i> gel formation

Table 3-4. Design criteria, characterisation techniques, and expected outcomes used to evaluate this research.

3.3.1 Imaging Particle Size Analysis

Imaging particle size analysis (PSA) was conducted to determine the shape and size distribution of the bioactive glass frit. Particle shape was quantified using circularity and convexity measurements. This data was then used to quantify the morphological characteristics of the frit that influence its performance in the composite scaffold. The shape, size, and structure of the bioactive glass influences its packing and wetting with waterglass, which in turn influences the composite's formability, porosity, and load-bearing capacity. The particle size information was also compared against the manufacturer's specifications to assess the presence and value of any deviation.

Optical imaging particle size analysis determines particle size distribution by dispersing a sample onto a glass plate, and then scanning the area of the plate with an optical light microscope to capture 2-dimensional projections of each particle. These images are then analysed for various parameters, including diameter, aspect ratio, circularity, and convexity.

Circularity (C , dimensionless) is defined as the ratio of the area of a particle ($A_{particle}$) to the area of a circle with the same convex hull perimeter (P_C), effectively measuring the degree to which a particle is similar to a circle [4, 5]. The convex hull perimeter is the perimeter of the smallest convex hull that encloses the entire particle (depicted schematically in Figure 3-9). The less smooth and round a particle is—i.e., the more it differs from a circle—the lower the circularity value will be. Circularity is calculated according to Equation 3.1.

$$C = \frac{4\pi A_{particle}}{(P_C)^2} \quad (3.1)$$

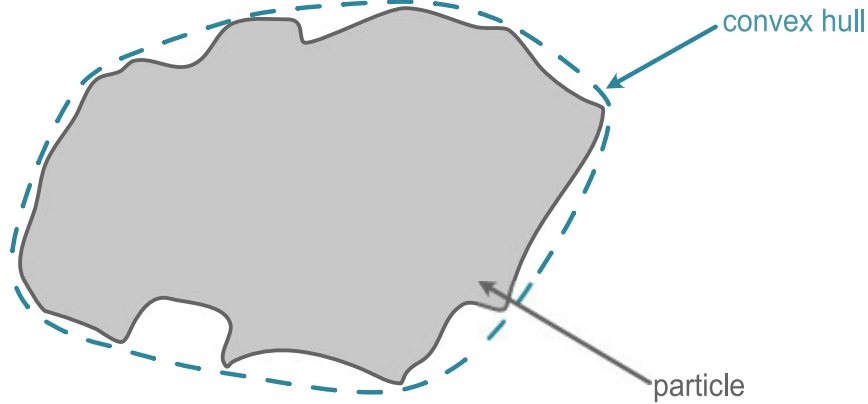


Figure 3-9. Schematic depiction of the minimum convex hull of a particle.

Convexity (C_x , dimensionless) is defined as the ratio of the convex hull perimeter (P_c) to the actual particle perimeter ($P_{particle}$), effectively measuring the particle edge roughness [4, 5]. Increasing roughness corresponds to a decreasing convexity value. Convexity is calculated according to Equation 3.2.

$$C_x = \frac{P_c}{P} \quad (3.2)$$

Static optical imaging was used to acquire data for PSA. This method involves dispersing a sample onto a glass plate and capturing an optical image of each particle. Each image is then analysed to assess the shape and size distribution of the sample. A Malvern Morphologi G3SE system (Malvern Panalytical, Malvern, UK; used with Nikon TU Plan Fluor 5x objective lens) with a sample volume of 0.5 cm³ was used for these measurements. To account for artefacts from contamination or scratches, a background scan of the bare glass plate was captured and subtracted from the bioactive glass data. Removal of background particles was confirmed by examining the 2-dimensional projections of each removed particle to confirm that they were not bioactive glass frit.

3.3.1.1 Sampling Method

The bioactive glass frit is a free-flowing powder, but the samples used in particle size analysis were not collected according to the “Golden Rules” outlined in ASTM E2651-19 (Standard Guide for Powder Particle Size Analysis) [6]. This standard stipulates that a powder should be sampled in motion, in small increments from a flowing stream, and not directly from a container. Spin riffling is recommended as the ideal sampling method for free-flowing powders.

It was assumed that the bioactive glass frit was too brittle and friable to be sampled in motion, and that the damage incurred by the motion of the powder would change the shape and size distribution of the sample. Additionally, the bioactive glass frit is affected by static electricity, which may affect the shape and size distribution if the powder is sampled in motion or through sieves.

Scoop sampling was used to obtain PSA samples; material was removed from the top of the bulk, which was stored in a 1 L cylindrical polystyrene container. This method of sample acquisition is consistent with the method used to obtain bioactive glass feedstock material for all other samples discussed in this research. Over the duration of this project, less than 20% of the bulk material was consumed, and the container of bulk frit was not mixed, inverted, shaken, or otherwise intentionally disturbed. The frit samples analysed in PSA are not intended to be representative of the bulk bioactive glass, but instead representative of the material utilised in the specimens involved in this research.

An investigation of powder sampling method reliability found that particle size distributions obtained via scoop sampling had a standard deviation of 5.14%, while samples obtained via spin riffling had a standard deviation of 0.125% [7].

3.3.2 Sodium Silicate Reaction Kinetics

The reaction rate of aqueous sodium silicate in ambient conditions was investigated to determine appropriate setting times for composite scaffold and sodium silicate control

specimens. Aqueous sodium silicate was dispensed onto Parafilm M with a polyethylene pipette (Fisher Scientific Company), and its mass was recorded every 10 seconds with an analytical balance (P-214, Denver Instrument) until the mass loss was < 0.5% over a period of 24 hours. Recorded data was then fit to a modified Michalis-Menton reaction equation, a kinetic equation that typically describes the rate of reaction as a function of decreasing reactants (Equation 3.3) [8]. The modified equation describes the normalised mass loss (m_t/m_i , in percent) as a function of time (t , in hours). The parameters A and B describe the 100% and 50% reaction completion time points, respectively. Two geometries (droplets and bulk discs; Table 3-5) of sodium silicate were tested to determine the effect of geometry on the rate of reaction.

$$\frac{m_t}{m_i} = \frac{(A \cdot t)}{(B + t)} \quad (3.3)$$

	Radius (mm)	Height (mm)
Droplets	4.2	2.2
Bulk discs	13	3.5

Table 3-5. Geometry of specimens used to investigate sodium silicate reaction kinetics.

3.3.3 Formability and Geometric Stability Evaluation

As aforementioned, preliminary screening tests established the composition range of sodium silicate capable of being formed into unique geometries and undercuts as an unset paste, while maintaining structural integrity as a de-moulded scaffold. The ability of the unset paste to be formed into various geometries and aspect ratios was evaluated using a custom Reprorubber putty (Flexbar Machine Company, Islandia, NY) negative mould made from a custom 3D-printed positive mould (Figure 3-10). The design criteria of formability established both upper and lower bounds of possible composite compositions; excess binder

resulted in a paste that was too flowable to be formed into undercuts or an unfeasible setting time, while insufficient binder resulted in a non-cohesive paste or an unfeasible manipulation time.

The paste remained formable in air up to its *manipulation time*—herein defined as the maximum amount of time the paste could be continuously worked before ‘calving’ agglomerates (partially set and unformable) and losing cohesiveness. Continuous working of the paste was necessary to replenish the surface exposed to atmosphere with unreacted binder phase—the external surface set at a faster rate than the interior bulk, which was affected by the diffusion gradient of CO₂ gas into the composite. In contrast to traditional working time, manipulation time does not imply a bulk reduction of viscosity or plastic flow, but rather a loss of cohesiveness that could impart a loss of formability in the paste, a lack of geometric stability once set, and heterogeneous phase and property distribution.

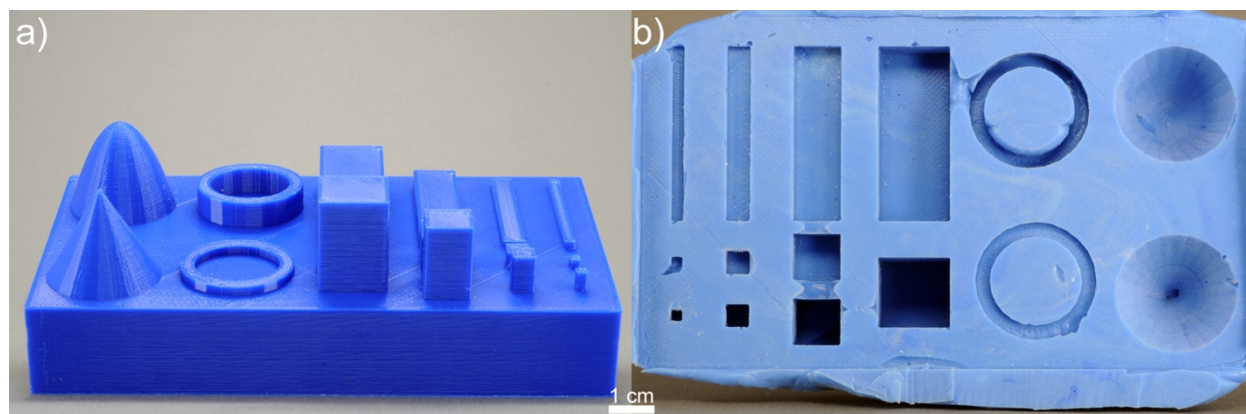


Figure 3-10. (a) Oblique view of 3D-printed original positive mould and (b) plan view of custom Reprorubber negative mould from which positive composite scaffolds were fabricated to assess formability and geometric stability (cone and paraboloid only in this study) [2].

Geometric stability of the composite was evaluated using de-moulded specimens from the negative mould above (Figure 3-10), demonstrating the degree to which the set scaffolds maintained their geometry. The lower bound of binder phase composition was additionally established by the geometric stability design criteria; insufficient binder

resulted in a composite incapable of maintaining its shape after setting. Geometric stability information was gathered using macrographs, further detailed in Chapter 3.3.4.1.

3.3.4 Imaging

3.3.4.1 Macrographs

Macrographs of the materials used in this research (Chapter 3.1) were obtained before, during, and after processing and characterisation using a digital camera (Finepix HS10, equipped with a Fujinon 30x optical zoom lens; Fujifilm Canada, Mississauga, ON) and a digital single lens reflex camera (D300s, equipped with an AF-S DX Nikkor 18-105mm f/3.5-5.6G ED VR zoom lens, Nikon Corp., Tokyo, Japan). Additional stereomicrographs of bioactive glass control specimens and composite scaffolds after *in vitro* immersion studies were obtained using a Leica EZ4 HD stereomicroscope (Leica Microsystems Inc., Concord, ON).

3.3.4.2 Optical Light Microscopy

Optical light microscopy (OLM) was used to obtain micrographs of polished epoxy-infiltrated composite specimens. Micrographs were used to visualise phase distribution and quantify two-dimensional pore and interconnect size. Examining the polished bottom surface of the specimen after epoxy infiltration allowed for a preliminary indication of pore interconnectivity; an open porous network would result in complete epoxy infiltration through the bulk of the specimen, leaving no visible voids. Three-dimensional open porosity was later quantified and verified with gas pycnometry and micro-CT (Chapters 4.4.3, 4.4.4). Two-dimensional phase distribution from OLM micrographs was verified in three dimensions with micro-CT renderings of the composite specimens.

Micrographs were obtained with a Zeiss Axio Imager M.2m (Carl Zeiss Canada Ltd., North York, ON) equipped with Zeiss EC-Epiplan Neofluar objective lenses in bright field (BF) mode. AxioVision SE64 v4.9.1 was used to process OLM micrographs and measure specimen features. Two-dimensional pore size was calculated as the average chord length passing through the centre of a pore. Two perpendicular chord lengths over twenty-two (22) unique pores were measured for each specimen. Two-dimensional binder layer thickness was measured as the average over twenty-two (22) unique binder layer locations per specimen.

3.3.4.3 Scanning Electron Microscopy

Scanning electron microscopy (SEM) was used to image surface features of bioactive glass frit, solid sodium silicate, as-moulded composites, mineralised *in vitro* specimens, and fracture surfaces of the composite specimens. As-processed morphology of composite specimens was used to visualise bioactive glass frit packing, composite constituent interaction, porosity, and phase distribution. Surface morphology changes after *in vitro* immersion were used to assess mineralisation, which in turn was used to predict bioactivity. Composite specimen fracture surfaces were used to assess failure mode during mechanical strength testing. SEM was selected as an imaging technique as it is non-destructive with a large depth of field, which is necessary for examining the irregular topography of the composite specimens.

SEM images are generated with a beam of electrons, which is scanned over the surface of a specimen, producing both backscattered electrons (BSE; through elastic scattering) and secondary electrons (SE; through inelastic scattering). Characteristic X-rays are also generated by the incident electron beam, which can be used for chemical analysis (further detailed in Chapter 3.3.8). The scattered electrons are then collected by a detector, which processes the electron signal intensity to generate an image [9].

Specimens were sputtered with gold using a Denton Desk II (Denton Vacuum, LLC., Moorestown, NJ) for 90 seconds (12 nm coating) prior to imaging to reduce charging.

Imaging was conducted in SE and BSE mode with a Zeiss EVO MA10 SEM and LaB₆ filament. Zeiss SmartSEM v05.06 was used to process SEM micrographs. Surface mineral feature size was measured using ImageJ v1.52q. At least fifty-six (56) unique measurements were averaged per mineral surface feature.

3.3.4.4 Micro-Computed Tomography

Micro-computed tomography (micro-CT) was used to calculate the porosity and surface area-to-volume ratio of the composite scaffolds, as well as develop a 3D visualisation of the composite structure and phase distribution. Data from micro-CT was then used to evaluate the effect of composition on the structure and porosity of the scaffolds. Additionally, 3D digital reconstructions were used to verify the aforementioned preliminary screening trials (Chapter 3.3.3) by visualising phase maldistribution of excess binder phase compositions.

Micro-CT was chosen as it is a non-destructive imaging technique capable of producing 3D models of porous structures with a spatial resolution of 8.90 μm . Results from micro-CT can be used to calculate pore size of a 3D scaffold with greater accuracy than a simple 2D image from microscopy. Additionally, the total porosity of the composites calculated by micro-CT can be verified against the total porosity calculated with gas pycnometry.

The principle of micro-CT operation involves the use of an X-ray source and detectors that are rotated around a specimen; the signal received by the detectors is used to generate a 2-dimensional image based on the relative radiodensity of the specimen. These 2D images are captured through the bulk of the specimen in a series trans-axial projections (slices), that when combined generate a 3D rendering comprised of voxels, rather than pixels. The 'slice' thickness determines the size of these voxels, which then dictates the resolution of the 3D rendering [10]. The digital 3D reconstruction can then be used for visualisation or quantitative analysis, including surface area-to-volume ratio and porosity.

Bruker SkyScan 1176 and 1076 micro-CT instruments (Bruker Ltd., Milton, ON) with a 90 kV X-ray source were used to collect micro-CT data. Bruker CTAn v1.10.1 software was used to analyse porosity via thresholding and binarisation of the reconstructed images and generate 3D digital models of the specimens, which were then processed and manipulated with Bruker CTVol v2.2 software. Bruker CTVOx v3.0 software was used to create and manipulate alternative 3D digital renderings of the composite scaffolds.

3.3.5 Gas Pycnometry

Gas pycnometry was used to determine the volume and density of the composite material, bioactive glass frit, and solid sodium silicate. These measurements were used to calculate the porosity and constituent volume fractions of the composite material after setting, and to quantify the changes in volume and density that occur during setting of aqueous sodium silicate.

Gas pycnometry was chosen as it is a non-destructive, non-reactive measurement technique capable of measuring the density of microporous materials. Volume measurements are determined using the ideal gas law (Equation 3.4) and the principle of gas displacement. A known volume of inert gas fills a chamber ($V, P_{reference\ chamber}$) containing a specimen of known mass ($m_{specimen}$), and the volume of displaced gas is used to calculate the volume of the specimen (Equation 3.4); shown schematically in Figure 3-11. The specimen volume is then used to calculate the specimen density ($\rho_{specimen}$), as per Equation 3.6.

$$PV = nRT \quad (3.4)$$

$$V_{specimen} = V_{specimen\ chamber} + \frac{V_{reference\ chamber}}{1 - \frac{P_{specimen\ chamber}}{P_{specimen+reference\ chamber}}} \quad (3.5)$$

$$\rho_{specimen} = \frac{m_{specimen}}{V_{specimen}} \quad (3.6)$$

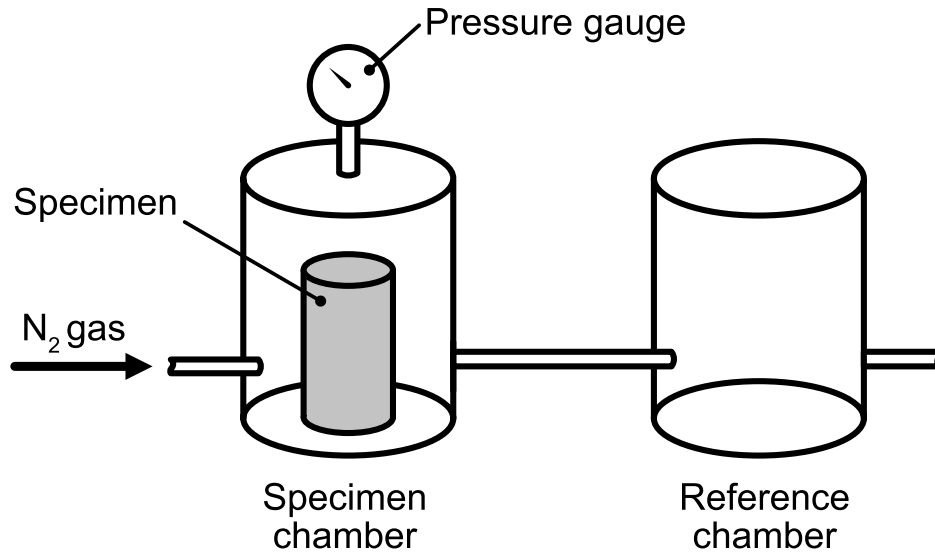


Figure 3-11. Schematic depiction of a gas pycnometer, showing both the specimen and reference chambers, which utilise the principle of gas displacement and the pressure difference between the chambers to calculate the specimen volume and density.

An AccuPyc II 1340 Series pycnometer (Micromeritics, Norcross, GA, USA) was used with nitrogen gas (99.998% pure; Praxair Canada Inc., Edmonton, AB) for all pycnometry measurements, using a sample chamber with a volume of 15.449 cm³, reference chamber volume of 74.455 cm³, and an equilibration rate of 0.055 kPa/min. Each sample was measured in 10 iterative cycles and the chambers were purged with nitrogen gas between each cycle. Three (3) specimens of each composition were analysed.

The use of gas pycnometry to analyse the open porosity faces the limitations detailed in the assumptions listed in Chapter 3.3.5.1. To mitigate the effect of these limitations, gas pycnometry was used in conjunction with micro-CT to quantify porosity of the composite specimens. As micro-CT is an imaging technique, the limitations faced by each technique are different—micro-CT, in addition to measuring the pore volume, was used to reveal the distribution of porosity through the specimens, the interconnectivity of pores, the surface area-to-volume ratio, and composite phase distributions.

3.3.5.1 Gas Pycnometry Data Analysis

Gas pycnometry data was used to assess the amount of open porosity present in composite scaffold specimens. The measured volume of each specimen was compared against the ‘minimum calculated volume’, which is the volume occupied by only bioactive glass frit and solid sodium silicate.

Assuming that the minimum volume that a composite scaffold could occupy would equal the combined volume of the 45S5 frit (V_{BAG}) and solid sodium silicate ($V_{WG,s}$), it then follows that the pycnometry volume measurement of a porous specimen with only open porosity would equal this ‘minimum volume’ value (V_{min}). If the measured volume of a specimen is greater than this minimum volume, it is assumed that the additional volume is exclusively comprised of closed pores.

The minimum volume values were calculated as follows:

$$V_{min} = V_{BAG} + V_{WG,s} \quad (3.7)$$

$$V_{BAG} = \frac{(m_{tested\ specimen}) \cdot (wt\% \text{ BAG}_{set})}{\rho_{BAG}} \quad (3.8)$$

$$V_{WG,s} = \frac{(m_{tested\ specimen}) \cdot (wt\% \text{ WG}_{set})}{\rho_{WG,s}} \quad (3.9)$$

$$wt\% \text{ BAG}_{set} = 1 - wt\% \text{ WG}_{set} \quad (3.10)$$

$$wt\% \text{ WG}_{cured} = \frac{m_{WG,s}}{m_{WG,s} + m_{BAG}} \quad (3.11)$$

$$m_{WG,s} = (m_{WG,l}) \cdot (mass\ loss\ factor) \quad (3.12)$$

$$mass\ loss\ factor = \left(1 - \frac{m_{WG,l} - m_{WG,s}}{m_{WG,l}} \right) \quad (3.13)$$

Bioactive glass density (ρ_{BAG}), set sodium silicate density ($\rho_{WG,s}$), and the mass loss factor were determined empirically via gas pycnometry.

The specimen mass ($m_{tested\ specimen}$) used in this calculation was the mass measured at the time of pycnometry analysis, as opposed to the combined weight of the measured feedstock materials. This convention accounted for the effect of the material loss—during the manufacturing process, residual paste adheres to the weigh boat, the bulb of the pipette used for mixing, and to gloves used to handle the specimen. Additionally, the friable nature of the set specimen can lead to loss of solid material during handling after setting.

Assumptions:

1) The material lost during manufacturing and handling was assumed to be lost proportionally; i.e., any lost material has the same composition as the bulk of the specimen. Realistically, the unset waterglass wets to the weigh boat, and it is likely that this wetting leads to a disproportionate loss of waterglass. It follows that compositions with lower amounts of waterglass may be more affected by this disproportionate loss.

2) At the time of analysis, the sodium silicate was assumed to be fully set, and assumed to not densify or shrink further. The time elapsed between manufacturing and analysis varied between specimen groups, and may have had an effect on the degree to which sodium silicate densified. To mitigate this variability, preliminary kinetics studies examining the rate of mass loss during setting of sodium silicate (Chapter 4.1.2) were used to confirm the stability of the specimens prior to gas pycnometry analysis. As shown in Figure 3-12, sodium silicate in air reaches half of its maximum normalized mass loss (i.e., setting reaction of binder is 50% complete) within 13.76 hours (parameter B in the curve fit). All pycnometry samples were allowed to set for a minimum of 288 hours before testing; as indicated on Figure 3-12 by the vertical dashed line, this setting time allowed the binder phase to reach the stable asymptotic region of the kinetic curve (95% level of maximum normalized mass loss).

3) The measured densities of solid sodium silicate and 45S5 bioactive glass are assumed to be representative of the densities of these constituents in the composite specimens. In actuality, the geometry of the setting waterglass was different (i.e., droplets on parafilm vs. contained within a composite scaffold), which may have affected the measured density. Additionally, the total set time for the sodium silicate specimen was different than the total set time for each composite specimen.

4) It is assumed that no reaction occurs between the two constituents that would alter the density of either constituent.

5) The sodium silicate-only specimen that was analysed was assumed to have no closed pores; closed pores would alter the empirically determined ρ_{WG_s} value.

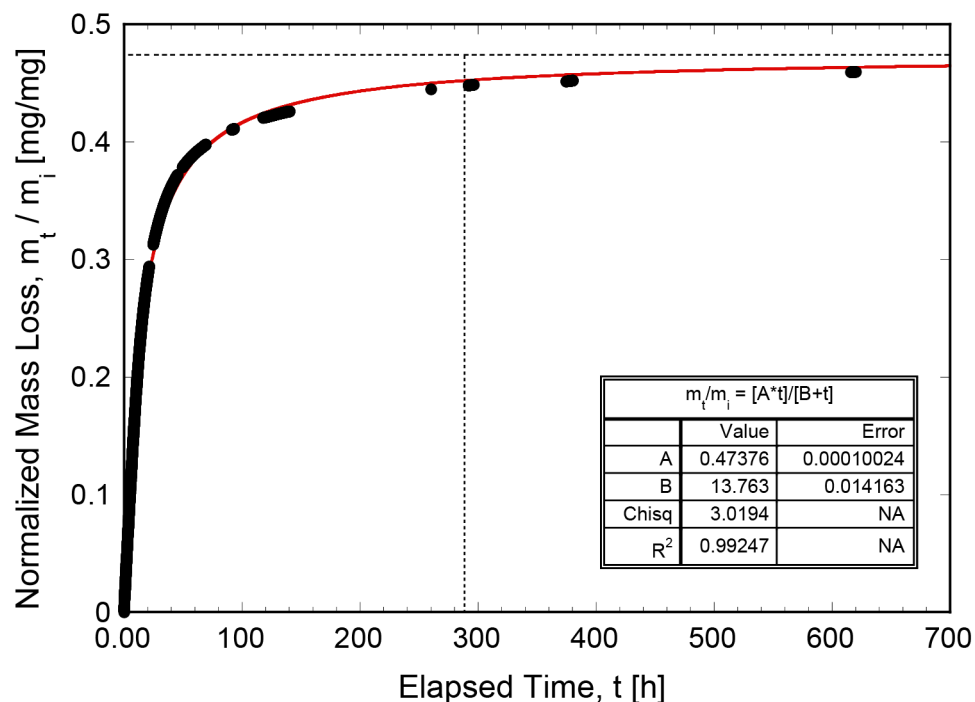


Figure 3-12. Kinetics data and curve fit for the mass loss during setting of bulk aqueous sodium silicate in air at 294 K (21 °C). The curve fit (red line) is based on the Michaelis-Menten equation describing a reaction as a function of concentration of reactants which decreases in time (as the reactants are consumed—much like is occurring in the setting of sodium silicate). The horizontal dashed line represents the asymptotic value of the mass loss (parameter A) and the vertical dashed line represents the setting time used for pycnometry specimens in air. Parameter B in the curve fit represents the time to reach half the maximal mass loss. Bulk solution kinetics were used as a conservative control due to the longer CO₂ diffusion path length as compared to the diffusion path length of the liquid spread between frit particles in the composite. Further details of sodium silicate kinetics studies can be found in Chapter 4.1.2 [2].

3.3.6 Mechanical Strength Testing

The mechanical behaviour of the composite material under uniaxial compression was assessed using an unconfined compressive strength (UCS) test. The UCS of the composite was used to assess its load-bearing capabilities, as well as to determine the effect of composition on the mechanical properties and failure mode of the material.

Load-displacement curves were collected and then transformed into engineering stress-strain curves using the original cross-sectional area (A_o in mm^2) of the composite cylinders. The unconfined compressive strength, UCS (σ_{UCS}), in MPa, was taken at the maximum load (P_{max} in N) for each specimen:

$$\sigma_{UCS} = \frac{P_{max}}{A_o} \quad (3.14)$$

Since the compressive strength acts only along one axis, the UCS can also be interpreted at the uniaxial compressive strength.

Stress (σ)-strain (ε) plots were generated using Equations 3.15 and 3.16, where d is the distance travelled by the platen, h_o is the initial specimen height, and P is the load applied to the specimen:

$$\varepsilon = \frac{d}{h_o} \quad (3.15)$$

$$\sigma = \frac{P}{A_o} \quad (3.16)$$

Testing involved placing a specimen on a stationary platen, while a second platen moves downward onto the sample at a constant speed (1.33 mm/min), uniaxially compressing the specimen until failure. A load cell under the stationary platen measured the force (P) applied to the sample throughout the test. Uniaxial compressive force was applied

to the sample until the force measured was 0 N. This process is illustrated schematically in Figure 3-13.

In accordance with ASTM D7012 [11], the specimens were in the form of right cylinders with an aspect ratio (h/d) of 2.45; 12 mm in diameter, 27 mm in height. Testing was completed with a PASCO Comprehensive Materials Testing System ME-8244; constant strain rate of $0.77 \times 10^{-3} \text{ s}^{-1}$ was achieved through modification with a stepper motor and controller (SureStep 1288 oz-in) and a pair of 2.54 cm-diameter compression platens (PASCO Compression Accessory ME-8247). PASCO Capstone v1.13.4 software was used to collect data during mechanical strength testing. A minimum of twelve (12) specimens of each composition were tested).

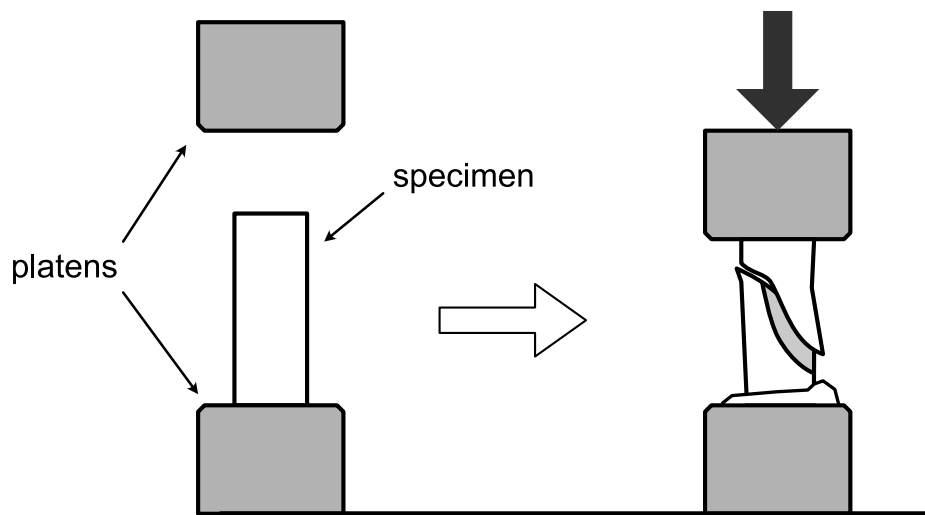


Figure 3-13. Schematic of unconfined mechanical crush testing in accordance with ASTM D7012 wherein a right cylindrical specimen is placed between two platens. The upper platen is then moved downward at a constant speed and strain rate, crushing the specimen. The test is completed when the sample has failed and the force measured is 0 N.

3.3.7 *in vitro* Immersion Tests

Bioactivity and mineralisation were assessed by *in vitro* immersion in simulated body fluid (SBF), prepared in accordance with method developed by Kokubo and Takadama [12]; the constituents of each 1000 mL batch are listed in Table 3-6, resulting in the final ion concentrations listed in Table 3-7. Temperature and pH of the SBF were monitored during preparation using a digital thermocouple (Fluke 54 II B, Fluke Corporation, Everett, WA) and digital pH meter with temperature probe (Accumet Basic AB15 Plus, Fisher Scientific Company, Toronto, ON). Sodium silicate control specimens, bioactive glass control specimens (frit and polished discs), and composite scaffolds were flushed with deionised ultra-filtered water (DIUF) (Fisher Scientific Company; CAS: 7732-18-5) immediately before placing in a polystyrene Petri dish (Fisherbrand Extra-Deep Disposable Petri Dishes, Fisher Scientific Company, Toronto, ON) filled with SBF. The specimen surface area to SBF volume ratio was 0.1 cm^{-1} , as established by Kokubo and Takadama [12]. The surface area of frit and composite samples was estimated according to the method detailed in Appendix IV. The Petri dishes were sealed with Parafilm M (Bemis Company Inc., Oshkosh, WI) and held at $36.5 \pm 1.0^\circ\text{C}$ in a water bath (Isotemp 210, Fisher Scientific Company, Toronto, ON) for the length of the *in vitro* test (1, 3, or 14 days). A unique specimen was used for each time point. As best practice suggests, SBF was replaced every 3 days to maintain an appropriate supply of ions. pH of spent SBF was tested using pH testing strips (Whatman pH Indicator Paper, Whatman International Ltd., Maidstone, UK). Upon completion, specimens were removed from the SBF solution and flushed with DIUF, followed by isopropyl alcohol, before drying in air overnight. Dried specimens were stored in a desiccator cabinet until being characterised.

Specimens were analysed to assess the formation of Ca-P rich minerals (e.g., apatite species) as an indicator of *in vitro* bioactivity. The presence of mineral species was analysed using SEM, EDX, XRD, and FTIR. Composite specimens were manually split before characterisation, with an intact half proceeding to SEM/EDX, one quarter of the material proceeding to XRD, and one quarter of the material proceeding to FTIR.

Reagent	Amount	Purity	Manufacturer	CAS
NaCl	8.035 g	≥ 99.0% (ACS)	EMD Chemicals Inc., Gibbstown, NJ	7647-14-5
NaHCO ₃	0.355 g	≥ 99.7% (ACS)	Fisher Scientific Company, Toronto, ON	144-55-8
KCl	0.225 g	≥ 99% (ACS)	MP Biomedicals, LLC, Solon, OH	7447-40-7
K ₂ HPO ₄ · 3H ₂ O	0.231 g	≥ 99%	Acros Organics, Morris Plains, NJ	16788-57-1
MgCl ₂ · 6H ₂ O	0.311 g	≥ 99% (ACS)	MP Biomedicals, LLC, Solon, OH	7791-18-6
1.0M-HCl (from 12M-HCl)	39 mL	ACS-Pur	Fisher Scientific Company, Toronto, ON	7647-01-0
CaCl ₂	0.292 g	≥ 96% (ACS)	MP Biomedicals, LLC, Solon, OH	10043-52-4
Na ₂ SO ₄	0.072 g	≥ 99.0% (ACS)	Ricca Chemical Company, Arlington, TX	7757-82-6
Tris-(hydroxymethyl)aminomethane	6.118 g	≥ 99.8% (ACS)	Fisher Scientific Company, Toronto, ON	77-86-1
1.0M-HCl (from 12M-HCl)	0-5 mL	ACS-Pur	Fisher Scientific Company, Toronto, ON	7647-01-0

Table 3-6. Reagents required for preparing 1000 mL of SBF [12], presented in the order of addition.

Ion	Concentration (mM)
Na ⁺	142.0
K ⁺	5.0
Mg ²⁺	1.5
Ca ²⁺	2.5
Cl ⁻	147.8
HCO ₃ ⁻	4.2
HPO ₄ ²⁻	1.0
SO ₄ ²⁻	0.5
pH	7.40

Table 3-7. Expected ion concentrations and pH of SBF prepared in accordance with the method developed by Kokubo and Takadama [12].

3.3.8 Energy-dispersive X-ray Spectroscopy

Energy-dispersive X-ray spectroscopy (EDX) was used to semi-quantitatively evaluate the surface chemistry of *in vitro* specimens. Surface morphology, chemical composition, and mineralisation were characterised with EDX in conjunction with variable pressure scanning electron microscopy (VP-SEM) in secondary electron (SE) mode. EDX analysis was used to identify elements present in the surface layer of *in vitro* specimens and compare element concentration and distribution as a function of composition and immersion time.

EDX analysis is capable of identifying surface chemistry by using characteristic X-rays generated by the interaction between a material and an incident electron beam. When bombarded by the electron beam, orbital electrons in the material can be ejected, ionising the atom. Electrons from higher energy states will then replace the ejected electron, generating an X-ray photon with an energy that corresponds to the energy difference

between the two electrons. Elements can be identified by measuring the characteristic energy of the emitted X-ray [13].

EDX is typically considered a semi-quantitative chemical analysis technique due to its large interaction volume (1-5 μm depth [14]), low spatial resolution, and the influence of specimen topography on X-ray detection. As such, EDX results were primarily used for element identification and prediction of mineralisation in this research, rather than quantification. Mineral species and comparative quantification were further assessed with XRD and FTIR analysis.

EDX was conducted with a Zeiss Sigma 300 VP SEM with Bruker XFlash 6160 EDX detectors. Specimens were sputtered with gold using a Denton Desk II for 90 seconds (12 nm coating) prior to imaging to reduce charging.

3.3.9 X-ray Diffractometry

Powder X-ray diffractometry (XRD) was conducted for phase identification prior to and following *in vitro* immersion. Bioactive glass control specimens, sodium silicate control specimens, and composite scaffold *in vitro* specimens were analysed with XRD. The presence of apatite and the extent of mineralisation was used to assess the bioactivity of the control specimens and composite material, and to determine the effect of composition on its behaviour *in vitro* [12, 15]. XRD data was used to verify results from SEM/EDX and FTIR, as well as to detect structural changes brought about by chemical changes that may not have been visible with other characterisation techniques.

XRD analysis utilises the diffraction of X-rays by crystallographic lattices, which produce constructive interference when exposed to incident monochromatic X-rays. Constructive interference occurs when the interaction satisfies Bragg's Law, and thus is characteristic of the lattice spacing (d) and diffraction angle (θ) [16]. Bragg's Law is shown in Equation 3.17, below, where n is the order of reflection (number of planes) and λ is the wavelength of the X-rays.

$$n\lambda = 2d \sin(\theta) \quad (3.17)$$

The diffracted X-rays are then collected at various angles and processed into patterns that are specific to the structure of the analysed specimen. The patterns are then compared against a library of known materials to identify phases present in the material.

A Rigaku Ultima IV X-ray diffractometer (Rigaku Americas Corporation, The Woodlands, TX) was used with a powder diffraction stage in the collection of XRD data. JADE v9.5 software was used to generate XRD patterns and index peaks. Specimens were crushed to a homogenous powder with an agate mortar and pestle prior to analysis to minimise orientation effects.

3.3.10 Fourier Transform Infrared Spectroscopy

To study the surface reactions and chemical changes that occur *in vitro*, Fourier transform infrared spectroscopy was used to identify mineralisation and chemical changes of bioactive glass, sodium silicate, and composite scaffold specimens. The chemical changes that occurred *in vitro* were used to predict the bioactivity of the composite material, and to determine the effect of composition on its *in vitro* behaviour. FTIR analysis was also used to compare the sodium silicate used in this research to as-received sodium silicate, which is further detailed in Appendix I.

FTIR was selected as it has been shown to effectively detect mineralisation behaviour of 45S5 bioactive glass immersed in simulated body fluid (SBF) [17, 15], and for its ability to detect changes to amorphous phases that are not visible in X-ray diffraction.

FTIR analysis produces an infrared spectrum that is measured when infrared radiation (IR) is applied to a specimen. Chemical bonds absorb, transmit, and reflect this IR at characteristic wavelengths, and this signal is transformed to an IR spectrum using a Fourier transform. The resulting spectrum is then used to identify a material's composition and structure by comparing against known material spectra.

A Thermo Fisher Nicolet 8700 FT-IR Spectrometer (Thermo Fisher Scientific, Toronto, ON) was used in absorbance mode for the collection of all FTIR data. Specimens were crushed before analysis and used with potassium bromide (KBr) pellets as a

background for all measurements. KBr pellet measurement was chosen for its ability to measure low wavenumbers (as low as 400 cm^{-1}), which was necessary to identify mineral formation. KBr pellets were used as a background due to the fact that KBr is IR-transparent [18].

Bibliography – Chapter Three

- [1] G. M. Nelson, A. G. McDonald and J. A. Nychka, “Structure and bioactivity of Ti/bioactive glass ‘changing landscape coatings’,” *Surface Innovations*, vol. 1, no. S14, pp. 209-223, 2013.
- [2] C. M. Guzzo and J. A. Nychka, “Fabrication of a Porous and Formable Ceramic Composite Bone Tissue Scaffold at Ambient Temperature,” *Metallurgical and Materials Transactions A*, Under Review, 2020.
- [3] S. Kashyap, “Effect of crystallinity on crack propagation and mineralization of bioactive glass 45S5,” University of Alberta, Edmonton, AB, 2010.
- [4] E. Olson, “Shape Factors and Their Use in Image Analysis - Part 1: Theory,” *Journal of GXP Compliance*, vol. 15, no. 3, pp. 85-96, 2011.
- [5] S. Endoh, “Chapter 1.3: Particle Shape Characterization,” in *Powder Technology Handbook, Fourth Edition*, Boca Raton, FL, CRC Press, 2020, pp. 19-26.
- [6] ASTM International, “ASTM E2651-19: Standard Guide for Particle Size Analysis,” ASTM International, West Conshohocken, USA, 2019.
- [7] T. Allen, “Sampling of Powders,” in *Particle Size Measurement*, Berlin/Heidelberg, Springer Science+Business Media, 2012, p. 39.
- [8] J. M. Berg, J. L. Tymoczko and L. Stryer, “8.4: The Michaelis-Menten Model Accounts for the Kinetic Properties of Many Enzymes,” in *Biochemistry, 5th ed.*, New York, NY, W. H. Freeman and Company, 2002.
- [9] Y. Leng, “Scanning Electron Microscopy,” in *Materials Characterization: Introduction to Microscopic and Spectroscopic Methods*, Singapore, John Wiley & Sons (Asia) Pte Ltd, 2008, pp. 121-144.
- [10] J. D. Boerckel, D. E. Mason, A. M. McDermott and E. Alsberg, “Microcomputed tomography: approaches and applications in bioengineering,” *Stem Cell Research & Therapy*, vol. 5, no. 144, pp. 1-12, 2014.
- [11] ASTM International, “Standard Test Methods for Compressive Strength and Elastic Moduli of Intact Rock Core Specimens under Varying States of Stress and Temperatures,” ASTM International, West Conshohocken, PA, 2017.
- [12] T. Kokubo and H. Takadama, “How useful is SBF in predicting in vivo bone activity?,” *Biomaterials*, vol. 27, pp. 2907-2915, 2006.

- [13] Y. Leng, "X-Ray Spectroscopy for Elemental Analysis," in *Materials Characterization: Introduction to Microscopic and Spectroscopic Methods*, Singapore, John Wiley & Sons (Asia) Pte Ltd, 2008, pp. 171-196.
- [14] D. Brabazon and A. Raffer, "Chapter 3: Advanced Characterization Techniques for Nanostructures," in *Emerging Nanotechnologies for Manufacturing*, Oxford, UK, William Andrew Applied Science Publishers, 2009, pp. 59-91.
- [15] O. H. Andersson and K. H. Karlsson, "On the bioactivity of silicate glass," *J. Non. Cryst. Solids*, vol. 129, pp. 145-151, 1991.
- [16] Y. Leng, "X-Ray Diffraction Methods," in *Materials Characterization: Introduction to Microscopic and Spectroscopic Methods*, Singapore, John Wiley & Sons (Asia) Pte Ltd, 2008, pp. 45-77.
- [17] H. Pirayesh and J. A. Nychka, "Sol-gel synthesis of bioactive glass-ceramic 45S5 and its in vitro dissolution and mineralization behaviour," *Journal of the American Ceramic Society*, vol. 96, no. 5, pp. 1643-1650, 2013.
- [18] Y. Leng, "Vibrational Spectroscopy for Molecular Analysis," in *Materials Characterization: Introduction to Microscopic and Spectroscopic Methods Author(s): Yang Leng*, Singapore, John Wiley & Sons (Asia) Pte Ltd, 2008, pp. 253-300.

Chapter Four

Results and Discussion¹

4.1 Materials Characterisation

4.1.1 Physical Characterisation of Bioactive Glass Frit

4.1.1.1 Manual Tap Density

Manual tap density of the bioactive glass frit, measured in accordance with ISO 23145-1 [1], was found to be 1.41 g/cm³. This tap density then translates to a packing factor of 52.1% when compared against the true material density of 2.7 g/cm³. The relatively low packing factor of the frit is necessary to maintain open porosity of the composite material when combined with the binder phase.

4.1.1.2 Optical Particle Size Analysis and Scanning Electron Microscopy

The as-received bioactive glass frit particle size distribution was confirmed with optical particle size analysis, as summarised in Table 4-1. The volume distribution of particle diameters is shown in Figure 4-1.

90% of background particles were found to be smaller than 49.0 µm, and less than 10% of frit particles (including background) were found to be smaller than 205.4 µm. As such, all particles smaller than 49.0 µm were excluded from the frit particle scan data.

¹ Portions of this chapter have been submitted for publication in Metallurgical and Materials Transaction A: C. M. Guzzo and J. A. Nychka, "Fabrication of a Porous and Formable Ceramic Composite Bone Tissue Scaffold at Ambient Temperature," Under Review, submitted 12-01-2019; Journal of the Mechanical Behaviour of Biomedical Materials: C. M. Guzzo and J. A. Nychka, "In vitro response of a porous and formable ceramic composite bone tissue scaffold," Under Review, submitted 02-01-2020.

The maximum particle size measured was 833.4 μm , and the minimum particle size measured after background correction was 49.7 μm . The D50 of the volume distribution was calculated to be 394.3 μm , which is in relative agreement with the manufacturer’s report of +355 μm size. Particles below 355 μm , which constituted 40.8% of the sample, may be attributable to fractured particles in handling.

Circularity measurements revealed that most particles are irregularly shaped, with 37.5% of particles classified as ‘very angular’ ($C < 0.60$), 62.3% classified as ‘angular’ ($0.60 < C < 0.86$), and 0.2% as ‘sub-angular’ ($0.86 < C < 0.95$) [2]. Irregular particles with low circularity typically have the larger void volume and void size [3, 4, 5], essential characteristics for open, interconnected pores in the composite scaffold. The aspect ratio, with a D50 of 0.667, is consistent with the angularity expressed by circularity measurements. Convexity was relatively high (D50 = 0.913), indicating that despite the angularity of the particles, the surface roughness is low.

Scanning electron microscopy of the bioactive glass frit was conducted to further assess its morphology and surface roughness. An SEM micrograph of the as-received frit particles is shown in Figure 4-2, revealing its angular shape and rough surface topology.

	D10 (μm)	D50 (μm)	D90 (μm)	Standard deviation (μm)
Diameter	207.4	394.3	703.5	118.6
Circularity	0.457	0.638	0.763	0.124
Convexity	0.824	0.913	0.953	0.063
Aspect ratio	0.434	0.667	0.864	0.163

Table 4-1. Background-corrected diameter, circularity, and convexity values for bioactive glass frit.

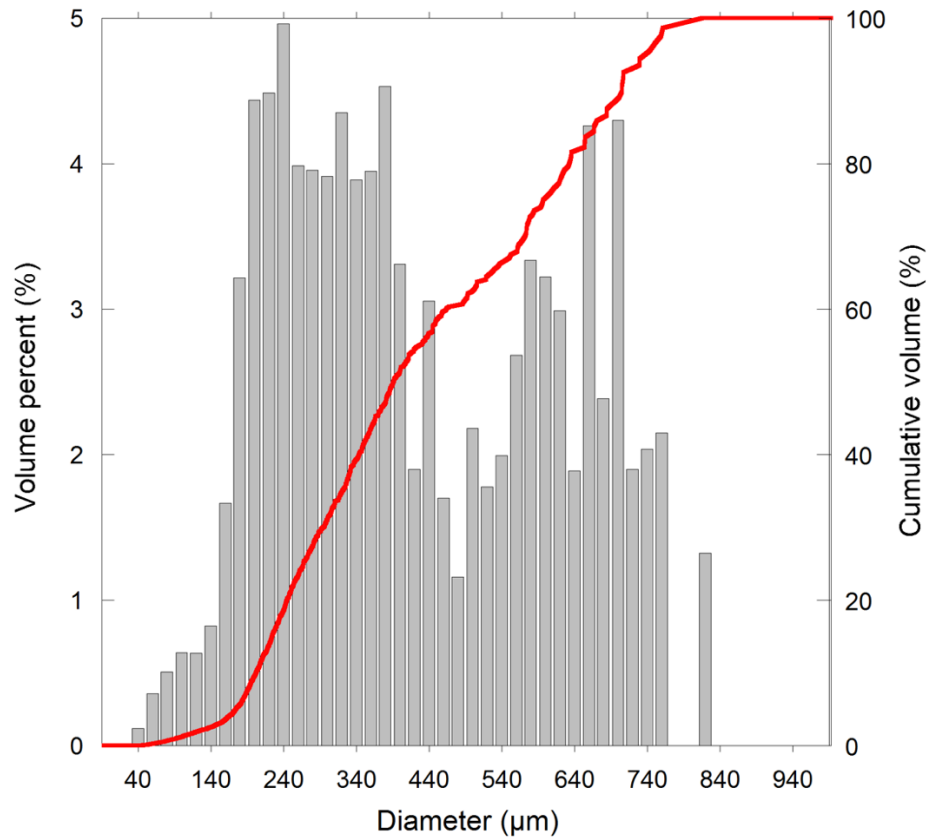


Figure 4-1. Volume-weighted size distribution of bioactive glass frit (in grey, left y-axis) overlaid with the undersize distribution (in red, right y-axis).

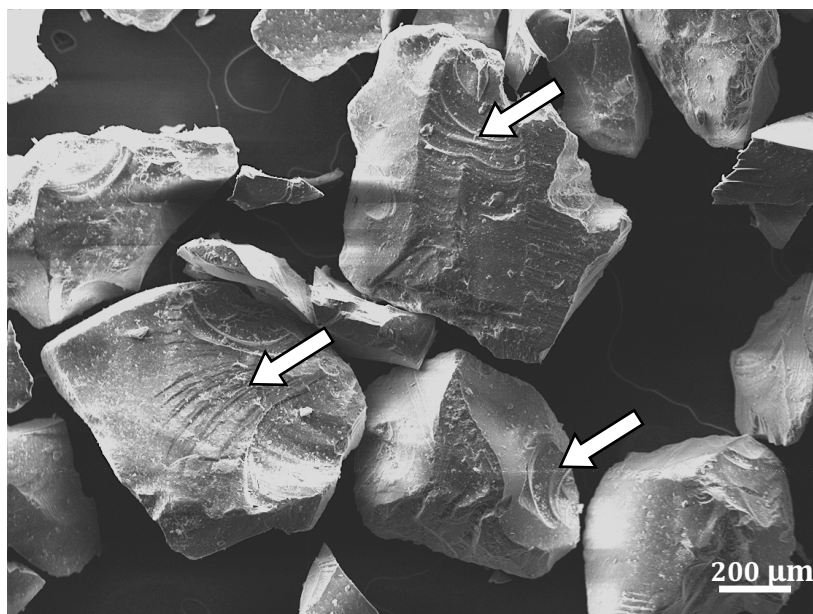


Figure 4-2. SE SEM micrograph of as-received bioactive glass frit, showing angular morphology and rough, stepped surface features indicative of cleavage fracture (white arrows).

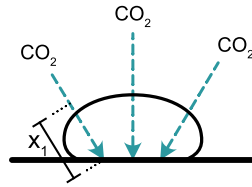
4.1.2 Sodium Silicate Setting Reaction Kinetics

Sodium silicate kinetics specimens were observed to reach a maximum mass loss of approximately 46% when setting in ambient conditions, regardless of tested geometry (Table 4-2). Geometry was found to have a profound impact on the rate of reaction, affecting the 50% setting completion time by a factor of ten, with droplets setting much more rapidly than the bulk disc. This finding is likely due to the difference in CO₂ diffusion path length; as shown schematically in Table 4-2, atmospheric CO₂ must travel a longer distance to fully set the bulk disc. Additionally, as the surface of the sodium silicate sets, it becomes a rigid diffusion barrier that increases in thickness throughout the setting reaction [6]. As the bulk disc has a larger maximum path length, it correspondingly has a larger diffusion barrier formed by the set material, and thus would require more time to set.

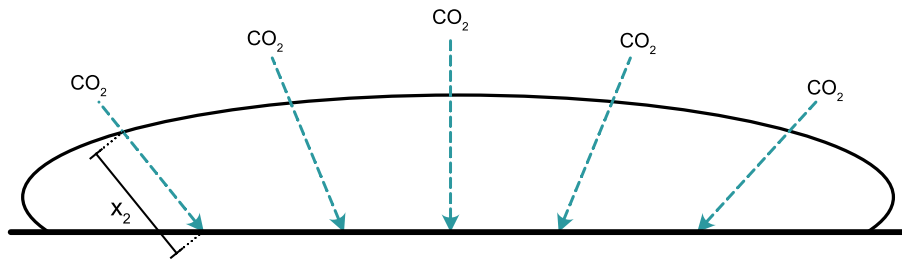
	Observed maximum mass loss (%)	Modelled maximum mass loss; parameter A (%)	Modelled 50% setting completion point; parameter B (hours)	Michalis-Menton R²
Droplet (n=2)	46.3	44.0	1.3	0.993
Disc (n =1)	46.0	47.4	13.8	0.915

Table 4-2. Mass loss data from sodium silicate setting kinetics and Michalis-Menten equation modelling.

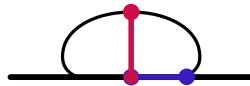
a) droplet specimen



b) disc specimen



c) droplet specimen



d) disc specimen

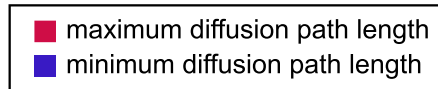
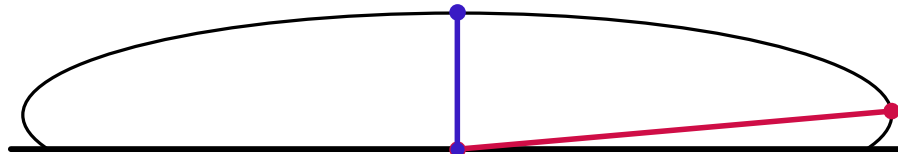


Figure 4-3. Schematic depiction of CO₂ gas diffusion through sodium silicate specimens in (a) droplet and (b) disc geometry, during setting in ambient conditions on an impermeable substrate (i.e., Parafilm M). The path length for droplet geometry, x_1 , is less than that for disc geometry, x_2 ; this shorter path length results in a more rapid reaction rate. The approximate minimum and maximum diffusion path lengths are schematically illustrated for (c) droplet and (d) disc specimens. The diffusion path length, and diffusion barrier, is lower for droplet geometry; the diffusion barrier length of the set sodium silicate is of particular consequence to setting reaction rate (further detailed in Figure 4-5).

The kinetics data for both geometries is shown fitted to a modified Michaelis-Menten model in Figure 4-4, which was used to determine the asymptotic mass loss (i.e., modelled maximum mass loss) and 50% setting completion. For all specimen geometries, setting proceeds as a ‘moving front’ through the material—this setting results in the rapid formation of a high-viscosity surface layer that acts as a significant diffusion barrier for CO₂ gas [6], resulting in a rapid decrease in reaction rate. This process is depicted in Figure 4-5.

Setting kinetics were used to determine mould residence times for composite scaffolds—no composite specimens were removed from moulds before achieving 75% of predicted mass loss, and no composite specimens were tested before achieving 95% of predicted mass loss. Kinetics data from bulk sodium silicate specimens were used as a conservative guideline for setting times; as the composite specimens have a shorter CO₂ diffusion path length than the kinetics specimens (19-57 μm; Chapter 4.4.1), it is expected that the binder phase present in composites will reach the stable, asymptotic region of the kinetic curve in less time than a bulk specimen.

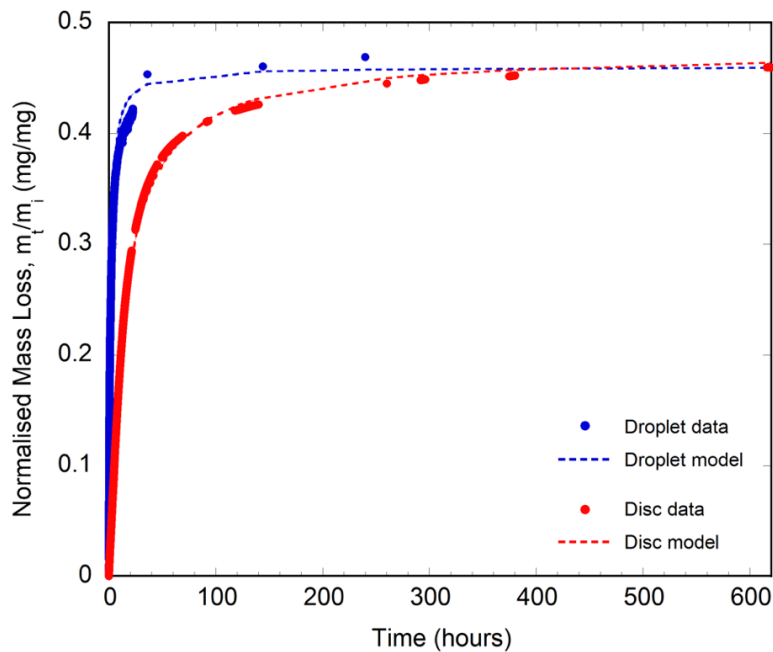


Figure 4-4. Kinetics data and curve fit for the mass loss during setting of bulk aqueous sodium silicate in air at 294 K (21 °C), for droplet geometry (blue) and disc geometry (red). The curve fits (dotted lines) are based on the Michaelis-Menten equation describing a reaction as a function of concentration of reactants which decreases over time. Bulk sodium silicate setting kinetics were used as a conservative control for establishing minimum mould residence times for composite scaffolds.

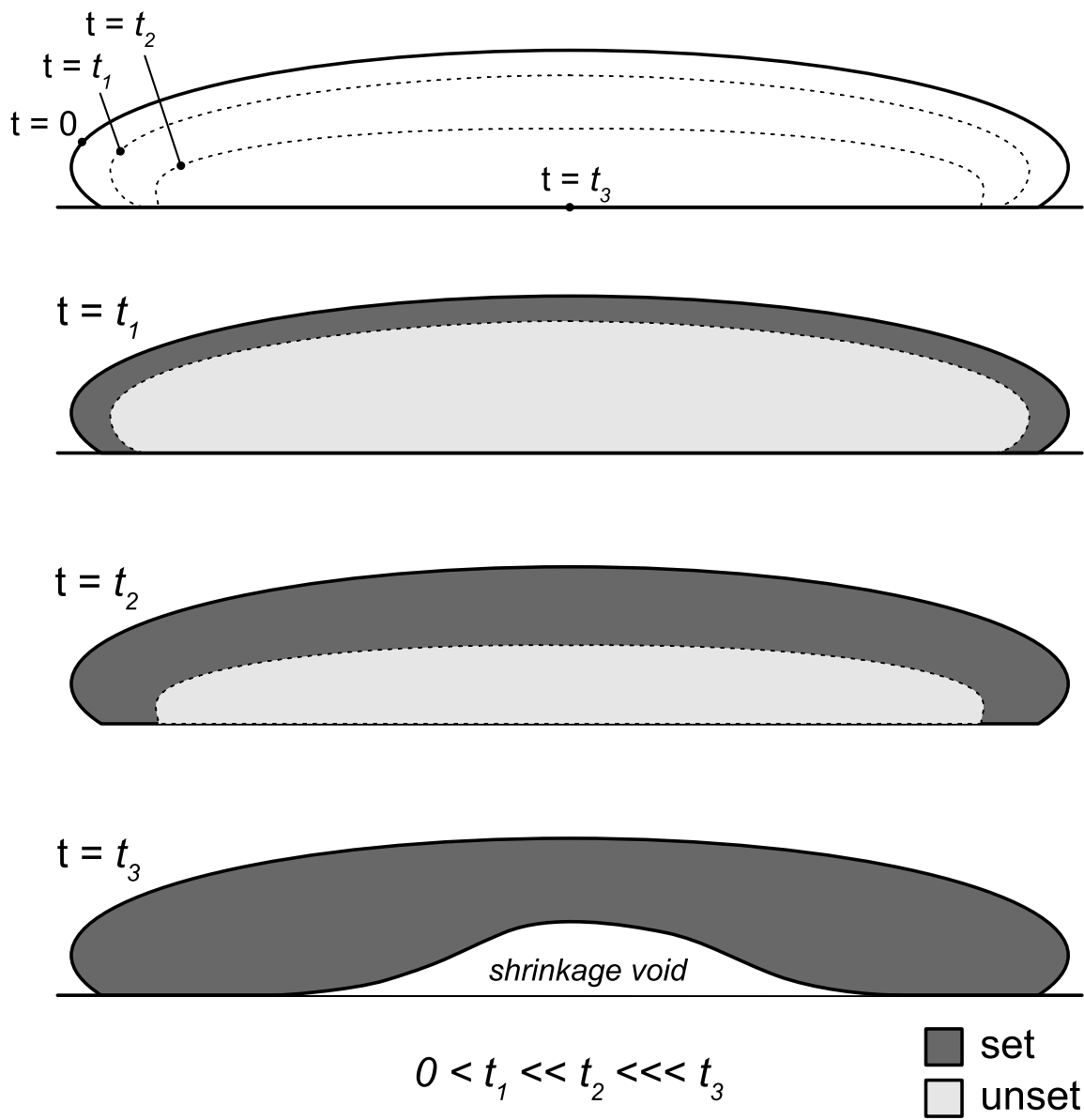


Figure 4-5. Schematic depiction of the ‘moving front’ of set material through bulk sodium silicate during setting in ambient conditions. The initial formation of a ‘skin’ at $t = t_1$ is rapid, but this rigid boundary severely impedes the diffusion of carbon dioxide gas, markedly decreasing the rate of reaction. As this ‘moving front’ of set material increases, the diffusion barrier increases proportionally, resulting in the asymptotic reaction rate seen in Figure 4-4. Due to the densification during setting, a shrinkage void may form in the centre of the monolithic sodium silicate.

4.2 Formability

Formability of the different compositions was assessed using the following criteria: 1) manipulation time; 2) set time; 3) porosity prior to compaction. Preliminary screening trials for potential specimen compositions established formability as the upper bound; unset paste compositions with an excess of binder phase were not viscous enough to be formed into undercuts and were neither porous nor compactable. The resultant specimens from these trials are shown in Figure 4-6; scaffold compositions with 29.4 vol% binder were not capable of being compacted. The implications of the excess binder phase on phase distribution was further explored with micro-CT in Chapter 4.4.4. The lack of porosity in the unset paste with high amounts of binder phase also resulted in unfeasible setting times; without this porosity, the surfaces exposed to atmosphere set and formed a diffusion barrier that was severely rate-limiting for any further reaction, as described by Atterton [6]. The highest composition of binder phase found to satisfactorily fulfil the criteria for formability was 16.1 vol%.

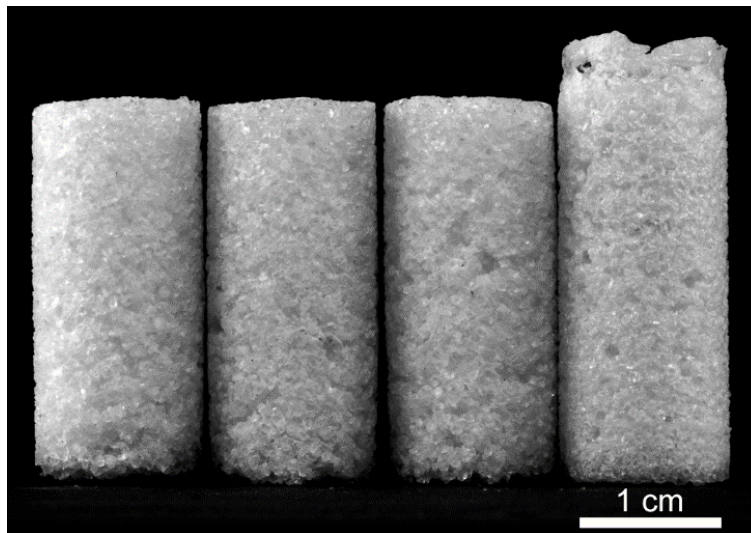


Figure 4-6. Cylinder specimens (Type B) prepared using 7.4, 11.4, 16.1, and 29.4 vol% binder phase (left to right respectively)—all cylinders were fabricated with the same amount of bioactive glass frit. Note the height difference of the 29.4 vol% specimen, which is due to the non-porous unset paste. The excess unset binder in the 29.4 vol% composition results in an incompactable paste that lacks the high formability as contrasted to the other compositions [7].

The previously defined *manipulation time* of the unset paste increased with increasing binder phase; the manipulation times of the 7.4, 11.4, and 16.1 vol% compositions were 2, 5, and 8 minutes, respectively. The cohesive, formable nature of the unset paste is shown in Figure 4-6. The shorter manipulation times in lower binder phase compositions were due to the increased surface area to volume ratio of the binder phase—a thinner binder coating on the particles resulted in a more rapid setting reaction due to a smaller diffusion path length. The higher porosity associated with a lower binder phase composition likely also reduced the mass transport limitations of CO₂ gas diffusion into the pores.

The porosity of the unset paste prior to compaction allowed it to be formed into undercuts, ridges, and other unique geometries. The resolution to which the paste maintained these geometries after setting is examined further in Chapter 4.3.

4.3 Geometric Stability

Geometric stability of the set paste was evaluated by assessing the structural integrity of the specimens during handling and mould geometry reproduction accuracy. Reproductions of a right circular cone (specimen type C) and circular paraboloid (specimen type D; recall Table 3-1) were analysed via dimensional differences between the set composite scaffold and the mould.

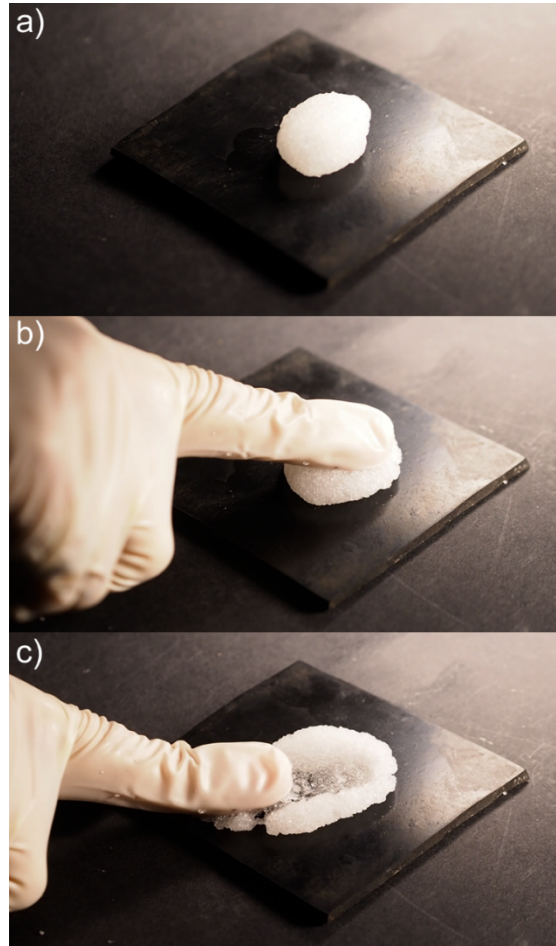


Figure 4-7. Manual compression and shearing of unset paste (within the manipulation time) of approximately 16.1 vol% binder phase (after setting) composite paste [7].

The aforementioned screening trials for determining possible specimen compositions established geometric stability as the lower bound; set specimens with too little binder phase were unable to maintain mould geometry, were friable, and crumbled when handled. The densification of the sodium silicate constituent during setting reduces the total volume of binder phase, and this reduction of volume leads to insufficient set binder to fix the bioactive glass frit into a rigid scaffold (no bulk composite shrinkage was observed). The lowest composition of binder phase found to satisfactorily fulfil the criteria for geometric stability was 7.4 vol%.

To measure the extent to which the set scaffold specimens retained their as-moulded geometry, the reproduction of specimen types C and D were compared to the original

positive mould (Figure 4-8). The intermediary Reprorubber negative mould was assumed to be within submicron resolution reproduction of the original positive mould based on technical product literature and claims therein [8], hence direct comparison was made between the set scaffold geometries and the positive mould geometries. The overall reproduction accuracy of the ceramic paste composite to the original mould was excellent; a small loss of resolution can be seen in the tip of the cone (specimen type C), likely due to de-moulding and handling. Excellent geometric reproducibility is evidenced by the negligible differences in geometric shape parameters (right hand images in Figure 4-8). Dimensional analysis revealed the diametrical difference at the base to be $\leq 5\%$ for the circular paraboloid and $\leq 2.5\%$ for the cone; height difference at the centre was $\leq 0.6\%$ for the circular paraboloid and $\leq 7.6\%$ for the cone. Resolution differences can be observed in the paraboloid (specimen type D) as missing particles of glass along the edge of the specimen.

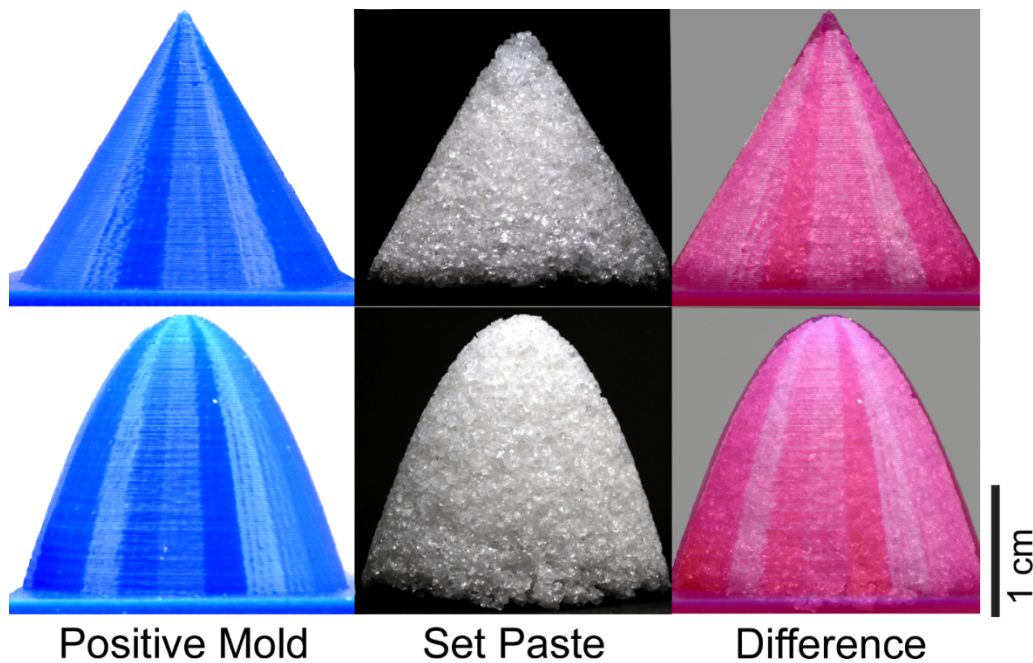


Figure 4-8. 3D printed positive mould (left); 7.4 vol% set specimens de-moulded from the mould shown in Figure A2-3b (middle); image created from superposing the set paste and positive mould images to highlight the different in edge profile, and geometry (right; false-coloured positive mould). The minor difference in geometry, seen at far right, indicates that the set paste exhibits excellent reproducibility [7].

4.4 Porosity

4.4.1 Optical Light Microscopy with Epoxy Infiltration

All composite compositions tested with epoxy infiltration were found to have all examined pores filled with epoxy when observed with OLM, indicative of an interconnected porous network. Figure 4-9 illustrates the dispersion and distribution of each phase (bioactive glass frit, set sodium silicate binder, and pores)—for all compositions, the structure of the scaffold was created by the packing of the frit and fixed with a conformal binder coating of set sodium silicate (binder phase). Average 2-dimensional pore size ranged from 156.4-285.1 μm (Table 4-3), distributed over the face of the specimen. The average thickness of the binder coating was found to range from 19.0-57.0 μm , increasing with increasing vol% sodium silicate binder (Table 4-4). The shrinkage cracks seen throughout the sodium silicate binder phase were due to the densification of aqueous sodium silicate post reaction with CO_2 (47% as determined by gas pycnometry, Chapter 4.4.3). The shrinkage cracks in the binder coating were also observed to be vertical (all compositions, see Figure 4-9, black arrows) and lateral cracks (in the plane of the coating) for the highest vol% coatings (see Figure 4-9, white arrows).

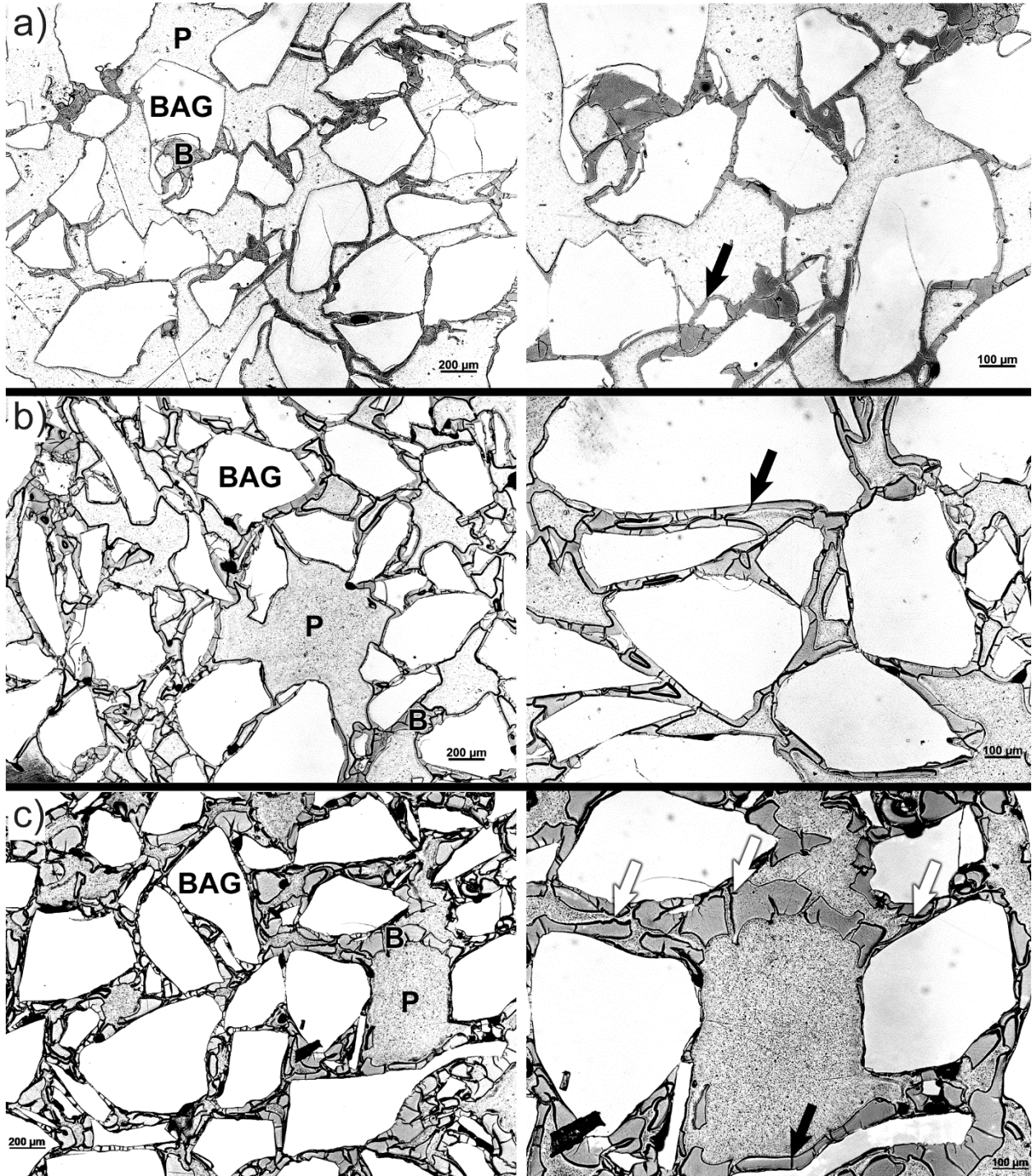


Figure 4-9. Bright-field OLM images of (a) 7.4, (b) 11.4, and (c) 16.1 vol% binder composites after epoxy vacuum- infiltration (higher magnification images at right). 'BAG' is bioactive glass frit particle; 'B' is binder phase; 'P' is pore. Black arrows indicate vertical cracks in the binder phase and white arrows indicate lateral cracks in the binder phased. As binder amount increases from (a) to (b) to (c) both the distribution and dispersion of the binder phase become more uniform, whilst porosity exhibits the opposite trend and also decreases in overall amount [7].

Composition (amount of binder)	Average pore size (um)	Standard deviation (um)	Minimum pore size (um)	Maximum pore size (um)
7.4 vol%	285.1	215.5	45.4	1061.5
11.4 vol%	202.2	212.0	26.0	998.8
16.1 vol%	156.4	120.0	38.3	647.9

Table 4-3. Average 2-dimensional pore size as a function of binder phase vol%, determined via OLM [7].

Composition (amount of binder)	Average binder thickness (um)	Standard deviation (um)	Minimum binder thickness (um)	Maximum binder thickness (um)
7.4 vol%	19.0	6.0	10.5	27.2
11.4 vol%	31.9	17.0	12.6	79.3
16.1 vol%	57.0	4.0	16.5	106.0

Table 4-4. Average binder coating thickness as a function of binder phase vol%, determined via OLM [7].

4.4.2 Scanning Electron Microscopy

SEM was used to image unpolished, as-processed specimens to examine the morphology of the composite scaffold. Micrographs in Figure 4-10 further illustrate the porous, interconnected scaffold formed after setting and the effect of composition on the structure of the specimens. The thicker layers of solid sodium silicate in 11.4 vol% and 16.1 vol% specimens resulted in increased delamination and larger cracks in the binder phase.

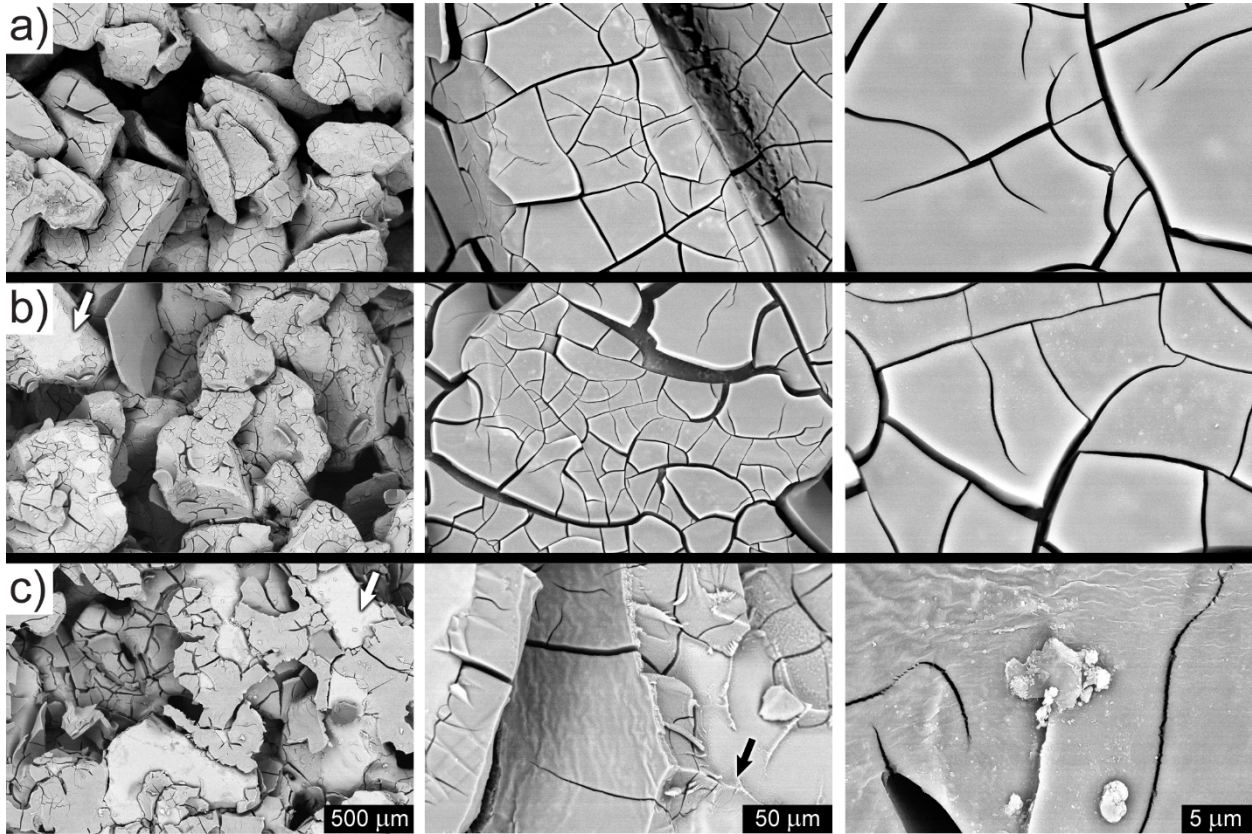


Figure 4-10. Back-scattered electron (BSE) SEM micrographs of (a) 7.4, (b), 11.4, and (c) 16.1 vol% composites. While the binder coating on the bioactive glass frit appears to have complete coverage it also has extensive cracking, which resembles mud-cracking, thus indicating shrinkage cracking (presumed to have occurred during the setting of the binder phase). White arrows in (b) and (c) indicate regions where the binder phase has spalled revealing the bioactive glass frit surface. The black arrow in (c) indicates a remnant ridge of binder phase in contact with the bioactive glass frit particle, which indicates the possibility of chemical reaction and bonding of the binder to the bioactive glass [9].

4.4.3 Gas Pycnometry

Nitrogen gas pycnometry confirmed the open porosity of all scaffold compositions; as anticipated, porosity was found to be inversely proportional to the amount of binder phase present (Figure 4-11). The compositions tested were successful in producing open porous networks; closed pores were found to be less than 1.1% for all compositions.

Gas pycnometry was also used to determine the volume percent of each constituent phase present in the set scaffolds (Table 7, Figure 10) and quantify the density change that occurs during the setting reaction of aqueous sodium silicate. After reacting with CO₂ gas in atmosphere, sodium silicate was found to have a density of 2.07 g/cm³ (a 46.8% increase from the unset density of 1.4 g/cm³).

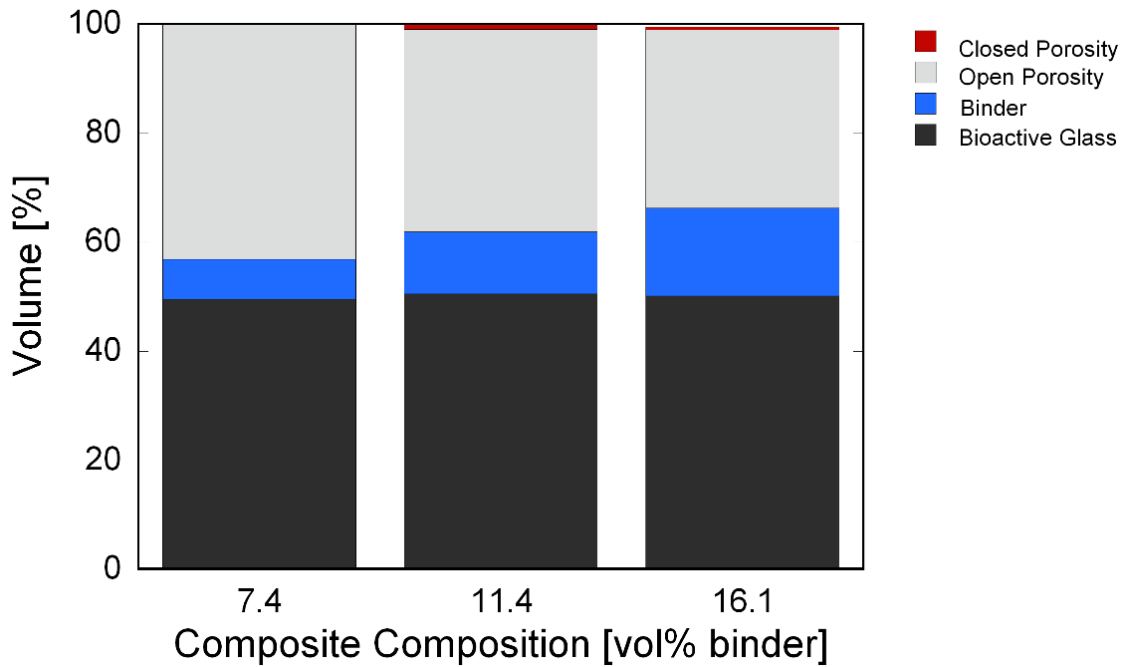


Figure 4-11. Volume percent of each constituent phase in set composite scaffolds, as determined by gas pycnometry. Whilst the bioactive glass volume fraction is relatively constant (within 1 vol%) the binder has a negative correlation with open porosity. Closed porosity is minimal in all composites, with no observed consistent trend between compositions [7].

	45S5 frit (vol%)	Sodium silicate (vol%)	Open pores (vol%)	Closed pores (vol%)
Composition I	49.5	7.4	43.0	0.08
Composition II	50.6	11.4	37.1	1.1
Composition III	50.2	16.1	32.7	0.5

Table 4-5. Composition of composite scaffolds determined by gas pycnometry [7].

Porosity values calculated from gas pycnometry were confirmed using porosity analysis from micro-CT (Chapter 4.4.4).

4.4.4 Micro-Computed Tomography

Porosity, phase distribution, and scaffold structure were verified using micro-CT, generating a 3D model of each investigated composition (7.4, 11.4, 16.1, and 29.4 vol% sodium silicate).

Porosity values calculated from micro-CT were within 3.2-6.8% agreement with those calculated using gas pycnometry (Table 4-6). The homogenous distribution of binder phase throughout the bulk was confirmed using porosity measurements from the upper, middle, and lower 10% of each specimen (Figure 4-12). This consistent phase distribution is present in the selected compositions due to the viscosity of aqueous sodium silicate and its wetting behaviour on bioactive frit.

The surface area to volume ratio (SA/V) was determined to decrease with increasing binder phase amount, as shown in Table 4-7. The variation in SA/V across the height of the specimen increases with increasing binder phase, indicating an inverse relationship between binder phase amount and spatial distribution. Increasing binder phase amount thus may increase variability in physical properties of the scaffold, as is further investigated in Chapter 4.5. The specimen compositions investigated have an average SA/V of 18.9-32.7 mm⁻¹, which is within the range of trabecular bone. A high SA/V is advantageous in bone tissue scaffolds as it can increase the rate of osteoinductive surface reactions (recall Figure 2-2) *in vivo*, accelerating integration with surrounding biological tissues [10, 11].

The distribution of pores is similarly consistent, as shown by 3D reconstructions of the scaffolds (Figure 4-13), which is necessary for successful bone tissue integration [10]. Additionally, the screening of 29.4 vol% binder composition was confirmed with micro-CT, illustrating regions of 0% porosity (indicated by the black phase) and the overall maldistribution of binder phase (dark grey phase in Figure 4-12, Figure 4-13).

Composition (amount of binder)	Average open porosity (%)	Standard deviation (%)	Difference in average porosity between micro- CT and pycnometry (% difference)
7.4 vol%	44.3	0.7	3.2
11.4 vol%	34.6	1.1	- 6.8
16.1 vol%	31.1	0.8	- 4.8
29.4 vol%	39.2	15.0	N/A

Table 4-6. Average open porosity as a function of composite composition for micro-CT investigations [7].

Composition (amount of binder)	Average surface area to volume ratio (SA/V; mm⁻¹)	Standard deviation of SA/V (mm⁻¹)	SA/V of trabecular bone (mm⁻¹)
7.4 vol%	32.7	0.7	6-15 [44]; 10-30 [43]
11.4 vol%	23.3	2.7	
16.1 vol%	18.9	3.6	

Table 4-7. Surface area to volume ratio (SA/V) of set scaffolds as a function of binder phase, as determined by micro-CT. Volume percent of binder phase is inversely proportional to SA/V; increasing binder phase corresponds to an increase in SA/V variance over the height of the specimen. SA/V data ranges for trabecular bone taken from [44, 43] [7].

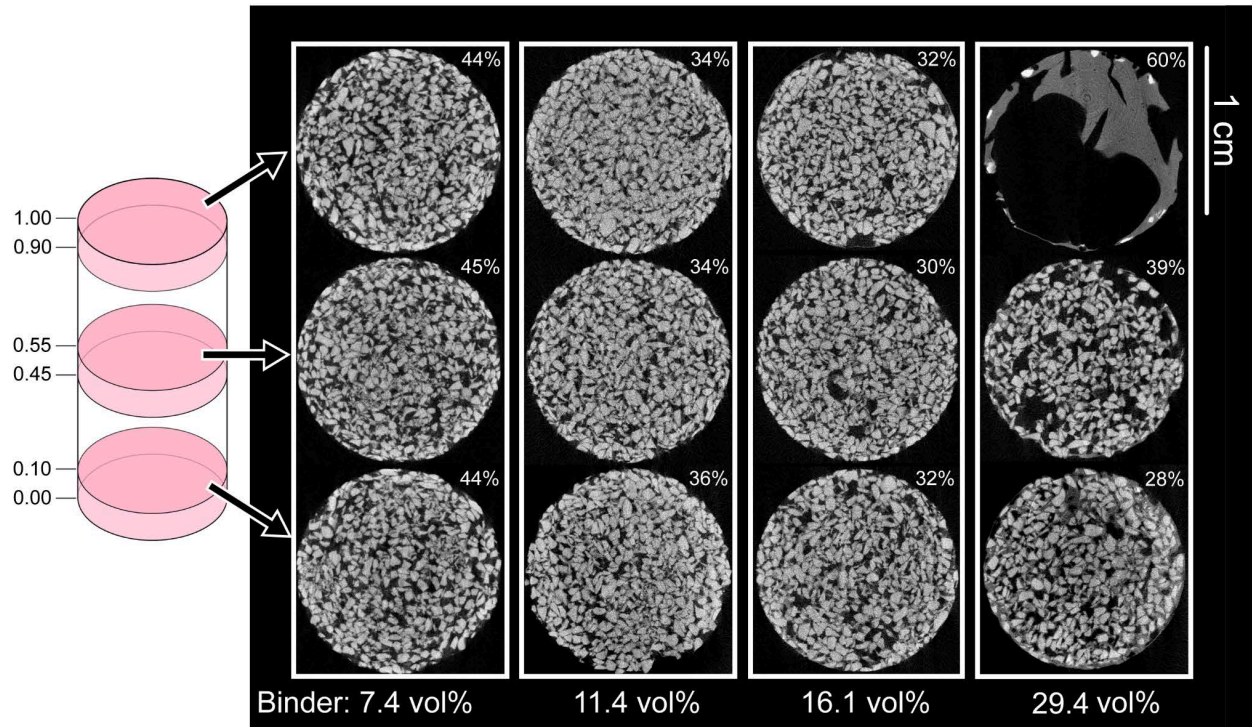


Figure 4-12. Thin-section axial micro-CT reconstructions at height fractions, h , centred at 0, 0.5, 1.0 of each specimen, illustrating the distribution of phases as a function of height and composition (black = porosity; light grey = bioactive glass frit; grey = binder). Diameter of each reconstruction is 12 mm. For the first three compositions: as the binder amount is increased (from left to right) the total volume of porosity per slice decreases (as indicated by the percentages listed by the reconstructions); the porosity is not well distributed nor dispersed in the 29.4 vol% composite, and contains very large pore defects and agglomerated binder phase zones (e.g., top right image) [7].

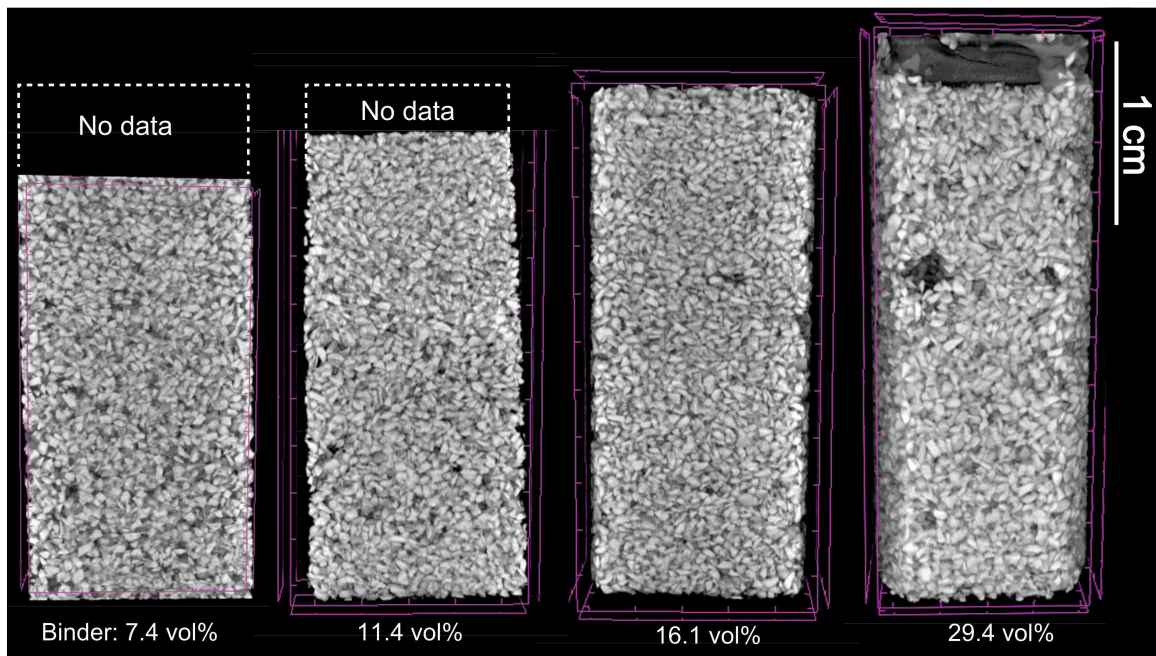


Figure 4-13. Thin vertical sections of micro-CT reconstructions for the various composite compositions. Bioactive glass particle packing is relatively consistent in all compositions except for bulk defects (large voids and bulk binder) observed in the 29.4 vol% specimen, especially near the mid-plane and at the top surface (far right) [7].

Alternative 3D renderings of the composite scaffolds (Figure 4-14) show the distribution of both open and closed pores, as well as their respective volumes. As illustrated in Figure 4-14, each composition was found to have interconnected open porous networks (shown in green) throughout the entire specimen; as aforementioned, volume percent of open pores decreased with increasing binder phase amount. Closed pores (shown in red) were found to be comparatively negligible, comprising less than 0.24 vol% of any specimen.

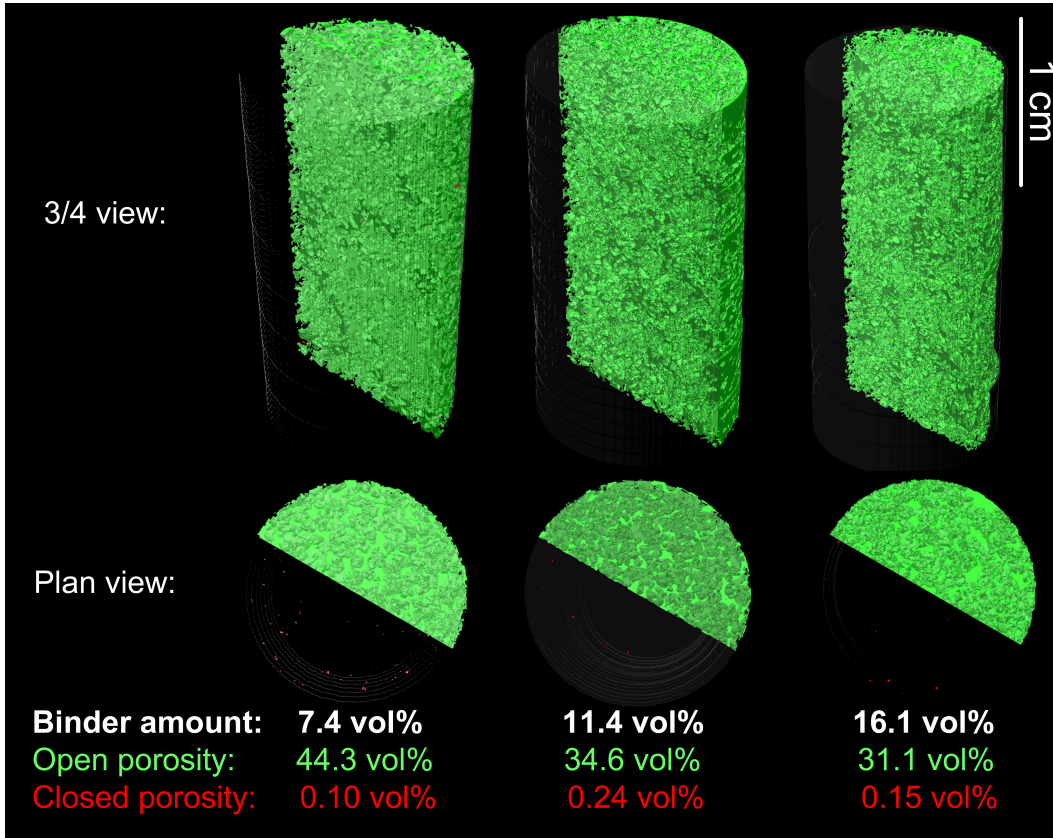


Figure 4-14. Digital 3D reconstructions of composite scaffold specimens. Half of the cylindrical specimen shows the network of open, interconnected pores in green, while the other half shows isolated closed pores, illustrated in red [9].

4.5 Load-Bearing Capacity

The composite scaffolds investigated in unconfined compression testing showed a moderate increase in UCS with increasing binder phase, and a pronounced increase in UCS variability with increasing binder phase (Table 4-8). Average UCS values for compositions of 7.4, 11.4, and 16.1 vol% binder were 1.30, 2.16, and 4.42 MPa, respectively. The UCS values obtained for this material are slightly lower than the range for trabecular bone (8-50 MPa) and considerably lower than the range for cortical bone (150-200 MPa) [12]; however, the design criterion was not to mimic the strength of native bone, but rather to provide sufficient interim mechanical stability until tissue in-growth and resorption have occurred. Additional

mechanical testing *in vitro* or *in vivo* should be planned to elucidate the effect of biological factors on strength and strength retention.

Composite Binder Amount	Sample Size, N	Mean UCS (MPa) +/- One Standard Deviation	Median UCS (MPa)	Minimum UCS (MPa)	Maximum UCS (MPa)
7.4 vol%	12	1.30 +/- 0.34	1.32	0.85	1.98
11.4 vol%	13	2.16 +/- 1.01	1.68	1.30	4.10
16.1 vol%	16	4.42 +/- 2.88	3.23	1.26	9.77

Table 4-8. Unconfined compressive strength of ceramic composite scaffolds as a function of binder amount [9].

Scaffolds tested in unconfined compression testing revealed a positive correlation of UCS with increasing binder phase amount (with concomitant increased variability) (Figure 4-15; Table 4-8); mean values of UCS were: 1.30, 2.16, and 4.42 MPa for 7.4, 11.4, and 16.1 vol% binder respectively. The multiple peaks in the stress-strain curves (Figure 4-15) are typical of crushing in porous solids. The load drops are associated with binder neck fracture and the subsequent increases in stress are a result of the reorganization of the frit into pore spaces (powder compaction) wherein they wedge against each other to densifying the specimen, thus resulting in higher strength. The process repeats itself until there is no longer any load carrying capability.

The relationship of failure mode to UCS is depicted in Figure 4-16. Specimens predominantly failed in single shear (Figure 4-16a), with variability in failure mode increasing with increasing amount of binder phase—likely a result of the corresponding increased variability in distribution of the binder phase within the scaffold. Specimens with mixed mode failure (Figure 4-16b) failed at considerably higher strengths than those failing in single or double shear.

In accordance with the sodium silicate setting kinetics established in Chapter 4.1.2, mechanical testing was only conducted on specimens that had reached at least 95% of expected mass loss due to setting. Mechanical test specimens were tested at least 5 days after processing, and up to 199 days after processing. To ensure that specimen age beyond 5 days

did not significantly affect mechanical properties, the coefficient of determination (R^2) was calculated for the relationship between specimen age and UCS. The values of R^2 for 7.4, 11.4, and 16.1 vol% specimens were 0.106, 0.249, and 0.022, respectively—indicating that specimen age (after > 95% mass loss) had no significant impact on measured UCS (Figure 4-17).

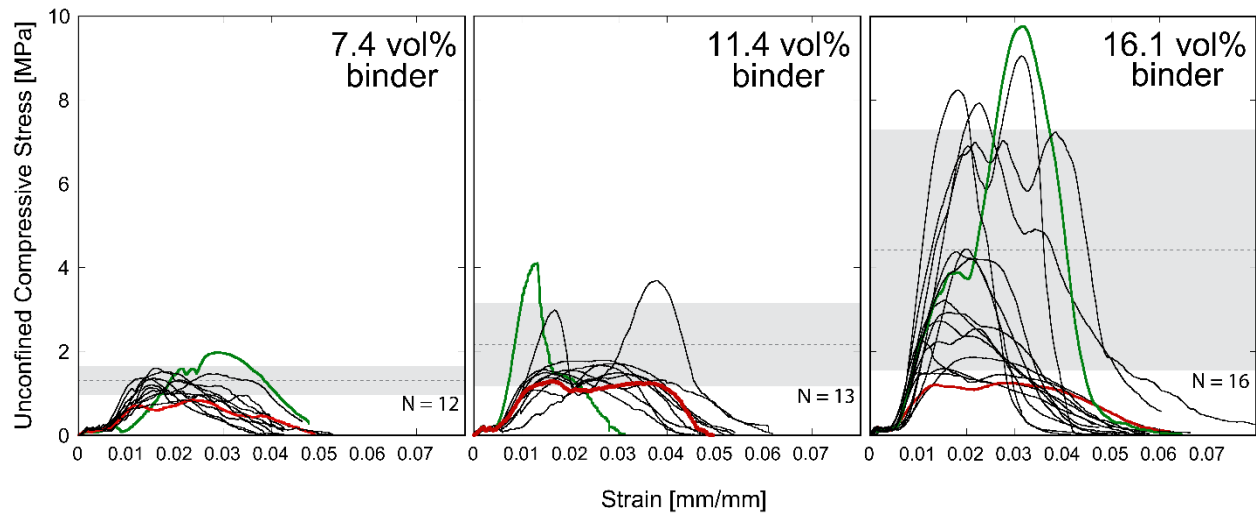


Figure 4-15. Unconfined compression strength testing data as a function of composite composition (vol% binder). All data are shown, with sample size indicated by N in the graphs. The grey band indicates +/- one standard deviation of the mean of the data set (horizontal dashed line). The red and green lines represent the specimens with the lowest and highest unconfined compressive strength (UCS) respectively, for each composition. The magnitude (and standard deviation) of the UCS is positively correlated with amount of binder phase [9].

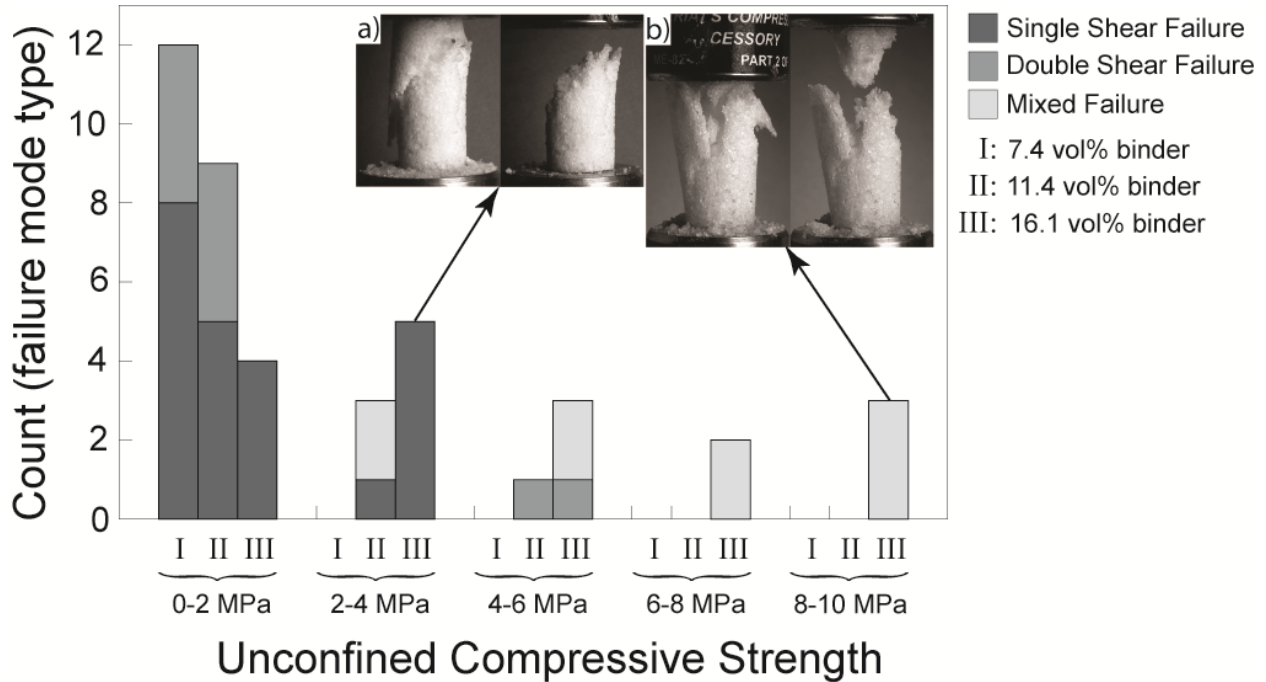


Figure 4-16. Inset images: time lapse photographs of 16.1 vol% binder compression specimens illustrating fracture in (a) single shear and (b) mixed failure modes—mixed failure mode was found to have a mild positive correlation with amount of binder and UCS. Single shear failure mode was more predominant at low values of UCS, but was not correlated with binder amount [9].

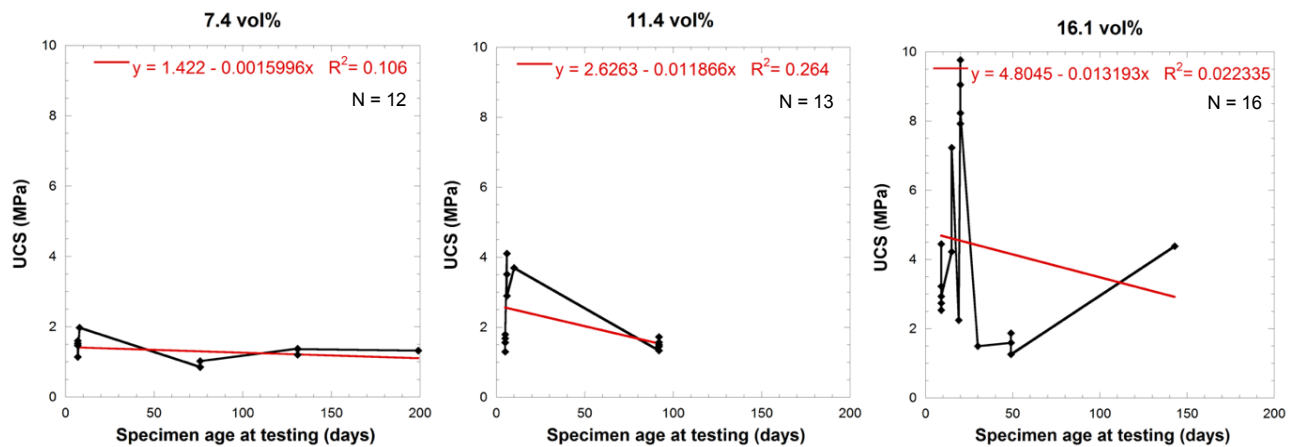


Figure 4-17. Correlation plots of UCS as a function of specimen age at testing, overlaid with best-fit linear regression (red line). Each datum point represents one specimen. As is evidenced by the lack of fit and low correlation coefficient, the specimen age (after < 95% mass loss; i.e., after 5 days) had no significant effect on the measured UCS values.

4.5.1 Scanning Electron Microscopy Fractography

Upon examining the fracture surfaces of failed specimens under SEM (Figure 4-18), evidence for both cohesive failure in the binder phase and adhesive failure between phases was found. No evidence of cohesive failure within the bioactive glass frit was observed. Most of the BAG frit surfaces remained coated in binder phase, however increased spallation and some delamination of the binder phase was indicative of adhesive failure of the binder phase, which likely included some cohesive failure in the binder neck regions as well. Adhesive failure between the two constituents can be seen in previous binder necks between two pieces of de-adhered frit. After failure, the surface of the binder phase is roughened (from deposits of micro-debris) and partially or completely delaminated from the bioactive glass frit, as indicated by black arrows in Figure 4-18.

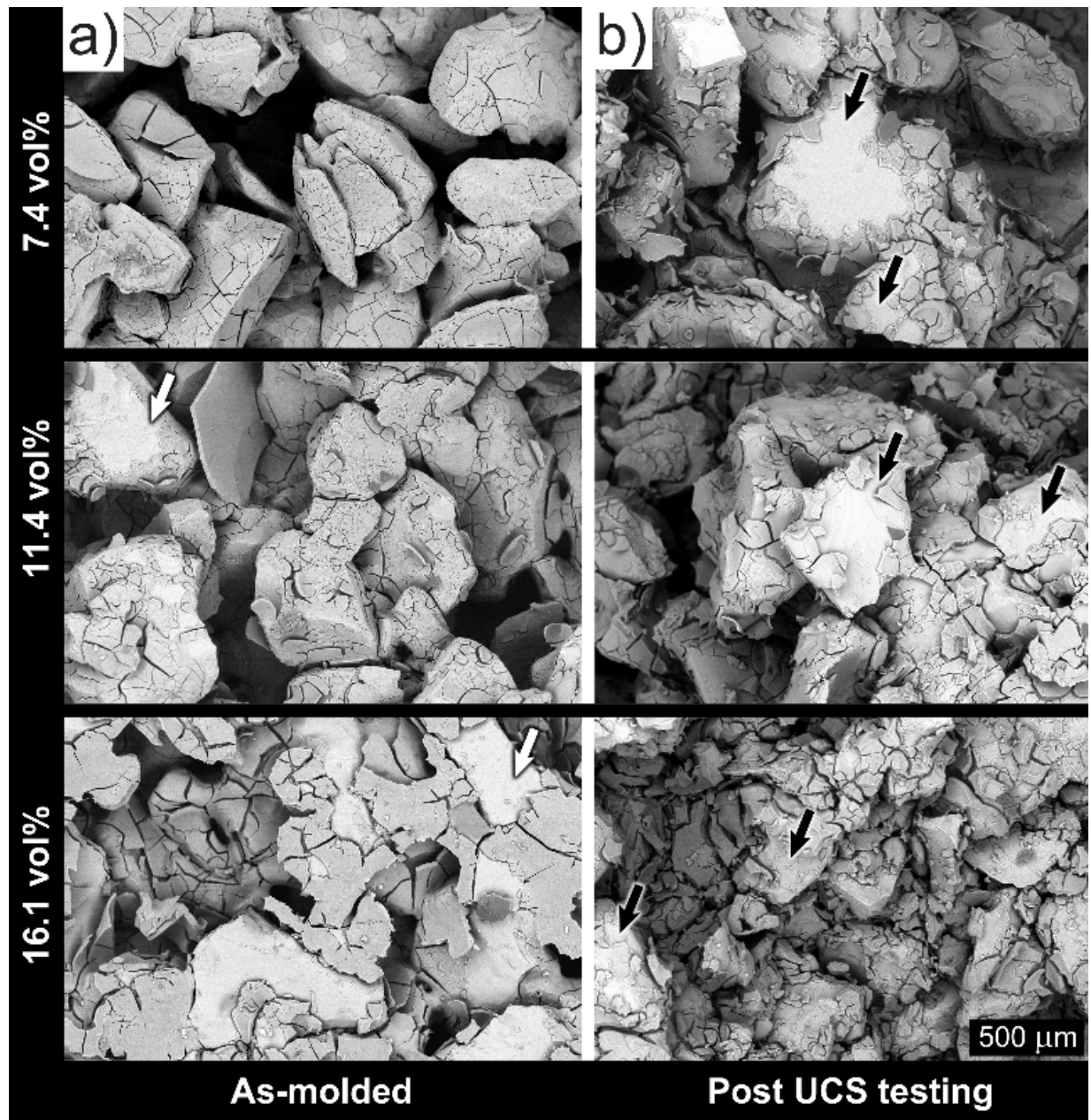


Figure 4-18. BSE SEM micrographs of (a) as-moulded and (b) post UCS tested (fractured) composite specimens, showing the increased extent of delamination and spallation of the binder phase that occurs after compressive failure. White arrows indicate binder spalls prior to UCS testing, whereas black arrows indicate BAG frit g which have spalls post testing. In the middle panel of (b), at the far-right black arrow, the adjoining two particles also appear to have spalls in the binder coating. The primary damage mode appears to have been adhesive failure of the binder phase to the BAG frit particles [9].

4.6 Bioactivity

4.6.1 Macro *in vitro* Behaviour

Composite specimens were found to maintain overall geometrical stability throughout the length of the *in vitro* immersion test (14 days), though the structural integrity of specimens during handling decreased with increasing immersion time. Specimens with higher vol% binder phase were found to be more friable after *in vitro* immersion than lower vol% specimens. This change in stability is likely due to the hydration and swelling of the binder phase, which results in internal forces within the scaffold that may reduce its structural integrity.

Sodium silicate control specimens formed a weakly consolidated, hydrated gel with a supernatant liquid when *in vitro*, seen at each time point (1, 3, and 14 days). This gel formation is consistent with the behaviour previously described by Tognonvi et al. [13]. Constituents of the SBF were found to have infiltrated the sodium silicate gel network, as shown by XRD analysis (further explored in Chapter 4.6.3).

All composite specimens were observed to deposit residue after 1 day *in vitro* immersion (11.4 vol% and 16.1 vol% specimens) or 3 days immersion (7.4 vol% specimens). Amount of residue was found to increase with increasing binder phase amount. Additionally, samples with higher amounts of binder phase were found to deposit more residue *in vitro* (white arrows in Figure 4-19), effectively reducing the amount of binder phase present in the specimen and lowering its structural integrity. FTIR analysis of this residue was conducted to determine its chemistry, detailed in Appendix V. Identification of bonds present in the residue revealed the presence of species present in SBF, bioactive glass, and sodium silicate, indicating that the residue is likely a combination of all components of the *in vitro* system.

Following removal from SBF and air-drying, 16.1 vol% composite specimens examined under stereomicroscopy were found to have formed a brighter white phase

between grains of bioactive glass frit (Figure 4-20). This phase is most likely dried binder that had been previously hydrated with SBF; hydrated sodium silicate control specimens were also found to form a bright white solid after drying in air. When possible, FTIR analysis was conducted on excised pieces of this brighter white phase; this characterisation is further explored in Appendix V.

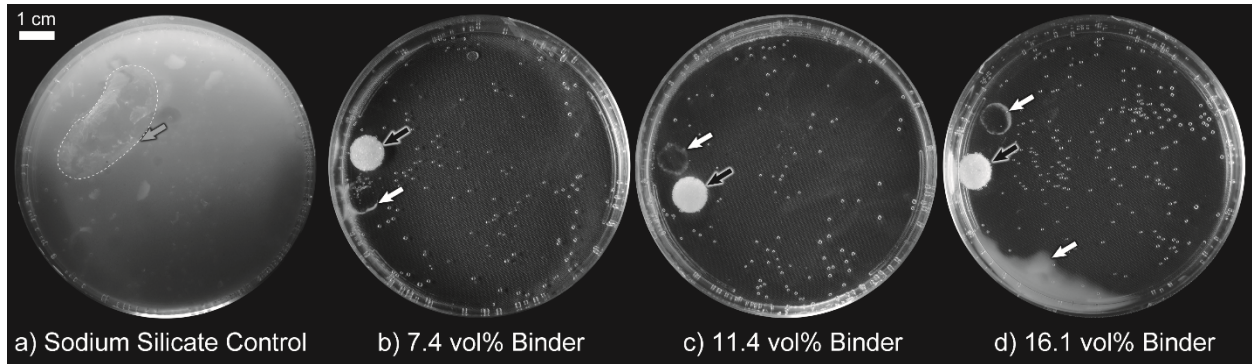


Figure 4-19. Petri dishes with a) control (original shape of the set sodium silicate control specimen is indicated by a white dashed line at left), and (b-d) composite scaffold specimens after 3 days *in vitro* immersion (air bubbles are visible in petri dishes for scaffold specimens). (a) the cohesive, hydrated gel formed by the sodium silicate control specimen (grey arrow) clouded the entire petri dish with gel. Composite scaffold specimens (black arrows in b-d) were moved to display the gel-residue deposited by the gelation of the binder phase (white arrows). Volume of the gel-residue from composite specimens was found to increase with increasing binder phase (white arrows in (b-d)). The frit control did not produce any gel-residue [9].



Figure 4-20. Stereomicrographs of composite specimens following 14 days *in vitro* immersion. The brighter white phase seen between grains of bioactive glass frit in the 16.1 vol% specimen was characterised via FTIR analysis (Appendix V).

The pH of the spent SBF was measured intermittently throughout immersion, shown in Table 4-9. The purpose of pH measurement was to ensure that the alkaline nature of the soluble binder phase was within the range of pH values observed for bioactive glass control specimens; though the pH is initially quite high (c. 11), this was observed for frit control specimens behaved similarly. The alkalinity decreases after the SBF is refreshed, indicating that the dissolution products are not released at the same rate or concentration after initial hydration. The highly alkaline nature of the dissolution products from bioactive glass are what produce a locally antibacterial environment, which has been found to be beneficial for bone healing [14]. Moreover, the high pH is buffered by bodily fluids *in vivo*, containing the alkaline environment to the bone defect site [15].

	3 day (no exchange of SBF)	6 day (1 exchange of SBF)	14 day (5 exchanges of SBF)
Bioactive glass frit control	c. 10	c. 8	No data.
Sodium silicate control	c. 11	c. 10	c. 9
7.4 vol%	c. 11	No data.	c. 8
11.4 vol%	c. 11	No data.	c. 8
16.1 vol%	c. 11	No data.	c. 8

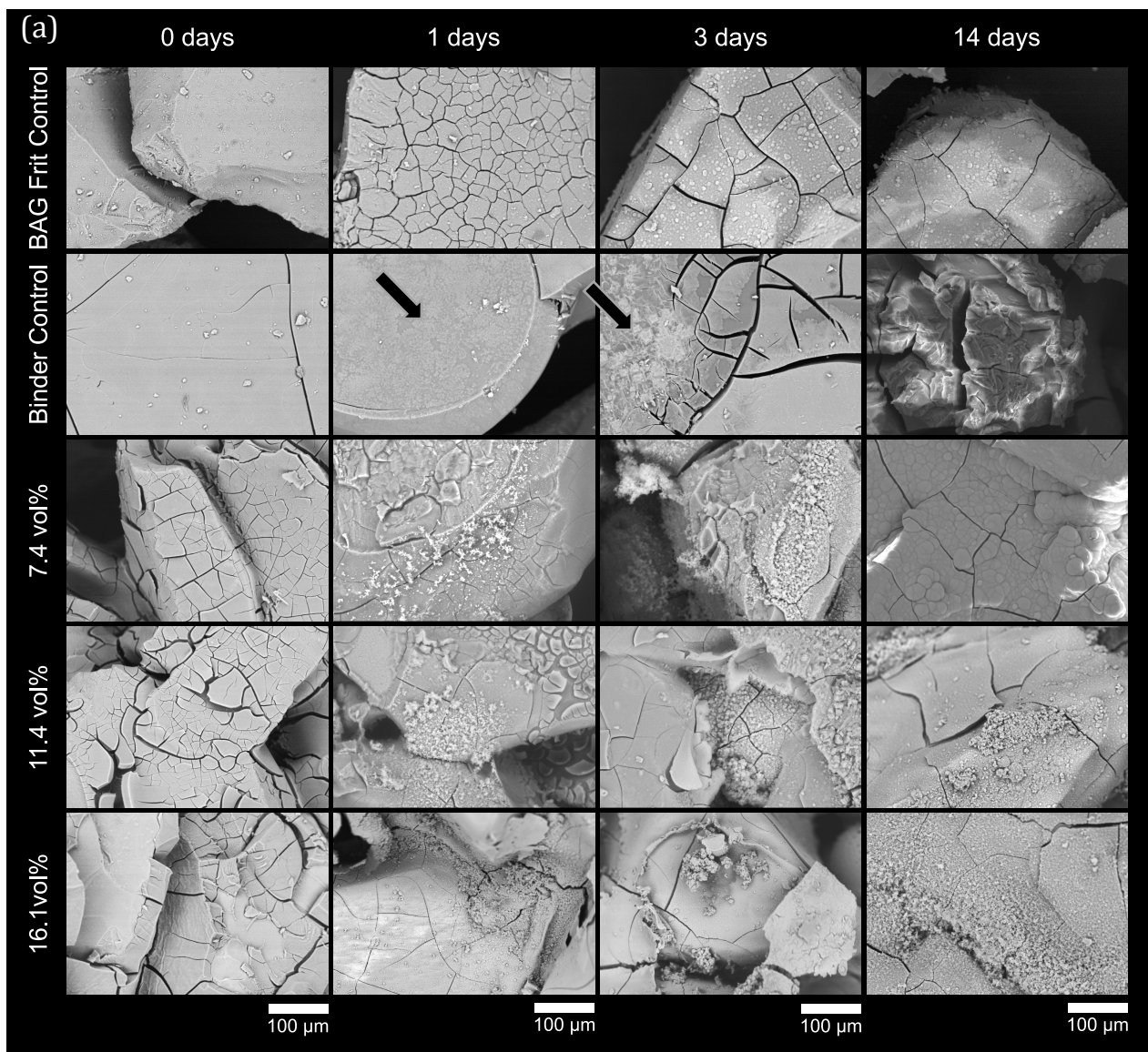
Table 4-9. pH measurements of spent SBF during *in vitro* immersion testing. Values are approximate, as pH was measured with pH testing strips. Though the pH of sodium silicate control specimens and composite specimens is initially high, it is within the range of bioactive glass, which has been shown to possess beneficial antibacterial properties due to the alkalinity of its dissolution products [14]. Moreover, the alkaline environment formed by the dissolution products of the sodium silicate and composite specimens decreases in pH as the SBF is exchanged, indicating that the local alkaline effect is limited and is likely to be buffered *in vivo* [15].

Viability of *in vitro* specimens was confirmed with bioactive glass disc monoliths, as mineralisation is visible to the naked eye on 0.5 µm-polished surfaces. The results of the viability screening tests are presented in Appendix III.

4.6.2 Scanning Electron Microscopy with Energy-dispersive X-ray Spectroscopy

SEM with EDX was used to monitor the progression of mineralisation and other surface changes of *in vitro* specimens. SEM micrographs in Figure 4-21 show the progression of surface morphological changes with increasing immersion time, and the effect of composition on the size and morphology of surface features.

Sodium silicate control specimens were not observed to mineralise at any immersion time. However, the binder phase of each composition, which was comprised of sodium silicate in contact with bioactive glass frit, was found to mineralise at every observed immersion time. This mineralisation indicates that either the composition of the binder phase changed as a result of its combination with the bioactive glass frit, in such a way as to allow it to form calcium phosphate minerals in SBF, or that mineralisation was able to nucleate on the bioactive glass through the binder phase layer. This phenomenon is further explored in Chapter 4.6.2.1.



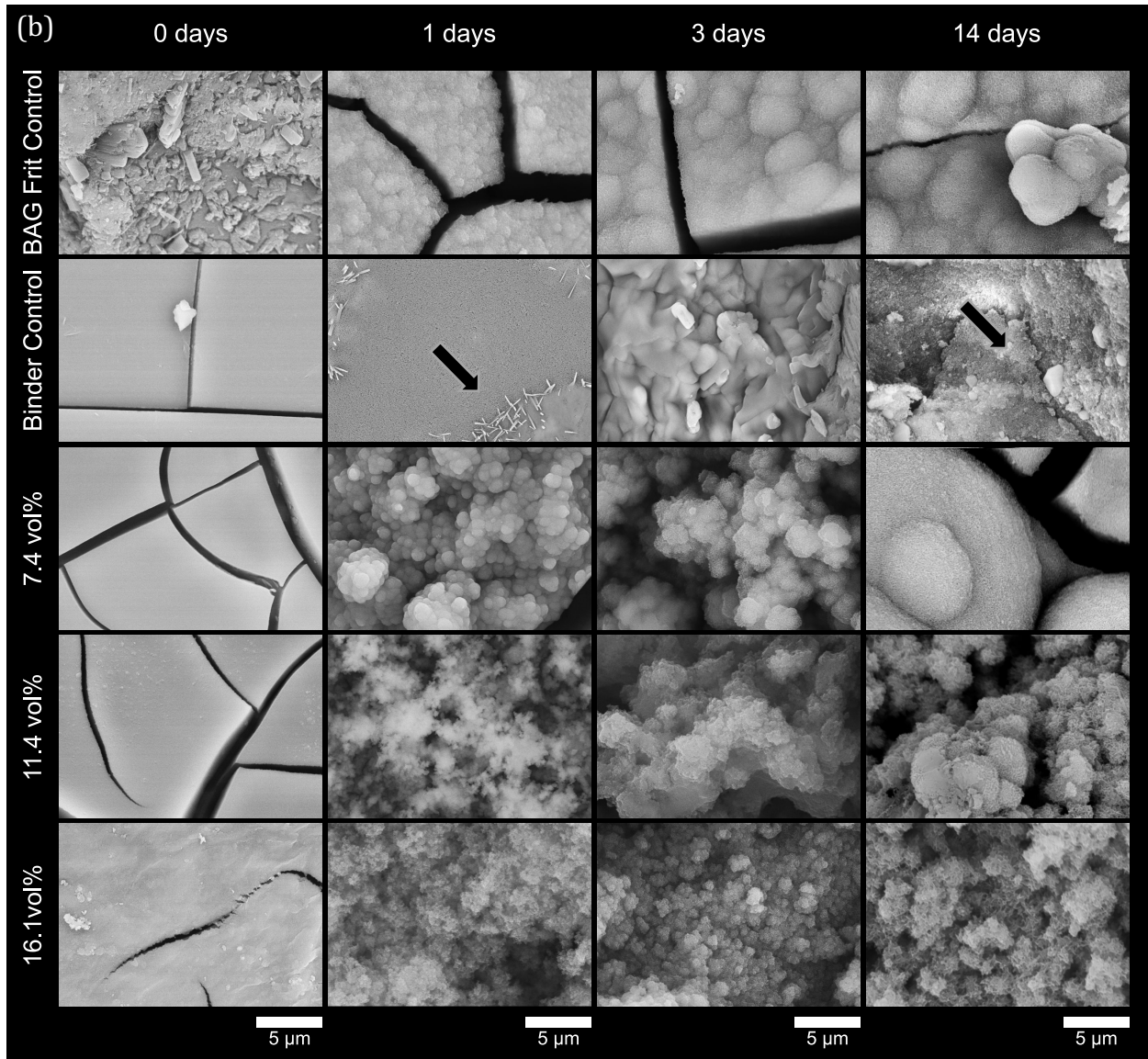


Figure 4-21. SEM BSE micrographs of *in vitro* specimens at 0, 1, 3, and 14 days immersion, at (a) low magnification and (b) high magnification. Surface mineralisation is shown to increase with increasing immersion time and is inversely related to amount of binder. Though a gel formed, the sodium silicate control (binder) did not mineralise despite roughened appearance; see black arrows sodium binder control images indicating deposition of crystalline SBF salts (confirmed with XRD analysis, Chapter 4.6.3). However, sodium silicate binder phase layers in composite specimens did mineralise. Adapted from Guzzo and Nychka, 2020 [9].

EDX confirmed that no calcium phosphate mineralisation occurred on the sodium silicate control specimen, as evidenced by the absence of calcium and phosphorous in Figure 4-22. EDX was also used to verify the elemental constituents of surface features, with calcium

phosphate nuclei displaying characteristically high calcium and phosphorous content. Though common in many studies, Ca/P ratios were not used to identify the type of calcium phosphate formed, as the interaction volume of EDX was larger than the thickness of the mineralised surface layer. Mineral phase identification was carried out with XRD and FTIR analysis (Chapters 4.6.3 and 4.6.4, respectively).

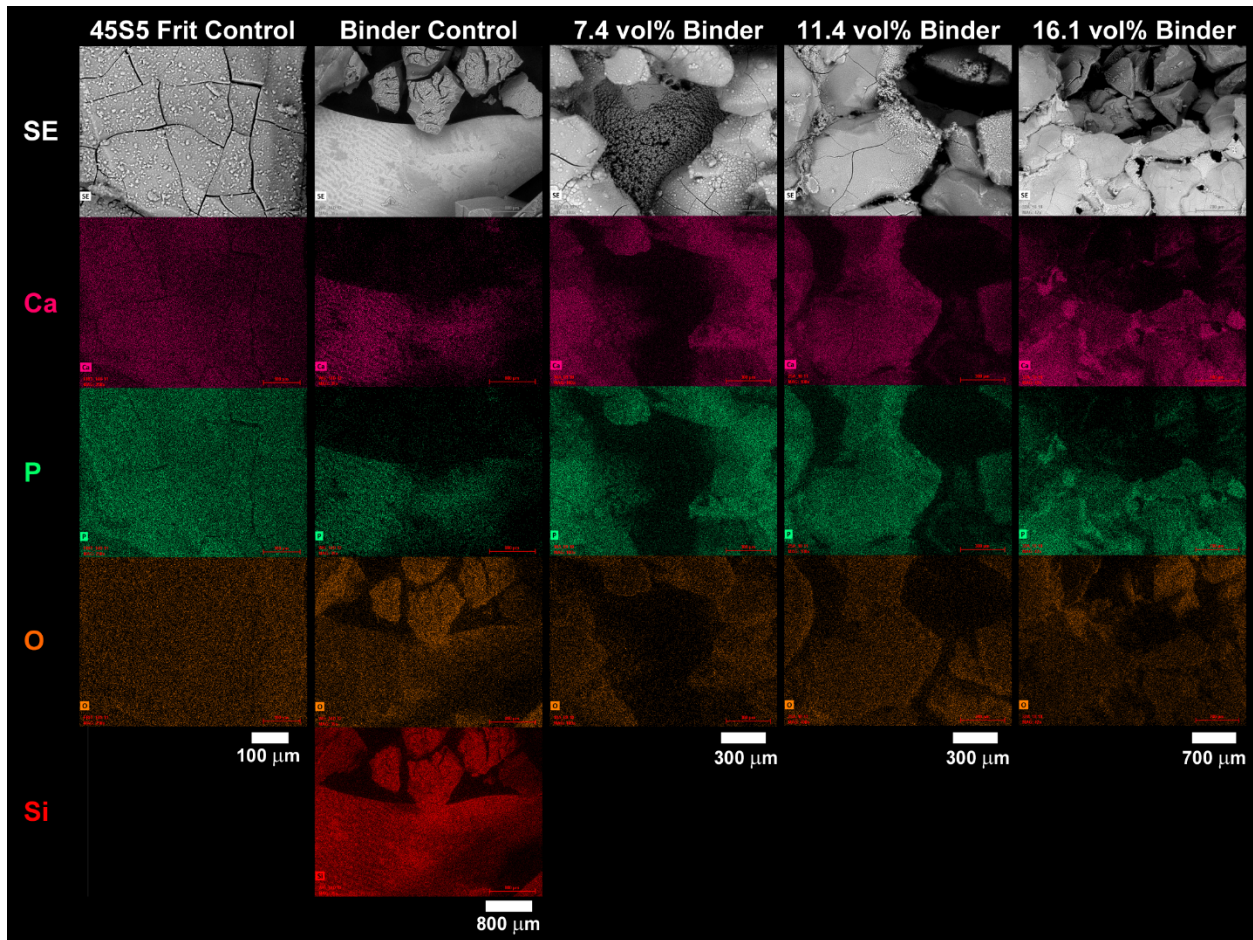


Figure 4-22. SEM-EDX element maps for the various controls and scaffolds after 14 days immersion in SBF. The co-location of Ca and P is an indicator of mineralisation of the surfaces of frit, and binder necks on scaffolds. Of note: no mineralisation (Ca and P) was observed on the binder control specimen—the binder becomes bioactive only when used in conjunction with the bioactive glass frit, likely due to reaction with the bioactive glass particles during setting. The most intense signals of Ca and P occurred on the highest binder scaffold (16.1 vol%) at the binder neck regions [9].

All compositions of composite specimens were found to mineralise *in vitro*, with the rates of nucleation and growth inversely proportional to amount of binder phase. Mineral surface features were observed to be arranged hierarchically (Figure 4-23), with the first-level (1st) and second-level (2nd) structures observed to have opposite relationships with the amount of binder phase. The larger, first-level structures decreased in size with increasing binder phase amount, and the lath or needle-like second-level structures increased in size with increasing binder phase amount. The size of the larger hierarchical structures for each composition is listed in Table 4-10. The surface features formed on the 7.4 vol% specimens are markedly similar to the bioactive glass control specimens, in both form and size; in contrast, the surface features of the 11.4 and 16.1 vol% specimens are most similar to one another. This pattern of *in vitro* behaviour is shown schematically in Figure 4-24.

This pattern is likely due to the surface coverage of the binder phase on the bioactive glass frit; specimens with 7.4 vol% have incomplete wet-out of the binder phase once set, exposing regions that are effectively only bioactive glass. This incomplete coverage is not seen in 11.4 vol% or 16.1 vol% specimens, in which every observed piece of frit is conformally coated in binder phase (Figure 4-25). The binder wet-out threshold is between 7.4 and 11.4 vol% set binder, and this threshold effect contributes to the similarities between 7.4 vol% specimens and the bioactive glass control, and the differences between 7.4 vol% and higher binder phase specimens.

	1 st -level structures (µm)		2 nd -level structures (µm)	
	Average	Standard Deviation	Average	Standard Deviation
Bioactive glass control	3.87	1.34	0.045	0.013
7.4 vol%	8.27	5.68	0.054	0.010
11.4 vol%	1.00	0.57	0.060	0.021
16.1 vol%	0.84	0.22	0.099	0.042

Table 4-10. Size of hierarchical surface features on 14 day *in vitro* specimens as a function of composition. First-level structures were measured for diameter, while second-level structures were measured for width [9].

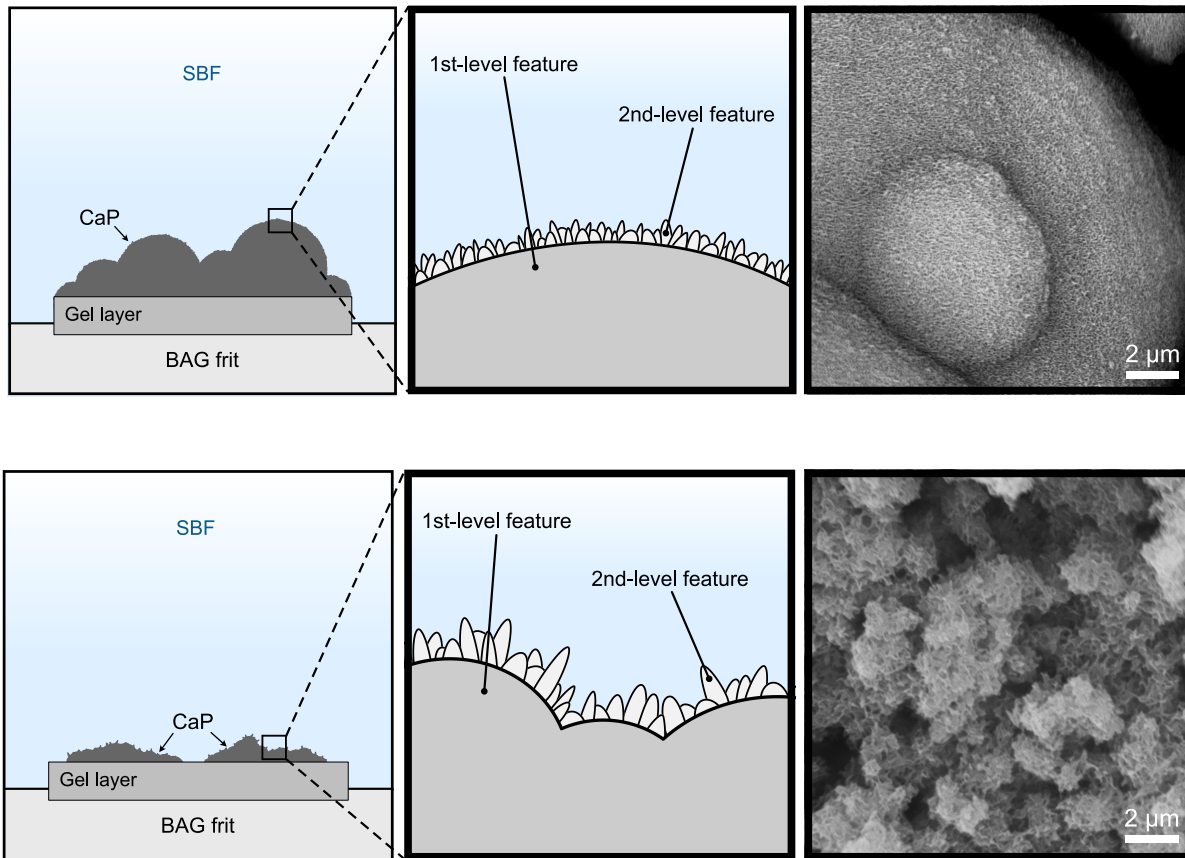


Figure 4-23. Schematic representation of the hierarchical structure of surface minerals as a function of binder phase, showing (a) low-binder composites and (b) high-binder composites after 14 days *in vitro* immersion. 1st-level features decrease in size with increasing binder phase, while 2nd-level features increase in size with increasing binder phase [9].

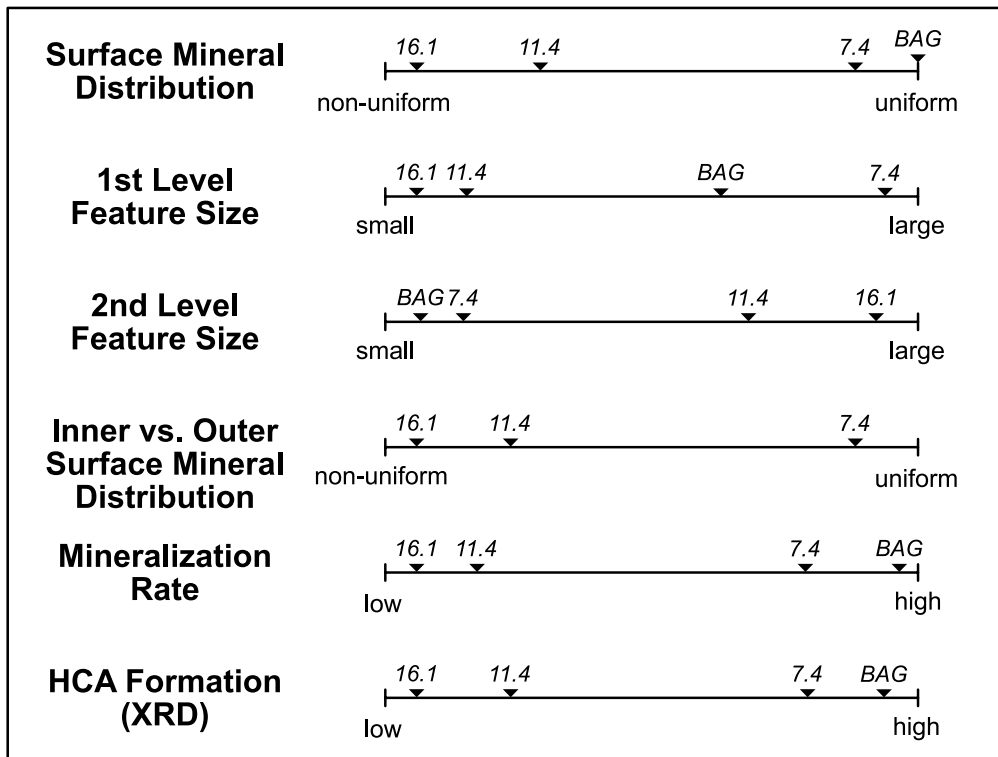


Figure 4-24. Schematic depiction of composite specimen *in vitro* behaviour. 7.4, 11.4, and 16.1 indicate the vol% of binder phase in each specimen composition; 'BAG' denotes bioactive glass control specimens. 7.4 and BAG specimens behave most similarly, while 11.4 and 16.1 specimens have distinctly different *in vitro* behaviour. Sodium silicate control specimens did not mineralise *in vitro* and thus are not included [9].

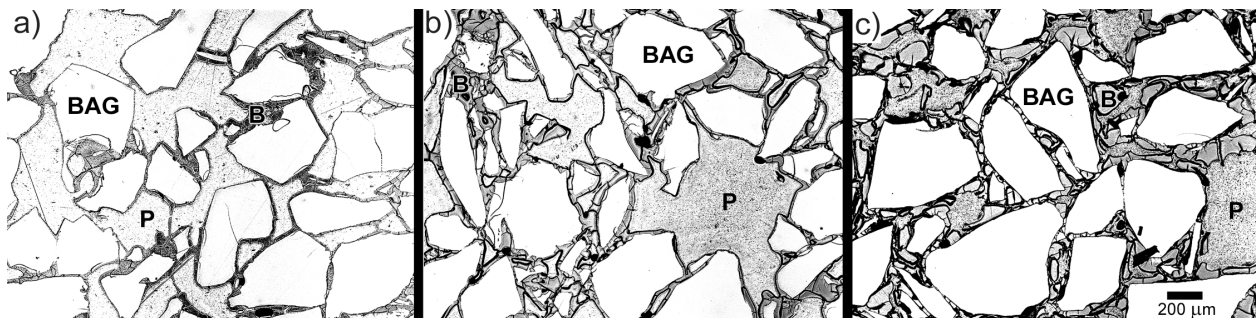


Figure 4-25. Bright-field OLM micrographs of (a) 7.4, (b) 11.4, and (c) 16.1 vol% binder phase specimens. Note the incomplete wet-out of the binder phase in specimen (a), with effectively complete coverage of bioactive glass frit in specimens (b) and (c). 'BAG' denotes bioactive glass frit particles, 'B' denotes binder phase, and 'P' denotes pores [9].

Surface minerals were predominantly composed of amorphous calcium phosphate (ACP), with evidence of crystalline species octacalcium phosphate (OCP) and hydroxycarbonate apatite (HCA) forming with increasing *in vitro* immersion time (from XRD and FTIR analysis, further explored in Chapters 4.6.3 and 4.6.4). The distribution and dispersion of surface mineralisation was found to be correlated with specimen composition. Surface mineral distribution displayed the same pattern described in Figure 4-24, wherein bioactive glass controls and 7.4 vol% specimens showed similar behaviour, and 11.4 vol% and 16.1 vol% specimens showed a different behaviour pattern. After 14 days of *in vitro* immersion, calcium phosphate nuclei formed continuously over the surface of bioactive glass controls and 7.4 vol% specimens, and in discrete clusters on 11.4 and 16.1 vol% specimens. The discrete mineral clusters on the latter two compositions were preferentially located on binder necks between bioactive glass frit particles, further indicating a compositional change in the binder phase during fabrication. This behaviour is further explored in Chapter 4.6.2.1.

Increasing the amount of binder phase appeared to impede mineral formation throughout the entire volume of the composites, but did not prevent it. The external surfaces of higher-binder phase compositions were observed to have higher amounts of mineralisation when compared to internal surfaces (Figure 4-26). This gradient was likely due to the hydrated binder swelling and forming a mass transport barrier, inhibiting ions from accessing the interior surfaces of the scaffold as readily as the external surfaces (pore-blocking). Compositions with higher amounts of binder phase would thus have larger barriers, resulting in the markedly reduced *internal* mineralisation. This phenomenon is illustrated schematically in Figure 4-27.

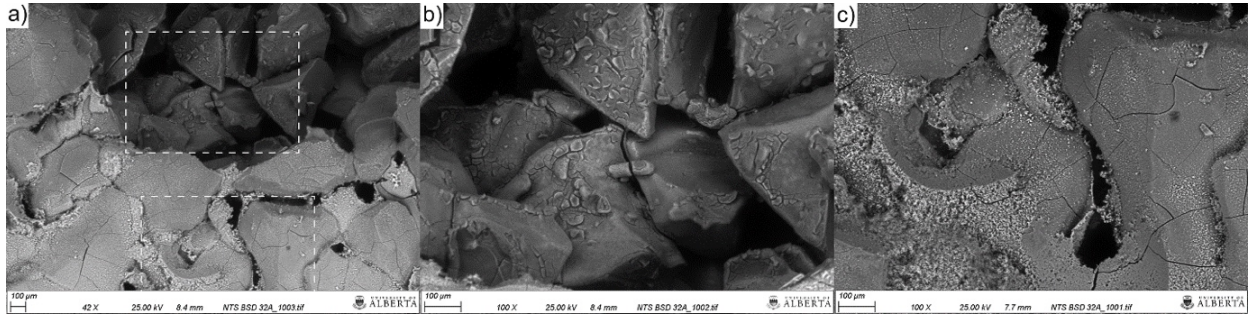


Figure 4-26. a) BSE SEM micrograph of a 16.1 vol% binder phase specimen after 14 days of *in vitro* immersion, depicting the difference in mineralisation between the (b) inner and (c) outer specimen surfaces. Dashed lines in a) represent regions of interest in b) and c). EDX mapping of calcium and phosphorous of both surfaces can be seen in Figure 4-22; while mineralisation has occurred on both surfaces, considerably higher quantities of calcium phosphate species have formed on the outer surface [9].

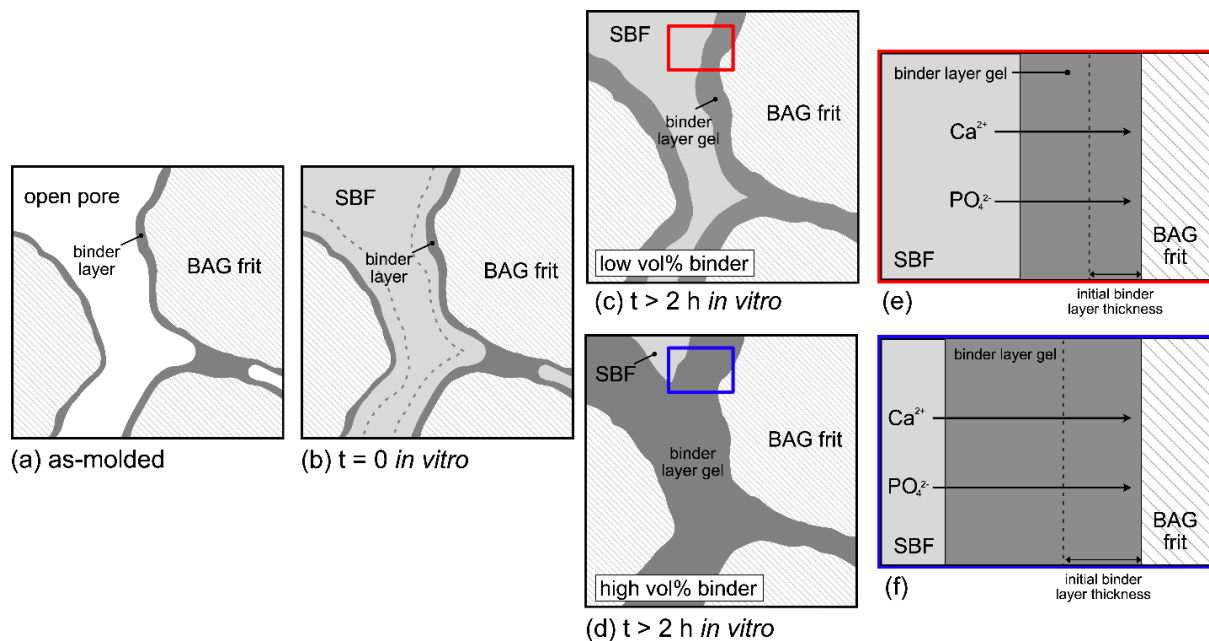


Figure 4-27. Schematic of *in vitro* swelling of composite binder phase, shown (a) as-moulded, before immersion; (b) immediately upon immersion, before hydration and swelling of the binder layer; and after swelling takes place in (c) low-binder and (d) high-binder composites. Insets show the path length difference for ion diffusion in (e) low-binder and (f) high-binder composites; the longer path length for ion diffusion in higher-binder compositions may impede mineralisation, particularly on inner surfaces, and the pore-blocking in high vol% binder composites also limited continued access of the internal structure to SBF [9].

4.6.2.1 *in vitro* Gel Formation

Evidence of two discrete gel layers was identified on high vol% binder composite scaffolds following *in vitro* immersion (Figure 4-28). 45S5 bioactive glass is known to form a hydrated silica gel layer *in vitro*, from which amorphous calcium phosphate forms, which is a precursor to the eventual crystallisation of hydroxyapatite [16]. The formation of this hydrated silica gel is evident on the bioactive glass control specimens, which display characteristic cracking from the dried gel layer. The other gel layer seen on the composite specimens (Figure 4-28b-c) is most likely the binder phase, which also forms a hydrated gel *in vitro*, and would display similar shrinkage cracks after drying.

It is important to note that while the sodium silicate control specimen was not observed to form any calcium phosphate, both gel layers on the composite specimens were found to form calcium phosphate. Additionally, calcium phosphate was found to preferentially nucleate on the binder necks of higher binder phase specimens. This location-specific nucleation is indicative of either (a) nucleation from the bioactive glass frit through the binder layer, or (b) a chemical change in the binder phase due to its interaction with the bioactive glass. Two possible scenarios have been identified for when a compositional change may have occurred:

1. This change occurred during fabrication—there is evidence of a reaction between the binder phase and the bioactive glass in as-processed composite specimens (Figure 4-29). The high pH of the aqueous sodium silicate (11.4) may have etched the bioactive glass, partially dissolving the silicate network and allowing ions from the bioactive glass to enter the sodium silicate gel network.

The preferential nucleation of calcium phosphate minerals on the binder necks of 16.1 vol% specimens (Figure 4-26) provides further evidence that a compositional change occurred during fabrication. Specimens with higher amounts of binder phase have more interfacial surface area for the etching reaction to occur (due to complete wet-out), as well as more material available to react. Additionally, the high Laplace pressure of the binder necks, which are on the order of microns, may locally increase the driving force for etching reactions [17].

- The compositional change may have occurred *in vitro*, as the two gel layers may have allowed for ion diffusion between the bioactive glass and binder phase. Ca^{2+} and PO_4^{3-} ions are able to migrate through the silica gel layer formed by bioactive glass [18], and ions from SBF were found to migrate into the sodium silicate gel matrix (via XRD analysis; Chapter 4.6.3). Thus, it follows that ions from the bioactive glass may be able to diffuse through the gel layers and alter the composition of the binder phase gel.

Additionally, compositional changes of the binder phase may have occurred simultaneously in both scenarios described above.

When composite specimens are immersed *in vitro*, a compositional change of the binder phase may result in the formation of either (i) one mixed gel, (ii) two discrete gels, which may or may not have an intermediate layer between them. These situations are shown schematically in Figure 4-28, with SEM micrographs depicting evidence for each mechanism.

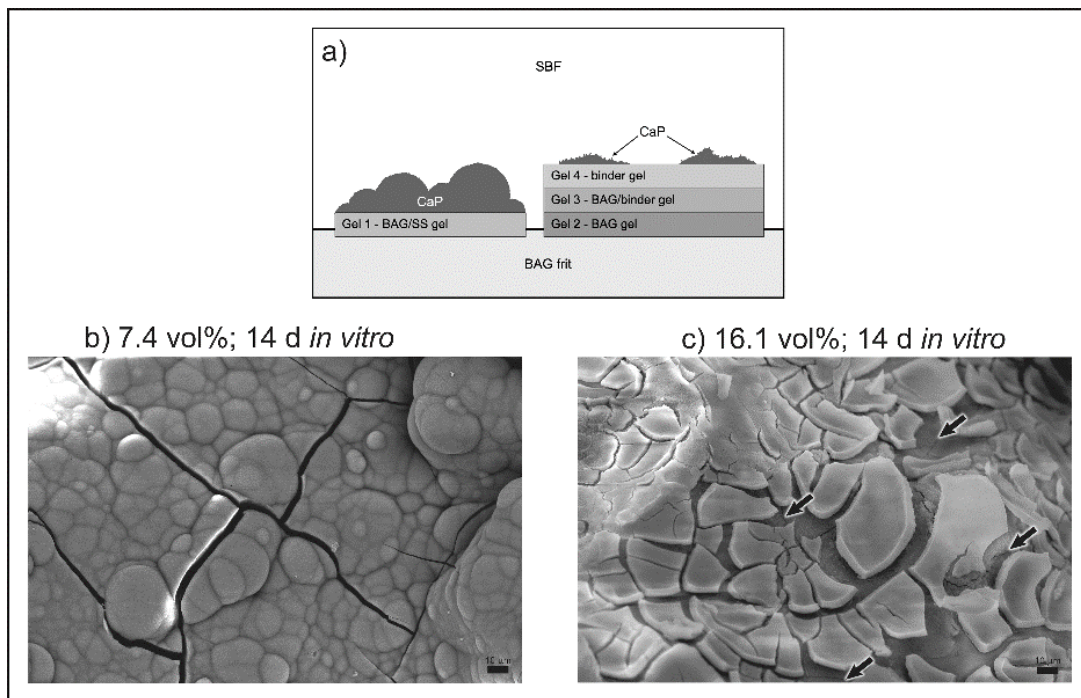


Figure 4-28. (a) Schematic depiction of possible gel formation mechanisms of composite specimens *in vitro*. Bioactive glass is denoted as ‘BAG’; calcium phosphate minerals are denoted as ‘CaP’. BSE SEM micrographs depict (b) single gel layer formation and (c) multiple gel layer formation. Due to intra-specimen variability, both phenomena may occur in different regions of a single specimen. Single gel formation was observed more often in lower binder phase compositions, while multiple gel formation was found on higher binder phase compositions. Arrows in (c) indicate where two distinct cracked gel layers are layered atop one another [9].

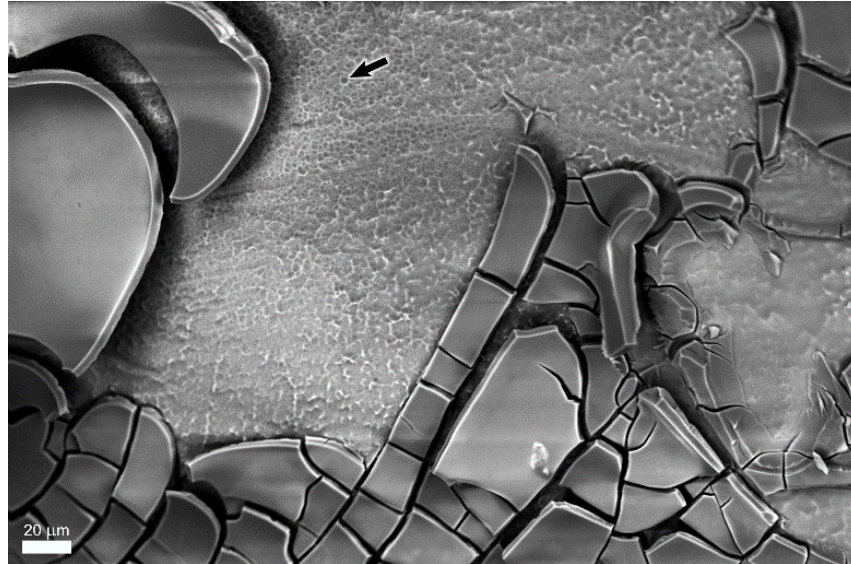


Figure 4-29. BSE SEM micrograph of a 45S5 glass frit particle within a 11.4 vol% binder composite scaffold specimen as manufactured. The pitting (black arrow) on the roughened surface of the frit indicates that the application of the high pH binder phase precursor has resulted in chemical attack of the glass frit, and effectively etched the surface. The appearance of etching provides further evidence for the possibility of an intermediate gel layer when sufficient amounts of binder phase are present [9].

4.6.3 X-ray Diffractometry

XRD analysis of composite and control specimens confirmed the relationships identified in SEM/EDX analysis; amount of OCP (PDF#01-074-1301) and HCA (PDF#01-072-9861) mineralisation decreased with increasing binder phase, and no evidence of calcium phosphate mineralisation was found for sodium silicate controls (Figure 4-30a). The rate of mineralisation was again found to be inversely proportional to binder phase; HCA signals at $2\theta = 31.5^\circ$ ($(hkl) = (1\ 2\ 1)$) decreased in magnitude with increasing binder phase. Evidence of HCA was detected in the composites after 14 days *in vitro* immersion, while HCA peaks were detected after 3 days in the bioactive glass frit control. Due to the nanocrystalline nature of *in vitro* HCA, XRD peaks are broader than well-ordered crystalline HCA [19]. HCA is a precursor of hydroxyapatite, which may also be present; HA peaks (PDF#01-096-0740) overlap with HCA peaks and thus are indistinguishable. However, distinct evidence of HCA mineralisation was observed in FTIR analysis (Figure 4-30a; Chapter 4.6.4).

Evidence of OCP mineralisation was found at varying time points for each composite specimen and bioactive glass control; as OCP is a precursor to HCA formation, it may continuously form from ACP while simultaneously being consumed to form HCA during *in vitro* immersion [20].

XRD patterns of *in vitro* sodium silicate control specimens clearly show halite (NaCl; PDF#00-005-0628), providing additional evidence that ions from SBF enter the hydrated sodium silicate gel network upon immersion. Ion transport through the binder phase gel network is necessary for mineralisation of conformally coated composite specimens. Additionally, amorphous cristobalite (SiO₂; PDF#00-004-0379) increases with increasing immersion time—sodium silicate gels have been reported to form cristobalite [6], with cristobalite formation theorised to be limited by the rigidity of the set gel. When hydrated with SBF and held at an elevated temperature, sodium silicate may have a lowered mass transport barrier and increased driving force for the formation of cristobalite.

4.6.4 Fourier Transform Infrared Spectroscopy

To validate the phase identification of *in vitro* mineral formation, FTIR was used to characterise changes in characteristic bonds. Spectra obtained from bioactive glass control specimens were observed to display the expected P–O bending peaks at 560 and 604 cm⁻¹, as well as P–O stretching at 1100 cm⁻¹ [21, 22, 19] (Figure 4-30b). The intensities of these peaks increased with increasing immersion time, confirming the increased formation of HCA surface minerals. Additionally, C–O stretching at 870 cm⁻¹ increases with increasing immersion time, indicative of HCA formation [22]. The Si–O stretching peak at 926 cm⁻¹ [23] decreased with increasing immersion time, likely indicating the dissolution of the glass silicate network as the bioactive glass begins to dissolve *in vitro*. Si–O bending at 470 cm⁻¹ and Si–O stretching at 1040 cm⁻¹ [24, 22] were present at all observed time points and did not undergo marked changes in intensity.

Composite specimens were found to produce similar FTIR spectra as the bioactive glass control, but with considerably less distinct formation of P–O and C–O peaks (Figure

4-30b). This difference is attributable to the macro-scale intra-sample variability; FTIR samples comprised less than 5% of the total volume of a single *in vitro* specimen. The nature of the composite scaffold is such that the composition and *in vitro* mineralisation behaviour varies considerably over a single specimen, as shown with SEM-EDX in Chapter 4.6.2. A sample taken from the specimen may be from a region containing very little surface mineralisation, or of dense mineralisation. Moreover, a FTIR sample taken from the specimen may contain varying amounts of either constituent. In contrast to XRD samples, FTIR samples were not crushed or homogenised prior to analysis, accounting for the difference in variability between the two techniques.

FTIR spectra of sodium silicate control specimens show the appearance of a peak at 801 cm^{-1} that increases in intensity with increasing immersion time (Figure 4-30b). This peak can be attributed to Si–O stretching of cristobalite [25, 26, 27], which is absent in the 0 day control specimen. At each observed time point, Si–O peaks are present at 470, 1065, and 1230 cm^{-1} , which is attributable to multiple SiO_2 polymorphs, including amorphous silica and cristobalite [28, 29]. The increasing formation of cristobalite with increasing immersion time confirms the aforementioned XRD results.

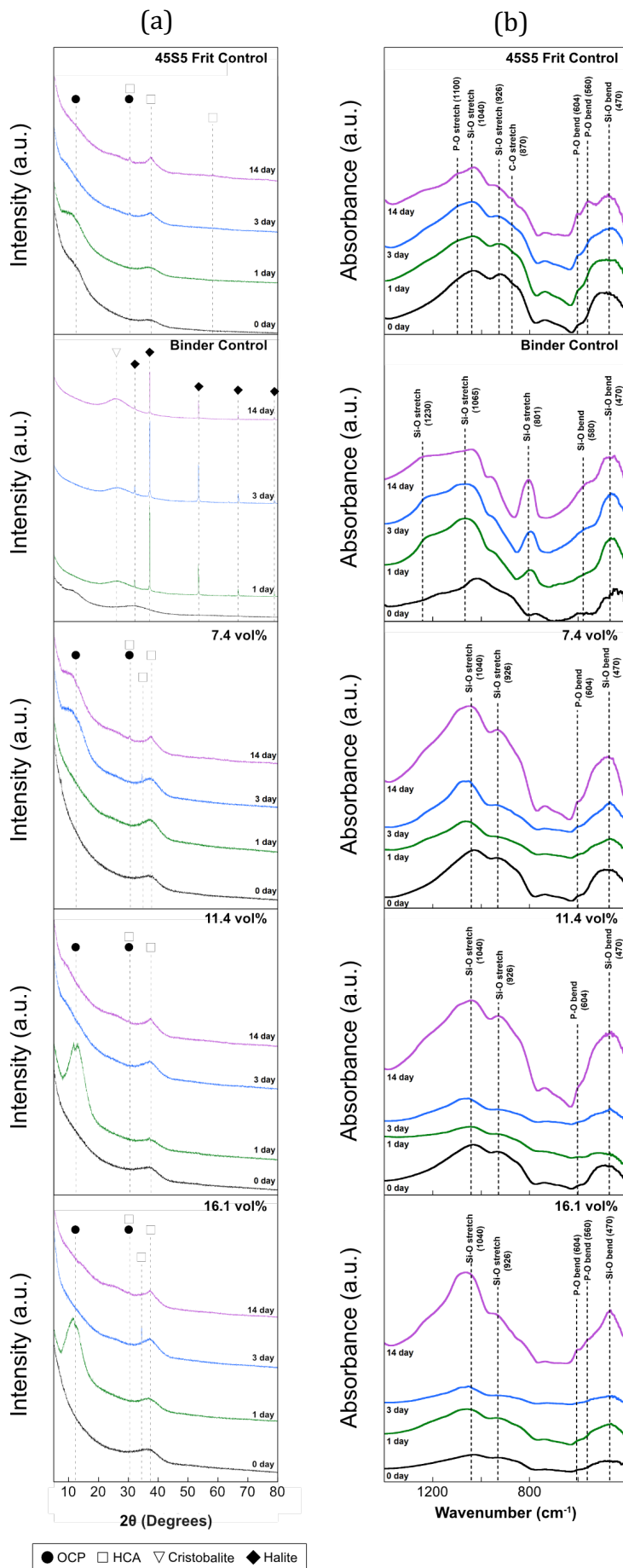


Figure 4-30. a) XRD patterns of *in vitro* specimens. The 45S5 frit control and composite scaffolds exhibit similar trends in formation of octacalcium phosphate (OCP) and hydroxycarbonate apatite (HCA) over immersion times. The binder control forms cristobalite and has impurity halite as a result of incorporation of SBF salts. b) FTIR spectra of *in vitro* specimens illustrating chemical changes and surface mineralisation. The 45S5 frit control and composite scaffolds show similar formation of P–O bonds associated with HCA mineral formation. Sodium silicate controls demonstrated the formation of characteristic Si–O peaks associated with the formation of cristobalite. Adapted from Guzzo and Nychka, 2020 [9].

4.7 Resorbability

The main constituent of the composite scaffolds, 45S5 bioactive glass, has been shown to be resorbable with extensive *in vivo* studies and clinical applications [30, 11, 10, 31, 32]. The *in vitro* gel formation (recall Chapter 4.5.2.1, Figure 4-28c) and biomineralisation of the bioactive glass frit within the composite scaffolds is indicative that the presence of a sodium silicate binder phase will not prevent resorption; the SBF infiltration necessary to produce gel formation and mineralisation is also required to initiate resorption [33, 34]. Future *in vivo* studies are necessary to investigate the effect of cell interaction and new bone growth on scaffold resorbability.

Sodium silicate has also been shown to be moderately resorbable in biomedical implants, albeit only *in vitro* and with far fewer studies than those for 45S5 bioactive glass [35, 36]. The gels formed *in vitro* by sodium silicate control specimens and the binder phase of composite scaffolds (recall Figure 4-19) are in agreement with gels observed to be water soluble in saline environments [13]. This solubility in aqueous environments is promising, as it may indicate *in vivo* resorbability; however, further evaluation of the degradation products and their potential cytotoxicity is required.

Throughout the 14 day *in vitro* immersion, all evaluated scaffold compositions maintained geometric stability sufficient to permit handling, indicative of sufficient stability to remain in a bone defect without material migration.

Ultimately, *in vivo* studies are necessary to accurately assess the resorbability of the composite as a whole. This future work is detailed in Chapter 5.2, along with other investigations that have the potential to further the clinical success and viability of this formable, *in situ*-setting, porous bone scaffold material.

Bibliography – Chapter Four

- [1] ISO, “ISO 23145-1 - Fine ceramics (advanced ceramics, advanced technical ceramics) — Determination of bulk density of ceramic powders — Part 1: Tap density - First Edition,” ISO - International Organization for Standardization, Geneva, Switzerland, 2007.
- [2] E. P. Cox, “A Method of Assigning Numerical and Percentage Values to the Degree of Roundness of Sand Grains,” *Journal of Paleontology*, vol. 1, no. 3, pp. 179-183, 1927.
- [3] K. Miura, K. Maeda, M. Furukawa and S. Toki, “Mechanical characteristics of sands with different primary properties,” *Soils and Foundations*, vol. 38, no. 4, pp. 159-172, 1998.
- [4] M. Cubrinovski and K. Ishihara, “Maximum and minimum void ratio characteristics of sands,” *Soils and Foundations*, vol. 42, no. 6, pp. 65-78, 2002.
- [5] X. Jia and R. A. Williams, “A packing algorithm for particles of arbitrary shapes,” *Powder Technology*, vol. 120, pp. 175-186, 2001.
- [6] D. V. Atterton, “The carbon-dioxide process,” *AFS Transactions*, vol. 64, pp. 14-18, 1956.
- [7] C. M. Guzzo and J. A. Nychka, “Fabrication of a Porous and Formable Ceramic Composite Bone Tissue Scaffold at Ambient Temperature,” *Metallurgical and Materials Transactions A*, Under Review, 2020.
- [8] Flexbar Machine Corporation, *Reprorubber Brochure REP-0409*, Islandia, NY: Flexbar Machine Corporation, 2017.
- [9] C. M. Guzzo and J. A. Nychka, “In vitro response of a porous and formable ceramic composite bone tissue scaffold,” *Journal of the Mechanical Behaviour of Biological Materials*, Under Review, 2020.
- [10] F. Baino, G. Novajra and C. Vitale-Brovarone, “Bioceramics and scaffolds: A winning combination for tissue engineering,” *Frontiers in Bioengineering and Biotechnology*, vol. 3, pp. 1-17, 2015.
- [11] L. Gerhardt and A. Boccaccini, “Bioactive glass and glass-ceramic scaffolds for bone tissue engineering,” *Materials*, vol. 3, pp. 3867-3910, 2010.
- [12] C. J. McMahon, “Chapter 16: Rigid Connective Tissue: Bone,” in *Structural Materials: A Textbook with Animations*, Philadelphia, PA: Merion Books, 2004, pp. 407-414.

- [13] M. T. Tognonvi, S. Rossignol and J. P. Bonnet, "Physical-chemistry of sodium silicate gelation in an alkaline medium," *Journal of Sol-Gel Science and Technology*, vol. 58, no. 3, pp. 625-635, 2011.
- [14] S. Hu, J. Chang, M. Liu and C. Ning, "Study on antibacterial effect of 45S5 Bioglass," *Journal of Materials Science: Materials in Medicine*, vol. 20, no. 1, pp. 281-6, 2009.
- [15] F. E. Ciraldo, E. Boccardi, V. Melli, F. Westhauser and A. R. Boccaccini, "Tackling bioactive glass excessive in vitro bioreactivity: Preconditioning approaches for cell culture tests," *Acta Biomaterialia*, vol. 75, pp. 3-10, 2018.
- [16] A. Lotsari, A. K. Rajasekharan, M. Halvarsson and M. Andersson, "Transformation of amorphous calcium phosphate to bone-like apatite," *Nature Communications*, vol. 9, no. 1, 2018.
- [17] Seville, J. Wu and Chuan-Yu, "8.4 Interaction of Particles with Liquid Bridges," in *Particle Technology and Engineering--An Engineer's Guide to Particles and Powders--Fundamentals and Computational Approaches*, Elsevier, 2016.
- [18] L. L. Hench, D. L. Wheeler and D. C. Greenspan, "Molecular control of bioactivity in sol-gel glasses," *J. Sol-Gel Sci Technol*, vol. 13, no. 1-3, pp. 245-250, 1998.
- [19] Y. Yu, Z. Bacsik and M. Eden, "Contrasting in vitro apatite growth from bioactive glass surfaces with that of spontaneous precipitation," *Materials*, vol. 11, no. p, pp. 20-22, 2018.
- [20] J. R. Jones, "Review of bioactive glass: From Hench to hybrids," *Acta Biomaterialia*, vol. 9, pp. 4457-4486, 2013.
- [21] I. Notingher and et al., "Application of FTIR and Raman spectroscopy to characterisation of bioactive materials and living cells," *Spectroscopy*, vol. 17, no. 2-3, pp. 275-288, 2003.
- [22] O. P. Filho, G. P. Latorre and L. L. Hench, "Effect of crystallization on apatite-layer formation of bioactive glass 45S5," *J Biomed Mater Res*, vol. 30, no. 4, pp. 509-514, 1996.
- [23] H. Aguiar, J. Serra, P. Gonzalez and B. Leon, "Structural study of sol-gel silicate glasses by IR and Raman spectroscopies," *J Non-Cryst Sol*, vol. 355, pp. 475-480, 2009.
- [24] G. S. Pappas, P. Liatsi, I. A. Kartsonakis, I. Danilidis and G. Kordas, "Synthesis and characterization of new SiO₂-CaO hollow nanospheres by sol-gel method: bioactivity of the new system," *J Non Cryst Sol*, vol. 354, no. 2-9, pp. 755-760, 2008.
- [25] H. -H. Fricke, M. Mattenklott, H. Parlar, A. Hartwig and MAK Commission, "Method for the determination of quartz and cristobalite (Air Monitoring Methods, 2015)," in *The MAK-Collection for Occupational Health and Safety: Annual Thresholds and Classifications for the Workplace*, Heidelberg, Wiley-Verlag GmbH & Co. KGaA, 2016.

- [26] E. R. Lippincott, A. Vancalkeburg, C. E. Weir and E. N. Bunting, "Infrared studies on polymorphs of silicon dioxide and germanium dioxide," *J Res Natl Bur Stand (1934)*, vol. 61, no. 1, p. 61, 1958.
- [27] S. H. Xue, H. Xie, H. Ping, Q. C. Li, B. L. Su and Z. Y. Fu, "Induces transformation of amorphous silica to cristobalite on bacterial surfaces," *RSC Adv*, vol. 5, no. 88, pp. 71844-71848, 2015.
- [28] J. R. Michalski, M. D. Kraft, T. Diecrich, T. G. Sharp and P. R. Christensen, "Thermal emission spectroscopy of the silica polymorphs and considerations for remote sensing on Mars," *Geophys Res Lett*, vol. 40, no. 19, 2003.
- [29] P. J. Launer and B. Arkles, "Infrared analysis of organosilicon compounds," in *Silicon Compounds: Silanes and Silicones, 3rd Ed.*, Morrisville, Gelest, Inc., 2013, pp. 175-178.
- [30] L. L. Hench, D. E. Day, W. Höland and V. M. Rheinberger, "Glass and Medicine," *International Journal of Applied Glass Science*, vol. 1, no. 1, pp. 104-117, 2010.
- [31] H. Qu, H. Fu, Z. Han and Y. Sun, "Biomaterials for bone tissue engineering scaffolds: A review," *RSC Advances*, vol. 9, no. 45, pp. 26252-26262, 2019.
- [32] Q. Chen, J. Roether and A. Boccaccini, "Tissue Engineering Scaffolds from Bioactive Glass and Composite Materials," *Topics in Tissue Engineering*, vol. 4, no. 6, pp. 1-27, 2008.
- [33] A. R. Boccaccini, Q. Chen, L. Lefebvre, L. Gremillard and J. Chevalier, "Sintering, crystallisation and biodegradation behaviour of Bioglass-derived glass-ceramics," *Faraday Discussions*, vol. 136, pp. 27-44, 2007.
- [34] J. A. Sanz-Herrera and A. R. Boccaccini, "Modelling bioactivity and degradation of bioactive glass based tissue engineering scaffolds," *International Journal of Solids and Structures*, vol. 48, no. 2, pp. 257-268, 2011.
- [35] Z. Huan and J. Chang, "Effect of sodium carbonate solution on self-setting properties of tricalcium silicate bone cement," *Journal of Biomaterials Applications*, vol. 23, no. 3, pp. 247-262, 2008.
- [36] Z. Huan and J. Chang, "Calcium-phosphate-silicate composite bone cement: self-setting properties and in vitro bioactivity.," *Journal of Materials Science: Materials in Medicine*, vol. 20, no. 4, pp. 833-841, 2009.
- [37] O. Borkiewicz, J. Rakovan and C. L. Cahill, "Time-resolved in situ studies of apatite formation in aqueous solutions," *American Mineralogist*, vol. 95, pp. 1224-1236, 2010.

Chapter Five

Conclusions and Future Work¹

5.1 Conclusions

In this thesis, an ambient temperature method for the fabrication of porous and formable all-ceramic composite material was explored to produce *in situ*-castable, wound-customisable bone tissue scaffolds. This composite material was evaluated in the context of established design criteria, namely: formability, geometric stability, porosity, load-bearing capacity, bioactivity, and resorbability. The method under development used existing materials to produce a formable paste that set in ambient conditions with geometric stability, and the resultant compacts were found to possess uniformly distributed open porous networks. Mechanical testing of the ceramic composites revealed sufficient compressive strength to permit handling, on the order of trabecular bone. The *in vitro* behaviour of the scaffolds was assessed to ascertain bioactivity; every investigated composite composition was observed to mineralise *in vitro*, forming amorphous calcium phosphate and hydroxycarbonate apatite. The rate and extent of mineralisation indicate that the composites exhibit Class A bioactivity [1]. The amount of binder inversely correlated with the amount of open porosity, positively correlated with compressive strength, and inversely correlated to the amount and uniformity of *in vitro* mineralisation.

In summary, a liquid silicate precursor can be combined with bioactive glass frit to produce a formable, geometrically stable, open porous scaffold with load-bearing capacity and an *in vitro* response indicative of Class A bioactivity and resorbability. This fabrication method circumvents the limitations of traditional ceramic processing techniques, creating

¹ Portions of this chapter have been submitted for publication in Metallurgical and Materials Transaction A: C. M. Guzzo and J. A. Nychka, "Fabrication of a Porous and Formable Ceramic Composite Bone Tissue Scaffold at Ambient Temperature," Under Review, submitted 12-01-2019; Journal of the Mechanical Behaviour of Biomedical Materials: C. M. Guzzo and J. A. Nychka, "In vitro response of a porous and formable ceramic composite bone tissue scaffold," Under Review, submitted 02-01-2020.

an interconnected porous network without thermal consolidation, and producing a truly conformal scaffold without additional surgeries, equipment, or infrastructure.

The conclusions of this research are as follows:

- 1) Fabrication of porous ceramic composites is possible (at ambient temperature) with established materials without the use of high temperature for powder consolidation:
 - a. The resultant paste was found to be formable as measured by sufficiently long manipulation times to mix, mould, and compact the unset paste into a variety of geometries;
 - b. The resultant set composites attained geometric stability as measured by ability to de-mould set composites, handle the set geometries, and through dimensional comparison/contrast to axisymmetric geometries investigated (discs, cylinders, cones, and circular paraboloids).

- 2) The set composites were found to be openly porous with sufficient strength. The composites were characterised for:
 - a. Porosity, frit, and binder amounts, distribution, and dispersion as measured via pycnometry (amounts of phases), OLM (2D phase distribution, dispersion and pore size), SEM (phase distribution, dispersion, surface morphology, and cracking), micro-CT (pore amounts, distribution, and dispersion);
 - b. Mechanical behaviour via UCS, which indicated a positive correlation to binder amount and an inverse correlation with porosity. Higher statistical variability in UCS was positively correlated to binder amount.
 - c. Failure mode in compression, which indicated that the mode was weakly correlated to the amount of binder phase: a single shear failure mode was observed at low strengths (low amounts of binder) and a mixed failure mode was observed at higher strengths (higher amounts of binder).

- 3) All investigated composite compositions were found to form calcium phosphate minerals (OCP, HCA) *in vitro*, as assessed by:
- a. SEM with EDX, which found mineralisation rate and distribution to be inversely related to binder amount.
 - b. The formation of multiple gel layers and the mineralisation of binder phase in composites despite the absence of CaP minerals in sodium silicate (binder) control specimens, suggesting a chemical change to the sodium silicate binder during composite fabrication that permits mineralisation *in vitro*.
 - c. XRD, which identified the formation of OCP and HCA in all composite compositions, with mineralisation rate and amount inversely related to binder amount; additionally, the infiltration of halite into sodium silicate control specimens, indicating that ions from SBF enter the hydrated sodium silicate gel network.
 - d. FTIR, which confirmed the formation of HCA *in vitro* for all composite specimens, and the formation of cristobalite *in vitro* for sodium silicate control specimens.

All composite materials investigated herein in were found to fulfil the aforementioned design criteria, as assessed in this research. Synthesising the outcomes of this research, it is suggested that the most ideal composite composition was 7.4 vol% binder, which had the highest amount of open porosity, a SA/V ratio matching trabecular bone, the shortest manipulation and setting time, excellent geometric stability, and displayed the greatest and most uniform mineralisation response *in vitro*. Though 7.4 vol% composites were found to have the lowest compressive strength, the magnitude of the strength was sufficient to allow for handling and interim dimensional stability *in vitro*.

The conclusions of this research in relation to the evaluated bone tissue scaffold design criteria are summarised in Table 5-1.

Design Criteria	Characterisation Technique	Evaluation of control specimens and composite scaffolds with compositions: 7.4, 11.4, and 16.1 vol% binder
Formability	Mould reproduction fidelity Compressability Manipulation time	<ol style="list-style-type: none"> 1. Compositions are capable of being formed into prescribed geometries (right cylinder h/d 0.27, 2.25; right circular cone, circular paraboloid). 2. Compactable by hand as unset paste. 3. Manipulation time = 2-8 minutes.
Geometric Stability	Resolution to mould	<ol style="list-style-type: none"> 4. Geometry is preserved during de-moulding and handling. 5. Excellent mould reproduction accuracy: diametrical difference 2.5-5%; height difference 0.6-7.6%
Porosity	OLM with epoxy infiltration Gas pycnometry Micro-CT	<ol style="list-style-type: none"> 6. Average 2D pore size: 156-285 μm 7. 2D pore size = $f(\text{binder}^{-1})$ 8. Porosity = 31-44 vol% 9. 0.1-1.1 vol% closed pores 10. Porosity = $f(\text{binder}^{-1})$ 11. SA/V = 19-33 mm^{-1} 12. SA/V = $f(\text{binder}^{-1})$ 13. SA/V variability = $f(\text{binder})$ 14. Interconnected open porous network well distributed within specimen
Load-Bearing Capacity	Unconfined compression test	<ol style="list-style-type: none"> 15. Average UCS = 1.3-4.4 MPa 16. UCS = $f(\text{binder})$ 17. UCS variability = $f(\text{binder})$
	SEM fractography	18. Adhesive failure between phases and cohesive failure within binder phase.

Bioactivity	SEM-EDX EDX	<p>19. 1st-level feature size = f(binder⁻¹)</p> <p>20. 2nd-level feature size = f(binder)</p> <p>21. Mineral distribution = f(binder⁻¹)</p> <p>22. Surface minerals concentrated at binder necks of higher binder phase specimens.</p> <p>23. Outer surface mineralisation > inner surface mineralisation of composites.</p> <p>24. Mineralisation of every observed composite composition.</p> <p>25. No calcium phosphate mineralisation of sodium silicate control.</p>
	XRD	<p>26. HCA formation = f(binder⁻¹)</p> <p>27. HCA formation = f(immersion time)</p> <p>28. OCP formation observed at varying immersion times.</p> <p>29. Halite from SBF infiltrates hydrated sodium silicate gel network.</p> <p>30. Sodium silicate cristobalite formation = f(immersion time)</p>
	FTIR	<p>31. P-O bond formation = f(immersion time)</p> <p>32. Sodium silicate cristobalite formation = f(immersion time)</p>
Resorbability	<i>In vitro</i> immersion	<p>33. 45S5 clinically demonstrated to be resorbable [2].</p> <p>34. Sodium silicate binder phase forms water-soluble gel.</p>

Table 5-1. Summary evaluation of design criteria explored in this thesis.

5.2 Future Work

The results revealed from this research are promising, as the composite scaffolds were found to achieve every established design criterion. However, further investigation of this material is necessary to ensure its clinical viability, and additional development will be required to bring this research to fruition as a successful clinical bone tissue scaffold.

Potential areas of future work are as follows:

- Additional characterisation of sodium silicate. The viscosity, molar ratio, and pH changes as a function of CO₂ gas exposure were outside the scope of this work, but are necessary to ensure consistency of fabricated composites. Molar ratio and species concentrations should be verified using ICP-OES (inductively coupled plasma-optical emission spectroscopy), AAS (atomic absorption spectroscopy) or similar chemical analysis. Additionally, determining the amount of dissolved CO₂ gas present in the sodium silicate used in this study is required to replicate the necessary characteristics (viscosity, wetting behaviour, manipulation time) when using a different batch of aqueous sodium silicate.
- Investigation of the resorbability of hydrated binder phase (sodium silicate) gel, including local pH changes and degradation products. Though hydrated sodium silicate gels similar to those observed in this work have been shown to be water-soluble, it is necessary to assess the rate and extent of degradation of sodium silicate gels in biological systems. The effect of ions present in simulated body fluid *in vitro* or in bodily fluids *in vivo* on the hydrated binder phase has yet to be fully understood. Moreover, the safety of any degradation products or pH changes as a result of resorption must be examined.
- Exploration of accelerated setting time by application of CO₂ gas. Similar to the process in which sand casting foundry cores are set in under one minute [3], the application of CO₂ gas to these composite specimens has the potential to reduce

setting time and increase clinical utility. Appropriate investigation of CO₂ curing must be conducted to avoid 'overgassing', a phenomena that occurs in sand casting, in which excessive application of CO₂ gas causes the formation of sodium bicarbonate and a significant reduction of binder strength [3, 4, 5].

- Identification of reaction product between binder phase and bioactive glass frit. The mineralisation of the binder phase when present in the composite, but not when isolated, indicates that a chemical change occurred between the bioactive glass frit and sodium silicate binder. Evidence of etching on bioactive glass in as-fabricated samples suggests that a reaction occurred during fabrication, but additional investigation is necessary to elucidate the exact mechanism and resultant product of this chemical reaction. Furthermore, the effect of this reaction on *in vitro* gel formation and mineralisation behaviour must be identified. It is evident that the interaction between bioactive glass and sodium silicate influences *in vitro* mineralisation behaviour; by identifying the exact nature of this influence, it follows that the composite material can be further improved and optimised.
- Assessment of the biological safety of the composite material. Although both 45S5 bioactive glass and sodium silicate are both present in FDA-approved and clinically utilised biomedical implants [2, 6], it is necessary to analyse the safety of this particular composite. It would be prudent to conduct *in vitro* assessments, such as those outlined by ISO 10993: Biological evaluation of medical devices (in particular, ISO 10993-5 [7]: Tests for *in vitro* cytotoxicity; ISO 10993-6 [8]: Tests for local effects after implantation; ISO 10993-9 [9]: Framework for identification and quantification of potential degradation products).
- *In vivo* assessment of bioactivity, bone growth, geometric stability, mechanical properties, resorption, and safety. Following from the successful *in vitro* characterisation conducted in this study, it is necessary to evaluate performance of the composite material *in vivo*, through an animal study, to ensure its clinical viability.

Bibliography – Chapter Five

- [1] L. L. Hench, D. L. Wheeler and D. C. Greenspan, “Molecular Control of Bioactivity in Sol-Gel Glasses,” *Journal of Sol-Gel Science and Technology*, vol. 13, pp. 245-250, 1998.
- [2] F. Baino, G. Novjra and C. Vitale-Brovarone, “Bioceramics and Scaffolds: A winning Combination for Tissue engineering,” *Frontiers in Bioengineering and Biotechnology*, vol. 3, no. 202, pp. 1-17, 2015.
- [3] J. R. Brown, “Chapter 14: Sodium silicate bonded sand,” in *Foseco Ferrous Foundryman's Handbook, Eleventh Edition*, Oxford, UK, Butterworth-Heinemann, 2000, pp. 204-216.
- [4] D. V. Atterton, “The carbon-dioxide process,” *AFS Transactions*, vol. 64, pp. 14-18, 1956.
- [5] Y. Owusu, “Physical-chemistry study of sodium silicate as a foundry sand binder,” *Advances in Colloid and Interface Science*, vol. 18, no. 1-2, pp. 57-91, 1982.
- [6] B. R. Constanz, “Calcium phosphate cements prepared from silicate solutions”. United States of America Patent US6719993B2, 28 April 2000.
- [7] ISO, “ISO 10993-5: Biological evaluation of medical devices — Part 5: Tests for in vitro cytotoxicity,” International Organization for Standardization, Geneva, Switzerland, 2009.
- [8] ISO, “ISO 10993-6: Biological evaluation of medical devices — Part 6: Tests for local effects after implantation,” International Organization for Standardization, Geneva, Switzerland, 2016.
- [9] ISO, “ISO 10993-9: Biological evaluation of medical devices — Part 9: Framework for identification and quantification of potential degradation products,” International Organization for Standardization, Geneva, Switzerland, 2019.

Bibliography

Chapter One — Introduction

- [1] J. R. Jones, P. D. Lee and L. L. Hench, "Hierarchical porous materials for tissue engineering," *Philosophical Transactions of the Royal Society: A*, vol. 364, pp. 263-281, 2006.
- [2] A. Bachoura, T. G. Guitton, R. M. Smith, M. S. Vrahas, D. Zurakowski and D. Ring, "Infirmary and Injury Complexity are Risk Factors for Surgical-site Infection after Operative Fracture Care," *Clinical Orthopaedics and Related Research*, vol. 469, no. 9, pp. 2621-2630, 2011.
- [3] J. R. Jones, "Review of bioactive glass : from Hench to hybrids," *Acta Biomaterialia*, vol. 9, pp. 4457-4486, 2012.
- [4] L. L. Hench, "Challenges for Bioceramics in the 21st Century," *American Ceramic Society Bulletin*, vol. 84, no. 9, pp. 18-21, 2005.
- [5] J. Wilson, A. Yli-Urpo and H. Risto-Pekka, "Bioactive glasses: clinical applications," in *An Introduction to Bioceramics*, Singapore, World Scientific, 1993, pp. 63-74.
- [6] J. R. Jones, "New trends in bioactive scaffolds: The importance of nanostructure," *J. Euro. Ceram. Soc.*, vol. 29, pp. 1275-1281, 2009.
- [7] F. Baino, G. Novaira and C. Vitale-Brovarone, "Bioceramics and scaffolds: A winning combination for tissue engineering," *Frontiers in Bioengineering and Biotechnology*, vol. 3, pp. 1-17, 2015.
- [8] C. M. Guzzo and J. A. Nychka, "Fabrication of a Porous and Formable Ceramic Composite Bone Tissue Scaffold at Ambient Temperature," *Metallurgical and Materials Transactions A*, Under Review, 2020.
- [9] P. Chicolata, V. Kulda and V. Babuska, "Fabrication of scaffolds for bone-tissue regeneration," *Materials*, vol. 12, no. 568, pp. 1-25, 2019.
- [10] H. Qu, H. Fu, Z. Han and Y. Sun, "Biomaterials for bone tissue engineering scaffolds: A Review," *RSC Advances*, vol. 9, no. 45, pp. 26252-26262, 2019.
- [11] E. Fiume, J. Barberi, E. Verné and F. Baino, "Bioactive Glasses : From Parent 45S5 Composition to Scaffold-Assisted Tissue-Healing Therapies," *Journal of Functional Biomaterials*, vol. 9, no. 24, pp. 1-33, 2018.

Chapter Two — Background and Literature Review

- [1] L. Gaviria, L. Actis, T. Guda and J. Ong, "Bone Grafting Evolution," in *Translating Biomaterials for Bone Graft: Bench-top to Clinical Applications*, Boca Raton, FL, CRC Press, 2017, pp. 3-21.
- [2] Centres for Disease Control and Prevention, "10 Leading Causes of Nonfatal Injury, United States," National Center for Injury Prevention and Control, CDC, Atlanta, GA, 2016.
- [3] F. A. Al-Mulhim, M. A. Baragbah, M. Sadat-Ali, A. S. Alomran and M. Q. Azam, "Prevalence of Surgical Site Infection in Orthopedic Surgery: A 5-year Analysis," *International Surgery*, vol. 99, pp. 264-268, 2014.
- [4] A. Bachoura, T. G. Guitton, R. M. Smith, M. S. Vrahas, D. Zurakowski and D. Ring, "Infirmity and Injury Complexity are Risk Factors for Surgical-site Infection after Operative Fracture Care," *Clinical Orthopaedics and Related Research*, vol. 469, no. 9, pp. 2621-2630, 2011.
- [5] M. Bhola, A. L. Neely and S. Kolhatkar, "Immediate Implant Placement: Clinical Decisions, Advantages, and Disadvantages," *Journal of Prosthodontics*, vol. 17, no. 7, pp. 576-81, 2008.
- [6] M. Ahn, K. An, J. Choi and D. Sohn, "Immediate Loading with Mini Dental Implants in the Fully Edentulous Mandible," *Implant Dentistry*, vol. 13, no. 4, pp. 367-72, 2004.
- [7] J. S. Silber, G. D. Anderson, S. D. Daffner, B. T. Brislin, M. J. Leland, A. S. Hilibrand, A. R. Vaccaro and T. J. Albert, "Donor Site Morbidity After Anterior Iliac Crest Bone Harvest for Single-Level Anterior Cervical Discectomy and Fusion," *Spine*, vol. 28, no. 2, pp. 134-139, 2003.
- [8] S. V. Dorozhkin, "Calcium Orthophosphates as Bioceramics: State of the Art," *Journal of Functional Biomaterials*, vol. 1, pp. 22-107, 2010.
- [9] V. Campana, G. Milano, E. Pagano, M. Barba, C. Cicione, G. Salonna, W. Lattanzi and G. Logroscino, "Bone substitutes in orthopaedic surgery: from basic science to clinical practice," *Journal of Materials Science: Materials in Medicine*, vol. 25, no. 10, pp. 2445-2461, 2014.
- [10] S. N. Parikh, "Bone graft substitutes: past, present, future.," *Journal of Postgraduate Medicine*, vol. 48, no. 2, pp. 142-148, 2002.

- [11] Datamonitor, "United States - Bone Graft Substitutes," Datamonitor, New York, NY, 2001.
- [12] American Academy of Orthopaedic Surgeons, "Bone-Graft Substitutes: Facts, Fictions & Applications," American Academy of Orthopaedic Surgeons, New Orleans, LA, 2003.
- [13] F. Baino, G. Novaira and C. Vitale-Brovarone, "Bioceramics and scaffolds: A winning combination for tissue engineering," *Frontiers in Bioengineering and Biotechnology*, vol. 3, pp. 1-17, 2015.
- [14] Z. Gou, A. Ballo and W. Xia, "Chapter 5: Biomimetic Preparation and Biomineralization of Bioceramics," in *Advanced Bioactive Inorganic Materials for Bone Regeneration and Drug Delivery*, Rolla, FL, CRC Press, 2013, pp. 117-146.
- [15] H. Qu, H. Fu, Z. Han and Y. Sun, "Biomaterials for bone tissue engineering scaffolds: A review," *RSC Advances*, vol. 9, no. 45, pp. 26252-26262, 2019.
- [16] X. Zhao, "Introduction to bioactive materials in medicine," in *Bioactive Materials in Medicine*, New York, Elsevier, 2011, pp. 1-13.
- [17] E. Fiume, J. Barberi, E. Verné and F. Baino, "Bioactive Glasses: From Parent 45S5 Composition to Scaffold-Assisted Tissue-Healing Therapies," *Journal of Functional Biomaterials*, vol. 9, no. 24, pp. 1-33, 2018.
- [18] L. L. Hench and E. Fielder, "3.1.4 Biological Gel-Glasses," in *Sol-Gel Technologies for Glass Producers and Users*, New York, Springer, 2004, p. 153.
- [19] L. L. Hench, D. L. Wheeler and D. C. Greenspan, "Molecular Control of Bioactivity in Sol-Gel Glasses," *Journal of Sol-Gel Science and Technology*, vol. 12, pp. 245-250, 1998.
- [20] P. Ducheyne and Q. Qiu, "Bioactive ceramics: The effect of surface reactivity on bone formation and bone cell function," *Biomaterials*, vol. 20, pp. 2287-2303, 1999.
- [21] L. Varila, S. Fagerlund, T. Lehtonen, J. Tuominen and L. Hupa, "Surface reactions of bioactive glasses in buffered solutions," *Journal of the European Ceramic Society*, vol. 32, pp. 2757-2763, 2012.
- [22] M. N. Rahaman, D. E. Day, B. S. Bal, Q. Fu, S. B. Jung, L. F. Bonewald and A. P. Tomsia, "Bioactive glass in tissue engineering," *Acta Biomaterialia*, vol. 7, no. 6, pp. 2355-2373, 2011.

- [23] J. R. Jones, "Review of bioactive glass: From Hench to hybrids," *Acta Biomaterialia*, vol. 9, pp. 4457-4486, 2013.
- [24] A. Lotsari, A. K. Rajasekharan, M. Halvarsson and M. Andersson, "Transformation of amorphous calcium phosphate to bone-like apatite," *Nature Communications*, vol. 9, no. 1, pp. 1-11, 2018.
- [25] L. L. Hench, D. E. Day, W. Höland and V. M. Rheinberger, "Glass and Medicine," *International Journal of Applied Glass Science*, vol. 1, no. 1, pp. 104-117, 2010.
- [26] P. Li, C. Ohtsuki, T. Kokubo, K. Nakanishi, N. Soga, T. Nakamura and T. Yamamuro, "Apatite Formation Induced by Silica Gel in a Simulated Body Fluid," *Journal of the American Ceramic Society*, vol. 75, no. 8, pp. 2094-2097, 1992.
- [27] G. Jell, I. Notingher, O. Tsigkou, P. Notingher, J. M. Polak, L. L. Hench and M. M. Stevens, "Bioactive glass-induced osteoblast differentiation: A noninvasive spectroscopic study," *Journal of Biomedical Materials Research*, vol. 86A, no. 1, pp. 31-40, 2007.
- [28] J. Wilson and S. B. Low, "Bioactive ceramics for periodontal treatment: comparative studies in the Patus monkey.," *Journal of Applied Biomaterials*, vol. 3, no. 2, pp. 123-129, 1992.
- [29] T. Albrektsson and C. Johansson, "Osteoinduction, osteoconduction and osseointegration," *European Spin Journal*, vol. 2S, pp. 96-101, 2001.
- [30] L. L. Hench, "The story of Bioglass (R)," *Journal of Materials Science: Materials in Medicine*, vol. 17, pp. 967-978, 2006.
- [31] R. Lanza, J. Gearhart, B. Hogan, D. Melton, R. Pedersen, J. Thomson and M. West, *Handbook of Stem Cells*, New York: Elsevier, 2004.
- [32] T. L. McCarthy, M. Centrella and E. Canalis, "Insulin-like growth factor (IGF) and bone.," *Connective Tissue Research*, vol. 20, no. 1-4, pp. 277-282, 1989.
- [33] S. Boonrungsiman, E. Gentleman, R. Carzaniga, N. D. Evans, D. W. McComb, A. E. Porter and M. M. Stevens, "The role of intracellular calcium phosphate in osteoblast-mediated bone apatite formation," *Proceedings of the National Academy of Sciences of the United States of America*, vol. 109, no. 35, pp. 14170-14175, 2012.

- [34] A. F. Mavrogenis, R. Dimitriou, J. Parvizi and G. C. Babis, "Biology of implant osseointegration.," *Journal of Musculoskeletal and Neuronal Interactions*, vol. 9, no. 2, pp. 61-71, 2009.
- [35] L.-C. Gerhardt and A. R. Boccaccini, "Bioactive Glass and Glass-Ceramic Scaffolds for Bone Tissue Engineering," *Materials*, vol. 3, pp. 3867-3910, 2010.
- [36] A. R. Boccaccini, Q. Chen, L. Lefebvre, L. Gremillard and J. Chevalier, "Sintering, crystallisation and biodegradation behaviour of Bioglass-derived glass-ceramics," *Faraday Discussions*, vol. 136, pp. 27-44, 2007.
- [37] J. A. Sanz-Herrera and A. R. Boccaccini, "Modelling bioactivity and degradation of bioactive glass based tissue engineering scaffolds," *International Journal of Solids and Structures*, vol. 48, no. 2, pp. 257-268, 2011.
- [38] I. Izqueirido-Barba, A. J. Salinas and M. Vallet-Regí, "Bioactive Glasses: From Macro to Nano," *International Journal of Applied Glass Science*, vol. 4, no. 2, pp. 149-161, 2013.
- [39] K. R. Rust, G. T. Singleton and P. J. Antonelli, "Bioglass middle ear prosthesis: long-term results," *American Journal of Otolaryngology*, vol. 17, pp. 371-374, 1996.
- [40] L. L. Hench, "Challenges for Bioceramics in the 21st Century," *American Ceramic Society Bulletin*, vol. 84, no. 9, pp. 18-21, 2005.
- [41] J. Wilson, A. Yli-Urpo and H. Risto-Pekka, "Bioactive glasses: clinical applications," in *An Introduction to Bioceramics*, Singapore, World Scientific, 1993, pp. 63-74.
- [42] S. Hu, J. Chang, M. Liu and C. Ning, "Study on antibacterial effect of 45S5 Bioglass," *Journal of Materials Science: Materials in Medicine*, vol. 20, no. 1, pp. 281-6, 2009.
- [43] P. Li, F. Zhang and T. Kokubo, "The effect of residual glassy phase in a bioactive glass-ceramic on the formation of its surface apatite layer in vitro," *Journal of Materials Science: Materials in Medicine*, vol. 3, pp. 452-256, 1992.
- [44] C. Wu, J. Chang and Y. Xiao, "Chapter 1: Mesoporous Bioactive Glasses for Drug Delivery and Bone Tissue Regeneration," in *Advanced Bioactive Inorganic Materials for Bone Regeneration and Drug Delivery*, Boca Raton, FL, CRC Press, 2013, pp. 1-24.
- [45] G. Kaur, G. Pickrell, N. Sriranganathan, V. Kumar and D. Homa, "Review and state of the art: Sol-gel and melt quenched bioactive glasses for tissue engineering.," *Journal of*

Biomedical Materials Research - Part B: Applied Biomaterials, vol. 104, no. 6, pp. 1248-1275, 2016.

- [46] Q. Chen, J. Roether and A. Boccaccini, "Tissue Engineering Scaffolds from Bioactive Glass and Composite Materials," *Topics in Tissue Engineering*, vol. 4, no. 6, pp. 1-27, 2008.
- [47] Y. Zhang and C. Wu, "Chapter 7: Bioactive Inorganic and Organic Composite Materials for Bone Regeneration and Gene Delivery," in *Advanced Bioactive Inorganic Materials for Bone Regeneration and Drug Delivery*, Rolla, FL, CRC Press, 2013, pp. 177-211.
- [48] Y. Luo, A. Lode, C. Wu and M. Gelinsky, "Chapter 4: 3D Plotting of Bioceramic Scaffolds under Physiological Conditions for Bone Tissue Engineering," in *Advanced Bioactive Inorganic Materials for Bone Regeneration and Drug Delivery*, Rolla, FL, CRC Press, 2013, pp. 82-116.
- [49] L. Roseti, V. Parisi, M. Petretta, C. Cavallo, G. Desando, I. Bartolotti and B. Grigolo, "Scaffolds for Bone Tissue Engineering: State of the art and new perspectives," *Materials Science and Engineering C*, vol. 78, pp. 1246-1262, 2017.
- [50] M. Navarro, A. Michiardi, O. Castaño and J. A. Planell, "Biomaterials in orthopaedics," *Journal of the Royal Society: Interface*, vol. 5, no. 27, pp. 1137-1158, 2008.
- [51] G. Lagaly, W. Tufar, A. Minihan and A. Lovell, "Silicates," in *Ullman's Encyclopedia of Industrial Chemistry*, vol. 32, Weinheim, Wiley-VCH Verlag, 2012, pp. 509-572.
- [52] S. Ebnesajjad, "5.20.1: Soluble Silicates (Potassium and Sodium Silicate)," in *Adhesives Technology Handbook (Second Edition)*, Norwich, NY, William Andrew Publishing, 2009, pp. 63-135.
- [53] H.-J. Engelhardt and L. E. von Borstel, "The behaviour of sodium silicate solutions (water glass) in the saline environment and their use in salt mining," *Zeitschrift der Deutschen Gesellschaft für Geowissenschaften (German Journal of Geology)*, vol. 165, no. 1, pp. 115-122, 2014.
- [54] J. G. Vail and J. H. Wills, "Chapter 2: Present Practices," in *Soluble Silicates - Their Properties and Uses, Volumes 1-2; American Chemical Society, Monograph Series*, New York, NY, Book Division, Reinhold Publishing Corporation, 1952, pp. 16-43.
- [55] J. F. Healy, "18.2: Technology: Glass," in *Pliny the Elder on Science and Technology*, Oxford, UK, Oxford University Press, 1999, pp. 350-358.

- [56] Pliny, "Natural History, Volume X: Books 36-37. Translated by D. R. Eichholz," in *Loeb Classical Library 419*, Cambridge, MA, Harvard University Press, 1962, pp. 150-151.
- [57] H. B. Ellis, "Stabilization of soils with lime and sodium silicate," Iowa State University, Ames, IA, 1963.
- [58] J. G. Vail and J. H. Wills, "Chapter 1: The Beginnings," in *Soluble Silicates - Their Properties and Uses, Volumes 1-2; American Chemical Society, Monograph Series*, New York, NY, Book Division, Reinhold Publishing Corporation, 1952, pp. 4-15.
- [59] D. V. Atterton, "The carbon-dioxide process," *AFS Transactions*, vol. 64, pp. 14-18, 1956.
- [60] D. V. Atterton and J. V. Stevenson, "The Carbon Dioxide Process: A Look Back -- A Look Forward," *AFS Transactions*, vol. 89, pp. 55-64, 1981.
- [61] Y. Owusu, "Physical-chemistry study of sodium silicate as a foundry sand binder," *Advances in Colloid and Interface Science*, vol. 18, no. 1-2, pp. 57-91, 1982.
- [62] M. Tognonvi, S. Rossignol and J. Bonnet, "Physical-chemistry of sodium silicate gelation in an alkaline medium," *Journal of Sol-Gel Science and Technology*, vol. 58, no. 3, pp. 625-635, 2011.
- [63] V. S. Komlev, J. V. Rau, M. Fosca, A. S. Fomin, A. N. Gurin, S. M. Barinov and R. Caminiti, "Single-phase bone cement based on dicalcium phosphate dihydrate powder and sodium silicate solution," *Materials Letters*, vol. 73, pp. 115-118, 2012.
- [64] H. Zhou, T. J. Luchini, S. Bhaduri and L. Deng, "Silicon (Si) containing bone cements: a review," *Materials Technology: Advanced Biomaterials*, vol. 30, no. B4, pp. 229-236, 2015.
- [65] S. M. Kenny and M. Buggy, "Bone cements and fillers: a review," *Journal of Materials Science: Materials in Medicine*, vol. 14, no. 11, pp. 923-938, 2003.
- [66] Z. Huan and J. Chang, "Effect of sodium carbonate solution on self-setting properties of tricalcium silicate bone cement," *Journal of Biomaterials Applications*, vol. 23, no. 3, pp. 247-262, 2008.
- [67] A. L. Oliveira, P. B. Malafaya and R. L. Reis, "Sodium Silicate Gel Induced Self-Mineralization of Different Compact and Porous Polymeric Structures," *Key Engineering Materials*, Vols. 192-195, no. Bioceramics 13, pp. 75-78, 2001.

- [68] P. Chocholata, V. Kulda and B. Vaclav, "Fabrication of scaffolds for bone-tissue regeneration," *Materials*, vol. 12, no. 568, pp. 1-25, 2019.
- [69] L. L. Hench, "Bioceramics," *Journal of the American Ceramic Society*, vol. 81, no. 7, pp. 1705-1728, 1998.
- [70] A. Mombelli and N. P. Lang, "The diagnosis and treatment of peri-implantitis," *Periodontology 2000*, vol. 17, no. 1, pp. 63-76, 1998.
- [71] N. Zitzmann and T. Berglundh, "Definition and prevalence of peri-implant diseases," *Periodontology*, vol. 35, no. s8, pp. 268-291, 2008.
- [72] B. M. Holzapfel, J. C. Reichert, J.-T. Schantz, U. Gbureck, L. Rackwitz, U. Nöth, F. Jakob, M. Rudert, J. Groll and D. W. Hutmacher, "How smart do biomaterials need to be? A translational science and clinical point of view," *Advanced Drug Delivery Reviews*, vol. 65, no. 4, pp. 581-603, 2013.

Chapter Three — Experimental Design

- [1] G. M. Nelson, A. G. McDonald and J. A. Nychka, "Structure and bioactivity of Ti/bioactive glass 'changing landscape coatings'," *Surface Innovations*, vol. 1, no. S14, pp. 209-223, 2013.
- [2] C. M. Guzzo and J. A. Nychka, "Fabrication of a Porous and Formable Ceramic Composite Bone Tissue Scaffold at Ambient Temperature," *Metallurgical and Materials Transactions A*, Under Review, 2020.
- [3] S. Kashyap, "Effect of crystallinity on crack propagation and mineralization of bioactive glass 45S5," University of Alberta, Edmonton, AB, 2010.
- [4] E. Olson, "Shape Factors and Their Use in Image Analysis - Part 1: Theory," *Journal of GXP Compliance*, vol. 15, no. 3, pp. 85-96, 2011.
- [5] S. Endoh, "Chapter 1.3: Particle Shape Characterization," in *Powder Technology Handbook, Fourth Edition*, Boca Raton, FL, CRC Press, 2020, pp. 19-26.
- [6] ASTM International, "ASTM E2651-19: Standard Guide for Particle Size Analysis," ASTM International, West Conshohocken, USA, 2019.
- [7] T. Allen, "Sampling of Powders," in *Particle Size Measurement*, Berlin/Heidelberg, Springer Science+Business Media, 2012, p. 39.
- [8] J. M. Berg, J. L. Tymoczko and L. Stryer, "8.4: The Michaelis-Menten Model Accounts for the Kinetic Properties of Many Enzymes," in *Biochemistry, 5th ed.*, New York, NY, W. H. Freeman and Company, 2002.
- [9] Y. Leng, "Scanning Electron Microscopy," in *Materials Characterization: Introduction to Microscopic and Spectroscopic Methods*, Singapore, John Wiley & Sons (Asia) Pte Ltd, 2008, pp. 121-144.
- [10] J. D. Boerckel, D. E. Mason, A. M. McDermott and E. Alsberg, "Microcomputed tomography: approaches and applications in bioengineering," *Stem Cell Research & Therapy*, vol. 5, no. 144, pp. 1-12, 2014.
- [11] ASTM International, "Standard Test Methods for Compressive Strength and Elastic Moduli of Intact Rock Core Specimens under Varying States of Stress and Temperatures," ASTM International, West Conshohocken, PA, 2017.
- [12] T. Kokubo and H. Takadama, "How useful is SBF in predicting in vivo bone activity?," *Biomaterials*, vol. 27, pp. 2907-2915, 2006.

- [13] Y. Leng, "X-Ray Spectroscopy for Elemental Analysis," in *Materials Characterization: Introduction to Microscopic and Spectroscopic Methods*, Singapore, John Wiley & Sons (Asia) Pte Ltd, 2008, pp. 171-196.
- [14] D. Brabazon and A. Raffer, "Chapter 3: Advanced Characterization Techniques for Nanostructures," in *Emerging Nanotechnologies for Manufacturing*, Oxford, UK, William Andrew Applied Science Publishers, 2009, pp. 59-91.
- [15] O. H. Andersson and K. H. Karlsson, "On the bioactivity of silicate glass," *J. Non. Cryst. Solids*, vol. 129, pp. 145-151, 1991.
- [16] Y. Leng, "X-Ray Diffraction Methods," in *Materials Characterization: Introduction to Microscopic and Spectroscopic Methods*, Singapore, John Wiley & Sons (Asia) Pte Ltd, 2008, pp. 45-77.
- [17] H. Pirayesh and J. A. Nychka, "Sol-gel synthesis of bioactive glass-ceramic 45S5 and its in vitro dissolution and mineralization behaviour," *Journal of the American Ceramic Society*, vol. 96, no. 5, pp. 1643-1650, 2013.
- [18] Y. Leng, "Vibrational Spectroscopy for Molecular Analysis," in *Materials Characterization: Introduction to Microscopic and Spectroscopic Methods Author(s): Yang Leng*, Singapore, John Wiley & Sons (Asia) Pte Ltd, 2008, pp. 253-300.

Chapter Four — Results and Discussion

- [1] ISO, "ISO 23145-1 - Fine ceramics (advanced ceramics, advanced technical ceramics) — Determination of bulk density of ceramic powders — Part 1: Tap density - First Edition," ISO - International Organization for Standardization, Geneva, Switzerland, 2007.
- [2] E. P. Cox, "A Method of Assigning Numerical and Percentage Values to the Degree of Roundness of Sand Grains," *Journal of Paleontology*, vol. 1, no. 3, pp. 179-183, 1927.
- [3] K. Miura, K. Maeda, M. Furukawa and S. Toki, "Mechanical characteristics of sands with different primary properties," *Soils and Foundations*, vol. 38, no. 4, pp. 159-172, 1998.
- [4] M. Cubrinovski and K. Ishihara, "Maximum and minimum void ratio characteristics of sands," *Soils and Foundations*, vol. 42, no. 6, pp. 65-78, 2002.
- [5] X. Jia and R. A. Williams, "A packing algorithm for particles of arbitrary shapes," *Powder Technology*, vol. 120, pp. 175-186, 2001.
- [6] D. V. Atterton, "The carbon-dioxide process," *AFS Transactions*, vol. 64, pp. 14-18, 1956.
- [7] C. M. Guzzo and J. A. Nychka, "Fabrication of a Porous and Formable Ceramic Composite Bone Tissue Scaffold at Ambient Temperature," *Metallurgical and Materials Transactions A*, Under Review, 2020.
- [8] Flexbar Machine Corporation, *Reprorubber Brochure REP-0409*, Islandia, NY: Flexbar Machine Corporation, 2017.
- [9] C. M. Guzzo and J. A. Nychka, "In vitro response of a porous and formable ceramic composite bone tissue scaffold," *Journal of the Mechanical Behaviour of Biological Materials*, Under Review, 2020.
- [10] F. Baino, G. Novajra and C. Vitale-Brovarone, "Bioceramics and scaffolds: A winning combination for tissue engineering," *Frontiers in Bioengineering and Biotechnology*, vol. 3, pp. 1-17, 2015.
- [11] L. Gerhardt and A. Boccaccini, "Bioactive glass and glass-ceramic scaffolds for bone tissue engineering," *Materials*, vol. 3, pp. 3867-3910, 2010.
- [12] C. J. McMahon, "Chapter 16: Rigid Connective Tissue: Bone," in *Structural Materials: A Textbook with Animations*, Philadelphia, PA: Merion Books, 2004, pp. 407-414.
- [13] M. T. Tognonvi, S. Rossignol and J. P. Bonnet, "Physical-chemistry of sodium silicate gelation in an alkaline medium," *Journal of Sol-Gel Science and Technology*, vol. 58, no. 3, pp. 625-635, 2011.

- [14] S. Hu, J. Chang, M. Liu and C. Ning, "Study on antibacterial effect of 45S5 Bioglass," *Journal of Materials Science: Materials in Medicine*, vol. 20, no. 1, pp. 281-6, 2009.
- [15] F. E. Ciraldo, E. Boccardi, V. Melli, F. Westhauser and A. R. Boccaccini, "Tackling bioactive glass excessive in vitro bioreactivity: Preconditioning approaches for cell culture tests," *Acta Biomaterialia*, vol. 75, pp. 3-10, 2018.
- [16] A. Lotsari, A. K. Rajasekharan, M. Halvarsson and M. Andersson, "Transformation of amorphous calcium phosphate to bone-like apatite," *Nature Communications*, vol. 9, no. 1, 2018.
- [17] Seville, J. Wu and Chuan-Yu, "8.4 Interaction of Particles with Liquid Bridges," in *Particle Technology and Engineering--An Engineer's Guide to Particles and Powders--Fundamentals and Computational Approaches*, Elsevier, 2016.
- [18] L. L. Hench, D. L. Wheeler and D. C. Greenspan, "Molecular control of bioactivity in sol-gel glasses," *J. Sol-Gel Sci Technol*, vol. 13, no. 1-3, pp. 245-250, 1998.
- [19] Y. Yu, Z. Bacsik and M. Eden, "Contrasting in vitro apatite growth from bioactive glass surfaces with that of spontaneous precipitation," *Materials*, vol. 11, no. p, pp. 20-22, 2018.
- [20] J. R. Jones, "Review of bioactive glass: From Hench to hybrids," *Acta Biomaterialia*, vol. 9, pp. 4457-4486, 2013.
- [21] I. Notingher and et al., "Application of FTIR and Raman spectroscopy to characterisation of bioactive materials and living cells," *Spectroscopy*, vol. 17, no. 2-3, pp. 275-288, 2003.
- [22] O. P. Filho, G. P. Latorre and L. L. Hench, "Effect of crystallization on apatite-layer formation of bioactive glass 45S5," *J Biomed Mater Res*, vol. 30, no. 4, pp. 509-514, 1996.
- [23] H. Aguiar, J. Serra, P. Gonzalez and B. Leon, "Structural study of sol-gel silicate glasses by IR and Raman spectroscopies," *J Non-Cryst Sol*, vol. 355, pp. 475-480, 2009.
- [24] G. S. Pappas, P. Liatsi, I. A. Kartsonakis, I. Danilidis and G. Kordas, "Synthesis and characterization of new SiO₂-CaO hollow nanospheres by sol-gel method: bioactivity of the new system," *J Non Cryst Sol*, vol. 354, no. 2-9, pp. 755-760, 2008.
- [25] H. -H. Fricke, M. Mattenklott, H. Parlar, A. Hartwig and MAK Commission, "Method for the determination of quartz and cristobalite (Air Monitoring Methods, 2015)," in *The MAK-Collection for Occupational Health and Safety: Annual Thresholds and Classifications for the Workplace*, Heidelberg, Wiley-Verlag GmbH & Co. KGaA, 2016.
- [26] E. R. Lippincott, A. Vancalkenburg, C. E. Weir and E. N. Bunting, "Infrared studies on polymorphs of silicon dioxide and germanium dioxide," *J Res Natl Bur Stand (1934)*, vol. 61, no. 1, p. 61, 1958.

- [27] S. H. Xue, H. Xie, H. Ping, Q. C. Li, B. L. Su and Z. Y. Fu, "Induces transformation of amorphous silica to cristobalite on bacterial surfaces," *RSC Adv*, vol. 5, no. 88, pp. 71844-71848, 2015.
- [28] J. R. Michalski, M. D. Kraft, T. Diecrich, T. G. Sharp and P. R. Christensen, "Thermal emission spectroscopy of the silica polymorphs and considerations for remote sensing on Mars," *Geophys Res Lett*, vol. 40, no. 19, 2003.
- [29] P. J. Launer and B. Arkles, "Infrared analysis of organosilicon compounds," in *Silicon Compounds: Silanes and Silicones, 3rd Ed.*, Morrisville, Gelest, Inc., 2013, pp. 175-178.
- [30] L. L. Hench, D. E. Day, W. Höland and V. M. Rheinberger, "Glass and Medicine," *International Journal of Applied Glass Science*, vol. 1, no. 1, pp. 104-117, 2010.
- [31] H. Qu, H. Fu, Z. Han and Y. Sun, "Biomaterials for bone tissue engineering scaffolds: A review," *RSC Advances*, vol. 9, no. 45, pp. 26252-26262, 2019.
- [32] Q. Chen, J. Roether and A. Boccaccini, "Tissue Engineering Scaffolds from Bioactive Glass and Composite Materials," *Topics in Tissue Engineering*, vol. 4, no. 6, pp. 1-27, 2008.
- [33] A. R. Boccaccini, Q. Chen, L. Lefebvre, L. Gremillard and J. Chevalier, "Sintering, crystallisation and biodegradation behaviour of Bioglass-derived glass-ceramics," *Faraday Discussions*, vol. 136, pp. 27-44, 2007.
- [34] J. A. Sanz-Herrera and A. R. Boccaccini, "Modelling bioactivity and degradation of bioactive glass based tissue engineering scaffolds," *International Journal of Solids and Structures*, vol. 48, no. 2, pp. 257-268, 2011.
- [35] Z. Huan and J. Chang, "Effect of sodium carbonate solution on self-setting properties of tricalcium silicate bone cement," *Journal of Biomaterials Applications*, vol. 23, no. 3, pp. 247-262, 2008.
- [36] Z. Huan and J. Chang, "Calcium-phosphate-silicate composite bone cement: self-setting properties and in vitro bioactivity.," *Journal of Materials Science: Materials in Medicine*, vol. 20, no. 4, pp. 833-841, 2009.
- [37] O. Borkiewicz, J. Rakovan and C. L. Cahill, "Time-resolved in situ studies of apatite formation in aqueous solutions," *American Mineralogist*, vol. 95, pp. 1224-1236, 2010.

Chapter Five — Conclusions and Future Work

- [1] L. L. Hench, D. L. Wheeler and D. C. Greenspan, "Molecular Control of Bioactivity in Sol-Gel Glasses," *Journal of Sol-Gel Science and Technology*, vol. 13, pp. 245-250, 1998.
- [2] F. Baino, G. Novjra and C. Vitale-Brovarone, "Bioceramics and Scaffolds: A winning Combination for Tissue engineering," *Frontiers in Bioengineering and Biotechnology*, vol. 3, no. 202, pp. 1-17, 2015.
- [3] J. R. Brown, "Chapter 14: Sodium silicate bonded sand," in *Foseco Ferrous Foundryman's Handbook, Eleventh Edition*, Oxford, UK, Butterworth-Heinemann, 2000, pp. 204-216.
- [4] D. V. Atterton, "The carbon-dioxide process," *AFS Transactions*, vol. 64, pp. 14-18, 1956.
- [5] Y. Owusu, "Physical-chemistry study of sodium silicate as a foundry sand binder," *Advances in Colloid and Interface Science*, vol. 18, no. 1-2, pp. 57-91, 1982.
- [6] B. R. Constanz, "Calcium phosphate cements prepared from silicate solutions". United States of America Patent US6719993B2, 28 April 2000.
- [7] ISO, "ISO 10993-5: Biological evaluation of medical devices — Part 5: Tests for in vitro cytotoxicity," International Organization for Standardization, Geneva, Switzerland, 2009.
- [8] ISO, "ISO 10993-6: Biological evaluation of medical devices — Part 6: Tests for local effects after implantation," International Organization for Standardization, Geneva, Switzerland, 2016.
- [9] ISO, "ISO 10993-9: Biological evaluation of medical devices — Part 9: Framework for identification and quantification of potential degradation products," International Organization for Standardization, Geneva, Switzerland, 2019.

Appendix I — Sodium Silicate Characterisation

- [1] Y. Owusu, “Physical-chemistry study of sodium silicate as a foundry sand binder,” *Advances in Colloid and Interface Science*, vol. 18, no. 1-2, pp. 57-91, 1982.
- [2] R. G. Liptai, “An experimental study of the effects of additives on the collapsibility of carbon dioxide-sodium silicate bonded foundry cores,” Missouri University of Science and Technology, Rolla, MO, 1960.
- [3] J. R. Michalski, M. D. Kraft, T. Diecrich, T. G. Sharp and P. R. Christensen, “Thermal emission spectroscopy of the silica polymorphs and considerations for remote sensing on Mars,” *Geophys Res Lett*, vol. 40, no. 19, 2003.
- [4] P. J. Launer and B. Arkles, “Infrared analysis of organosilicon compounds,” in *Silicon Compounds: Silanes and Silicones, 3rd Ed.*, Morrisville, Gelest, Inc., 2013, pp. 175-178.
- [5] H. -H. Fricke, M. Mattenklott, H. Parlar, A. Hartwig and MAK Commission, “Method for the determination of quartz and cristobalite (Air Monitoring Methods, 2015),” in *The MAK-Collection for Occupational Health and Safety: Annual Thresholds and Classifications for the Workplace*, Heidelberg, Wiley-Verlag GmbH & Co. KGaA, 2016.
- [6] E. R. Lippincott, A. Vancalckenburg, C. E. Weir and E. N. Bunting, “Infrared studies on polymorphs of silicon dioxide and germanium dioxide,” *J Res Natl Bur Stand (1934)*, vol. 61, no. 1, p. 61, 1958.

Appendix II — Fabrication of Specimen Moulds

- [1] Flexbar Machine Corporation, *Reprorubber Brochure REP-0409*, Islandia, NY: Flexbar Machine Corporation, 2017.
- [2] C. M. Guzzo and J. A. Nychka, “Fabrication of a Porous and Formable Ceramic Composite Bone Tissue Scaffold at Ambient Temperature,” *Metallurgical and Materials Transactions A*, Under Review, 2020.

Appendix III — Viability of *in vitro* Immersion Tests

- [1] S. Kashyap, K. Griep and J. Nychka, “Crystallization kinetics, mineralization and crack propagation in partially crystallized bioactive glass 45S5,” *Materials Science and Engineering C*, vol. 31, pp. 762-769, 2011.

Appendix IV — Specimen Surface Area Approximation

- [1] P. Li, C. Ohtsuki, T. Kokubo, K. Nakanishi, N. Soga, T. Nakamura and T. Yamamuro, "Apatite Formation Induced by Silica Gel in a Simulated Body Fluid," *Journal of the American Ceramic Society*, vol. 75, no. 8, pp. 2094-2097, 1992.
- [2] M. Eagleson, Concise Encyclopaedia Chemistry, Berlin, Germany: Walter de Gruyter & CO., 1993, p. 773.

Appendix V — FTIR Characterisation of *in vitro* Residue

- [1] National Institute for Standards and Technology, "Tromethane," in *NIST Chemistry WebBook, SRD 69*, Gaithersburg, MD, U.S. Secretary of Commerce, 2018.
- [2] I. Notingher and et al., "Application of FTIR and Raman spectroscopy to characterisation of bioactive materials and living cells," *Spectroscopy*, vol. 17, no. 2-3, pp. 275-288, 2003.
- [3] O. P. Filho, G. P. Latorre and L. L. Hench, "Effect of crystallization on apatite-layer formation of bioactive glass 45S5," *J Biomed Mater Res*, vol. 30, no. 4, pp. 509-514, 1996.
- [4] Y. Yu, Z. Bacsik and M. Eden, "Contrasting *in vitro* apatite growth from bioactive glass surfaces with that of spontaneous precipitation," *Materials*, vol. 11, no. p, pp. 20-22, 2018.
- [5] National Institute for Standards and Technology, "Sodium bicarbonate," in *NIST Chemistry WebBook, SRD 69*, Gaithersburg, MD, U.S. Secretary of Commerce, 2018.
- [6] National Institute for Standards and Technology, "Sodium chloride," in *NIST Chemistry WebBook, SRD 69*, Gaithersburg, MD, U.S. Secretary of Commerce, 2018.
- [7] National Institute for Standards and Technology, "Sodium sulphate," in *NIST Chemistry WebBook, SRD 69*, Gaithersburg, MD, U.S. Secretary of Commerce, 2018.
- [8] National Institute for Standards and Technology, "Calcium chloride," in *NIST Chemistry WebBook, SRD 69*, Gaithersburg, MD, U.S. Secretary of Commerce, 2018.

Appendix I—Sodium Silicate Characterisation

A1.1 Density Comparison

The density of the (unset) aqueous sodium silicate used in this study ('old-batch') differed from as-received sodium silicate ('new-batch') density due to aging and exposure to CO₂ gas over the course of 5 years. Density of unset sodium silicate was measured by filling 3.0 mL plastic cuvettes (Eppendorf Canada Ltd., Mississauga, ON) with sodium silicate and recording the mass of the sodium silicate with an analytical balance (P-214, Denver Instrument, Bohemia, NY). The unset old-batch sodium silicate density was found to be 1.358 g/cm³, as compared to the new-batch density of 1.315 g/cm³.

The densification of the old-batch sodium silicate is likely due to the initiation of the setting reaction due to exposure to CO₂ gas. When aqueous sodium silicate sets, it densifies as the result of siloxane polymerisation [1]. Though not fully set, the sodium silicate used in this study has likely undergone some degree of siloxane polymerisation, increasing its density and viscosity.

Densities of set sodium silicates were evaluated with nitrogen gas pycnometry. Ten measurements were taken for each specimen; the observed densities of the set sodium silicates were 2.07 g/cm³ and 2.00 g/cm³ for the old-batch sodium silicate and new-batch sodium silicate, respectively. This minor discrepancy may be attributable to uncertainty in measurement, or indicate that the chemical changes that resulted in density changes of the aqueous material have the potential to slightly affect the density of the set material. The mass loss during setting (in ambient conditions: 294 K; 21 °C) of the old-batch sodium silicate was found to be 46.3%, and the mass loss of new-batch sodium silicate was found to be 47.0%.

A1.2 Contact Angle Comparison

The viscosity, surface tension, and wetting behaviour of the sodium silicate used in this work differed from as-received sodium silicate; these differences were quantified by comparing contact angles of each sodium silicate. A manual static sessile drop method was employed; 0.5 mL of each material was dropped from a height of 2 cm onto a borosilicate glass slide (Fisherbrand Microscope Slides, Fisher Scientific Company, Toronto, ON) that had been cleaned with isopropyl alcohol (Fisher Scientific Company; CAS: 67-63-0) and dried prior to analysis. Images of the drops were analysed with ImageJ v1.52q to determine contact angle; two contact angle measurements were averaged for each droplet. A visual comparison of the two sodium silicates is shown in Figure A1-1, and the contact angle measurements are summarised in Table A1-1.



Figure A1-1. Contact angle comparison of the old-batch aqueous sodium silicate used in this study (A) and new-batch as-received sodium silicate (B) on a borosilicate glass substrate.

	Apparent contact angle (θ)	Standard deviation (θ)
Sodium silicate A	67.1	3.5
Sodium silicate B	50.4	6.0

Table A1-1. Contact angle measurements and standard deviation for the old-batch aqueous sodium silicate used in this study (A) and new-batch as-received sodium silicate (B).

The contact angle of the sodium silicate is indicative of key properties that allow it to function appropriately as a binder phase—namely, viscosity and wetting behaviour. The old-batch sodium silicate (A) has sufficient viscosity to maintain uniform distribution throughout the scaffold; however, new-batch sodium silicate (B) is not sufficiently viscous, and instead settles to the bottom of a specimen mould before setting. Additionally, the less viscous new-batch sodium silicate has a significantly shortened manipulation time; the lower viscosity results in a lower diffusion barrier for CO₂ gas, and thus a faster rate of reaction [2].

A1.3 Fourier Transform Infrared Spectroscopy Comparison

To assess if the differences between the unset sodium silicates affected the chemistry of the set material, FTIR was conducted on set specimens of both sodium silicates. As shown in Figure A1-2, peaks are present at similar wavenumbers, but variability in relative peak intensity prevents accurate assessment of chemical differences between the two materials. The peaks present for both materials are nearly identical, indicating that the chemical bonds present in both materials are similarly identical. This similarity is to be expected, as the chemical differences between the two sodium silicates is likely due to concentration and polymerisation, rather than differences in species or bonds. For both batches of sodium silicate, Si–O peaks are present at 470, 580, 880, 1065, and 1230 cm⁻¹, which are attributable to multiple SiO₂ polymorphs, including amorphous silica [3, 4]. The Si–O peak identified at 779 cm⁻¹ is attributable to quartz (SiO₂) [5, 6]. To more accurately assess if there are differences in chemistry, it will be necessary to utilise a different chemical characterisation technique (such as atomic absorption spectroscopy or inductively coupled plasma-optical emission spectroscopy). For further information on future work, refer to Chapter 5.2.

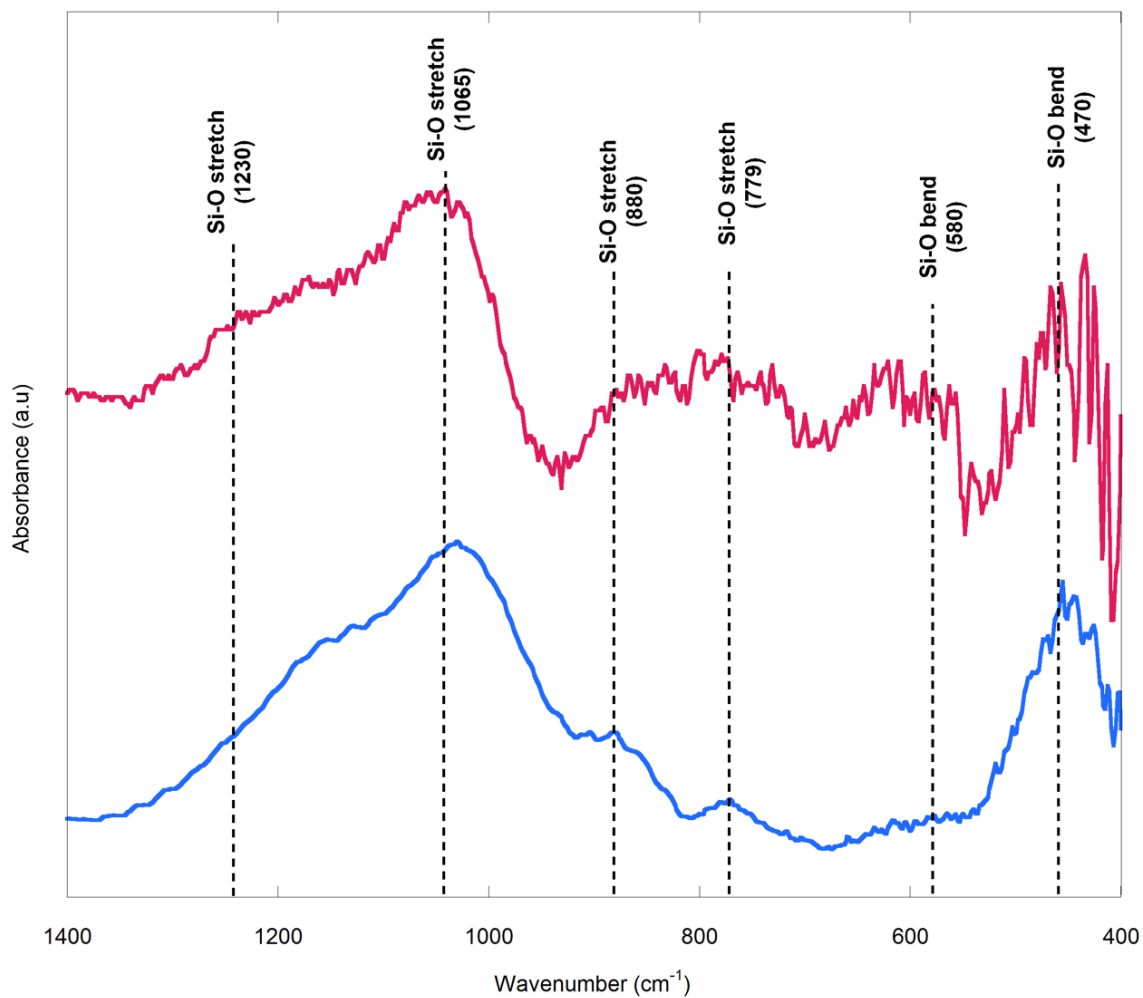


Figure A1-2. FTIR spectra of set old-batch sodium silicate used in this study (blue) and new-batch as-received sodium silicate (red). Peaks were found to be in similar locations, indicating that the bonds present in both batches of sodium silicate are also similar.

Bibliography – Appendix I

- [1] Y. Owusu, “Physical-chemistry study of sodium silicate as a foundry sand binder,” *Advances in Colloid and Interface Science*, vol. 18, no. 1-2, pp. 57-91, 1982.
- [2] R. G. Liptai, “An experimental study of the effects of additives on the collapsibility of carbon dioxide-sodium silicate bonded foundry cores,” Missouri University of Science and Technology, Rolla, MO, 1960.
- [3] J. R. Michalski, M. D. Kraft, T. Diecrich, T. G. Sharp and P. R. Christensen, “Thermal emission spectroscopy of the silica polymorphs and considerations for remote sensing on Mars,” *Geophys Res Lett*, vol. 40, no. 19, 2003.
- [4] P. J. Launer and B. Arkles, “Infrared analysis of organosilicon compounds,” in *Silicon Compounds: Silanes and Silicones, 3rd Ed.*, Morrisville, Gelest, Inc., 2013, pp. 175-178.
- [5] H. -H. Fricke, M. Mattenklott, H. Parlar, A. Hartwig and MAK Commission, “Method for the determination of quartz and cristobalite (Air Monitoring Methods, 2015),” in *The MAK-Collection for Occupational Health and Safety: Annual Thresholds and Classifications for the Workplace*, Heidelberg, Wiley-Verlag GmbH & Co. KGaA, 2016.
- [6] E. R. Lippincott, A. Vancalkenburg, C. E. Weir and E. N. Bunting, “Infrared studies on polymorphs of silicon dioxide and germanium dioxide,” *J Res Natl Bur Stand (1934)*, vol. 61, no. 1, p. 61, 1958.

Appendix II—Fabrication of Specimen Moulds

A2.1 Specimen Mould A

Moulds for the smaller A-type specimens were prepared by using a stainless steel die (11.5 mm diameter) to punch circular wells (resultant 10.3 mm diameter) through a sheet of rubber (2.85 mm thickness), shown in Figure A2-1.

To prepare A-type composite scaffold specimens, the die-punched rubber was placed over a solid sheet of rubber, and composite paste was pressed by hand into the circular wells. Specimens were prepared in batches of 5, and each well was filled with the same mass of paste (as weighed by an analytical balance; P-214, Denver Instrument, Bohemia, NY, USA). A third sheet of rubber was placed atop of the filled wells, and a 2 kg weight was placed over all specimens until demoulding. This process is depicted schematically in Figure 3-3, Chapter 3.2.1.

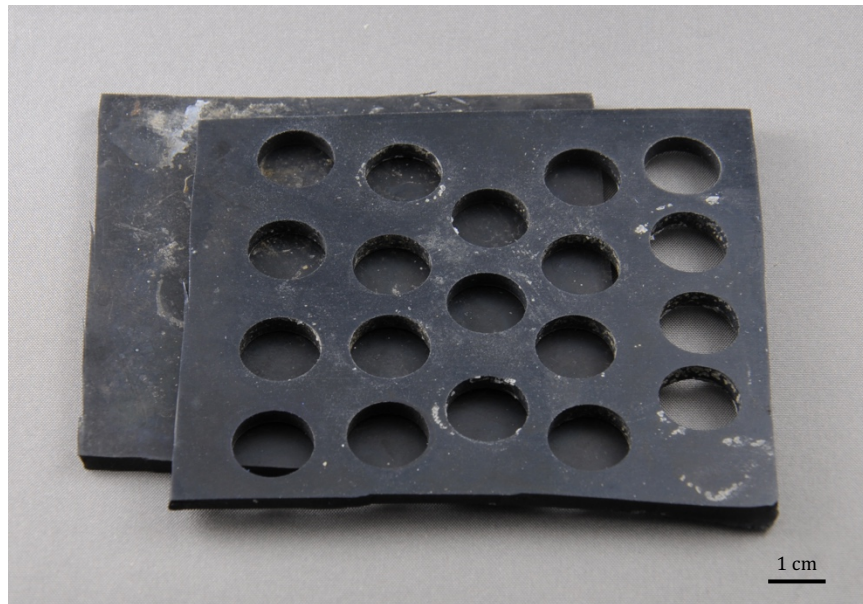


Figure A2-1. Moulds prepared for A-type specimens.

A2.2 Specimen Mould B

Moulds for the larger B-type specimens were prepared using 25 mm diameter mounting cups (Allied High Tech Products Inc., Rancho Dominguez, CA, USA). The base of the 2-part mounting cup was removed, and the mould was placed over a fixed aluminium rod (12 mm diameter) and Teflon block as shown in Figure A2-2.

Dental impression material (3M ESPE Imprint 4 Heavy Body, 3M Canada, London, ON) was used to fill the cavity between the mould and the aluminium rod. Once cured, the aluminium rod was removed, leaving a cylindrical specimen cavity (Figure A2-2). Any moulds with voids along the specimen cavity were discarded. Excess epoxy was trimmed to be flush with the mounting cup, and the depth of the cavity was measured to determine the necessary depth of the compressing piston to create specimens with a height of 27 mm. The mould was removed from the Teflon block and placed on a silicone block until demoulding.

To prepare B-type composite scaffold specimens, the specimen cavity was placed on a Teflon block and filled with the composite paste. The paste was pressed into a custom mould with either a universal materials testing machine (Comprehensive Materials Testing System ME-8244, PASCO scientific, Roseville, CA; modified for constant strain rates through integration of a stepper motor and controller; SureStep 1288 oz-in, Automation Direct, GA, USA) or with a hand-operated drill press (Hausmann Xpert 12" drill press DP1200, Rona Inc., Boucherville, QC; modified with custom 12 mm diameter aluminium piston). A schematic of this process is illustrated in Figure 3-3, Chapter 3.2.1.

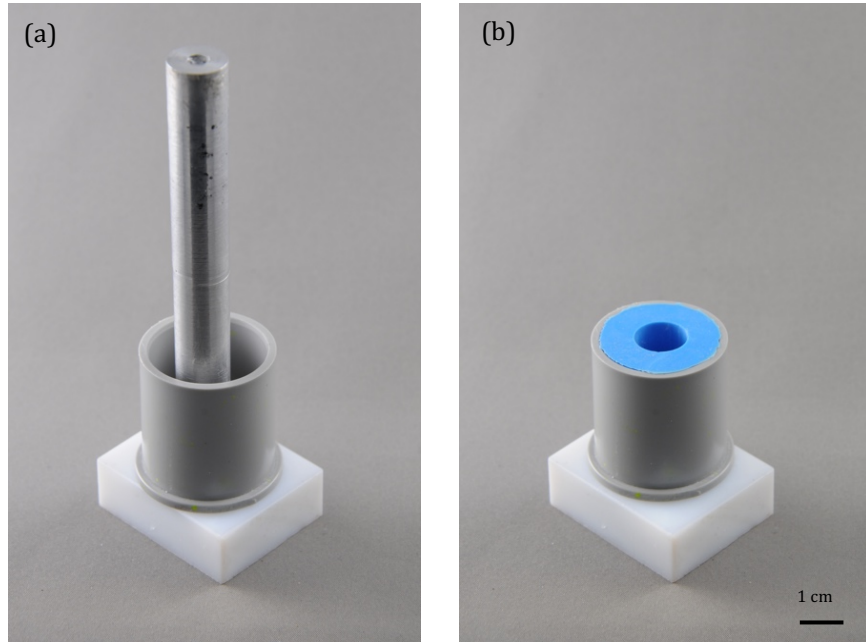


Figure A2-2. Moulds prepared for B-type specimens, showing (a) the components of the mould prior to assembly and (b) the completed mould.

A2.2.1 Choice of VPS Dental Impression Material

Heavy-body vinyl polysiloxane (VPS) dental impression material was chosen for its ability to produce a void-free specimen cavity with high fidelity to the placeholder aluminium rod. Heavy-body VPS has enough elasticity to release specimens without damage, with enough rigidity to resist deformation when the specimen is compressed by the piston. Two VPS dental impression materials (3M ESPE Imprint 4 Heavy Body and EXA'lence Heavy Body Rigid, GC America, Alsip, IL) were tested for their ability to produce a void-free specimen cavity. 3M ESPE Imprint 4 Heavy Body was chosen for its superior performance.

A2.3 Specimen Moulds C and D

Moulds for C- and D-type specimens were fabricated by first preparing a 3-D printed positive mould from PLA filament with a Machina MK2 X20 3D printer (Machina Corp, Edmonton, AB), shown in Figure A2-3a. A negative mould was fabricated by conformally applying Reprorubber putty (Flexbar Machine Company, Islandia, NY) to the positive mould, shown in Figure A2-3b. Reprorubber was chosen for its submicron reproduction resolution (as claimed in technical literature [1]), which allowed for direct comparison was made between the set scaffold geometries and the positive mold geometries.

To prepare C- and D-type specimens, composite paste was pressed by hand into the desired specimen cavity. A sheet of silicone rubber was placed atop the filled cavities, and a 2 kg weight was placed over specimens until de-moulding. De-moulded specimens are shown in Figure 4-6, Chapter 4.3.

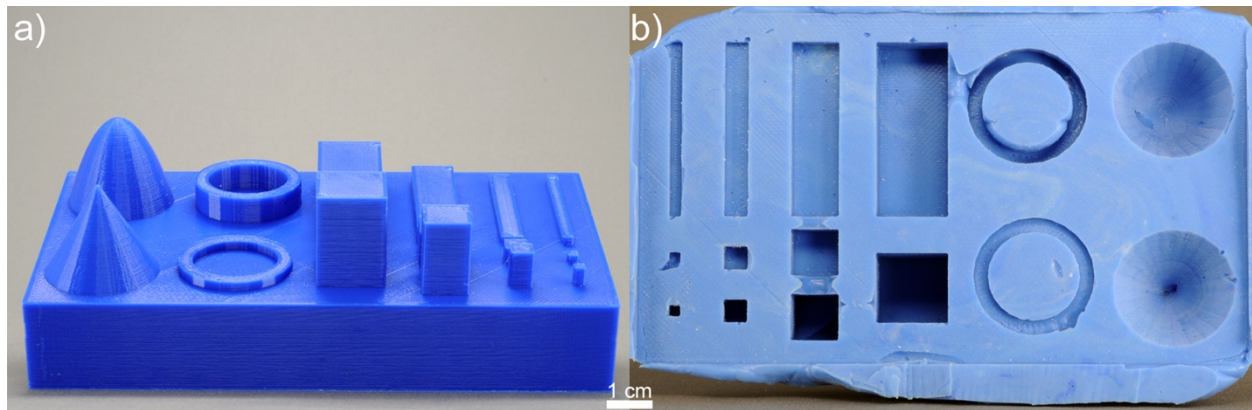


Figure A2-3. (a) Oblique view of 3D-printed original positive mould and (b) plan view of custom Reprorubber negative mould from which positive composite scaffolds were fabricated to assess formability and geometric stability (cone and paraboloid only in this study) [2].

Bibliography – Appendix II

- [1] Flexbar Machine Corporation, *Reprorubber Brochure REP-0409*, Islandia, NY: Flexbar Machine Corporation, 2017.
- [2] C. M. Guzzo and J. A. Nychka, "Fabrication of a Porous and Formable Ceramic Composite Bone Tissue Scaffold at Ambient Temperature," *Metallurgical and Materials Transactions A*, Under Review, 2020.

Appendix III—Viability of *in vitro* Immersion Tests

Monolithic discs of 45S5 bioactive glass and bioactive glass frit control specimens were used to confirm the viability of *in vitro* immersion in simulated body fluid (SBF). Bioactive glass specimens prepared in this manner have been shown to mineralise in *in vitro*, and thus were used as controls [1]. Mineralisation on the surface (polished to 0.5 µm) of bioactive glass discs can be observed with the naked eye, and mineral structures and composition are more readily observed via SEM/EDX on discs than frit. Stereomicrographs of bioactive glass discs are shown in Figure A3-1—it is evident that surface mineralisation is absent on the 7-day specimen, indicating that the used for 7-day specimens was not viable. The temperature of the SBF was not consistently maintained during the addition of reagents, leading to an incorrect amount of Tris(hydroxymethyl)aminomethane added, which culminated in an improperly buffered solution with a different pH than intended. For these reasons, no data from 7-day *in vitro* specimens were included in the analysis. The temperature of the first batch of SBF was measured using only a mercury thermometer (Kessler Thermometer and Chase Instrument, West Babylon, NY), which was not sufficiently precise to maintain an appropriate temperature. In order to more accurately maintain the temperature of the SBF during fabrication, all subsequent batches of SBF were produced using both a digital thermocouple (Fluke 54 II B, Fluke Corporation, Everett, WA) and a temperature probe (Accumet Basic AB15 Plus, Fisher Scientific Company, Toronto, ON).

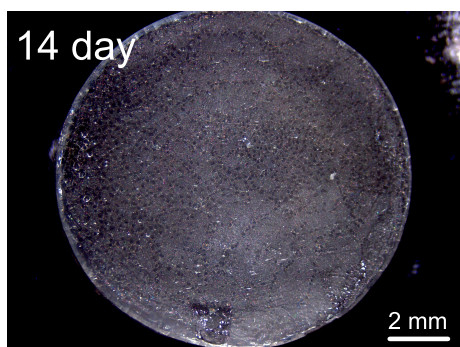
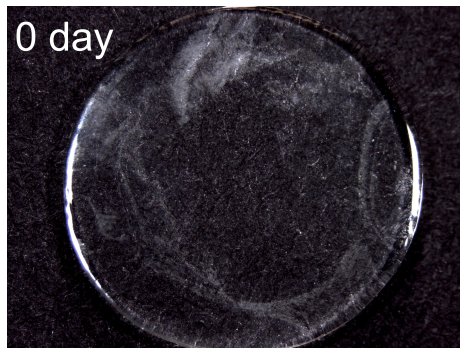


Figure A3-1. Stereomicrographs of 0, 1, 3, 7, and 14-day *in vitro* specimens of monolithic 45S5 bioactive glass, captured on a black paper background. The opacity of the 1, 3, and 14-day specimens is due to the formation of calcium phosphate minerals on the surface. No such mineralisation is observed on the 0-day control specimen, as expected; nor the 7-day specimen, which was immersed in an improperly produced batch of SBF. The 14-day specimen exhibits surface cracking, which likely occurred during drying due to the increased thickness of the mineral layer.

Bibliography – Appendix III

- [1] S. Kashyap, K. Griep and J. Nychka, “Crystallization kinetics, mineralization and crack propagation in partially crystallized bioactive glass 45S5,” *Materials Science and Engineering C*, vol. 31, pp. 762-769, 2011.

Appendix IV—Specimen Surface Area Approximation

The surface area of composite specimens used in *in vitro* immersion tests was approximated to estimate the necessary volume of simulated body fluid (SBF). The composite surface area was calculated as the sum surface area of spherical particles that would occupy a cylinder of equivalent size to the specimen, in the densest packing configuration. A full list of assumptions and limitations is included below.

Volumes of the spherical particles (V_s) and cylindrical specimens (V_c) were calculating using the following equations:

$$V_s = \frac{4}{3} \cdot \pi \cdot r_s^3 \quad (\text{A4.1})$$

$$V_c = \pi \cdot r_c^2 \cdot h \quad (\text{A4.2})$$

Where r_s is the radius of the spherical particles ($r_s = D_{50}/2 = 0.0197$ cm), r_c is the radius of the cylindrical specimen ($r_c = 0.535$ cm) and h is the height of the cylindrical specimen ($h = 0.280$ cm).

The maximum volume of the cylindrical specimen that can be occupied by spherical particles (V_{occ}) is calculated by:

$$V_{occ} = 0.74048 \cdot V_c \quad (\text{A4.3})$$

The number of spherical particles (n_s) of uniform radius that can occupy a cylindrical sample are calculated by:

$$n_s = \frac{V_{occ}}{V_s} \quad (\text{A4.4})$$

The total surface area of the spherical particles (SA_{tot}) was calculated by:

$$SA_{tot} = n_s \cdot SA_s \quad (\text{A4.5})$$

$$SA_s = 4 \cdot \pi \cdot r_s^2 \quad (\text{A4.6})$$

The total approximate surface area of *in vitro* composite samples was calculated to be 15.23 cm². For a SA_{tot}/SBF volume ratio of 0.1 cm⁻¹ [1], it follows that 131.0 mL of SBF is required per composite sample for *in vitro* immersion tests.

Assumptions:

- 1) Only the surface area of the bioactive glass is considered; the effects of the sodium silicate binder matrix are ignored. This may increase the approximated surface area.
- 2) All bioactive glass frit particles are assumed to be spheres, of uniform shape. The diameter of every sphere was assumed to be equal to the D_{50} as measured in imaging particle size analysis (Chapter 4.1.1.2). This may decrease the approximated surface area, as spheres have a lower surface area than the actual, angular frit particles.
- 3) The spherical particles were assumed to have maximum packing density, with a packing factor of 0.74 [2]. The maximum packing factor was chosen as the specimens are compressed before setting, increasing packing.
- 4) The effect of contact between frit particles was ignored. This contact may increase the approximated surface area.

Bibliography – Appendix IV

- [1] P. Li, C. Ohtsuki, T. Kokubo, K. Nakanishi, N. Soga, T. Nakamura and T. Yamamuro, "Apatite Formation Induced by Silica Gel in a Simulated Body Fluid," *Journal of the American Ceramic Society*, vol. 75, no. 8, pp. 2094-2097, 1992.
- [2] M. Eagleson, *Concise Encyclopaedia Chemistry*, Berlin, Germany: Walter de Gruyter & CO., 1993, p. 773.

Appendix V—FTIR Characterisation of *in vitro* Residue

FTIR characterisation was used to identify the nature of the gel residue formed by sodium silicate control specimens and high-binder phase composites. FTIR was conducted on all specimens that deposited sufficient residue material for analysis. Resultant spectra were found to contain many of the bonds present in simulated body fluid (SBF) species, such as NaCl, CaCl₂, NaSO₄, NaHCO₃, or K₂HPO₄·3H₂O. The presence of SBF species is likely due to the fact that the residue could not be washed with deionised ultra-filtered water (DIUF) as thoroughly as the specimens, as the small amount of residue present would be removed by the DIUF. Instead, a small amount of DIUF was added to the drained petri dishes, gently swirled around the residue, and then poured off slowly so as not to remove the residue material. The washed residue was then allowed to dry in a fume hood overnight in the petri dish, after which it was scraped off.

The amount of residue present in both the petri dishes and in the intergranular spaces of composite specimens was positively correlated with binder amount. Though the visual characteristics of the residue indicate that it is likely binder phase—both the dried sodium silicate control and the residue were weakly consolidated, semi-translucent gels when hydrated, and fine white powders when dried—FTIR was conducted to assist in confirming this supposition. However, the overwhelming presence of SBF constituents in the FTIR spectra obscure the exact chemical nature of the residue; for instance, P-O and C-O bonds could be from either SBF or from biomineralisation (Figure A5-1), and some spectra were entirely dominated by the characteristic peaks of Tris(hydroxymethyl)aminomethane-HCl (hydrochloric acid) buffer (Figure A5-2) [1]. The infiltration of SBF species into the hydrated binder gel has been observed via XRD (Chapter 4.6.3), and thus it is likely that SBF species are also present in the gel residue, unable to be parsed from biominerals via FTIR characterisation alone. For these reasons, FTIR analysis was not used to identify the chemical nature of the *in vitro* residue material. In order to more accurately assess the chemistry of the residue, a different chemical analysis technique, such as inductively coupled plasma-

optical emission spectroscopy (ICP-OES) or atomic absorption spectroscopy (AAS), may yield more informative results.

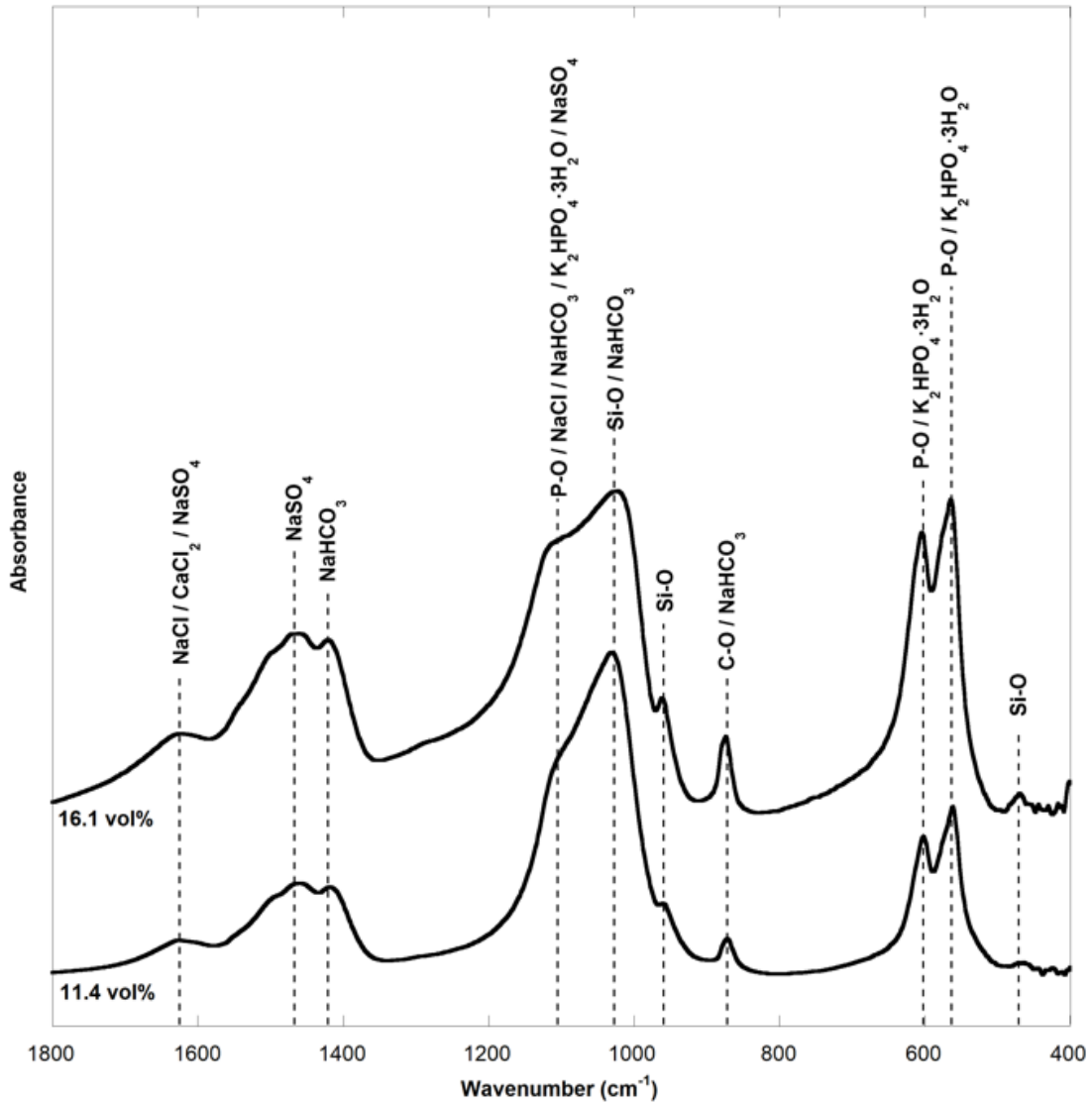


Figure A5-1. FTIR spectra of residue obtained from 11.4 and 16.1 vol% composite specimens after 14 days *in vitro* immersion. Peaks that may be attributable to the composite material and the formation of biominerals are shown as bonds (i.e., P-O, C-O, Si-O¹ [2, 3, 4]); however, the presence of numerous peaks also attributable to SBF constituents (i.e., NaCl, CaCl₂, NaSO₄, NaHCO₃, K₂HPO₄·3H₂O [5, 6, 7, 8]) renders these signals inconclusive. An insufficient amount of residue for FTIR analysis was present for the 7.4 vol% specimen after 14 days *in vitro*.

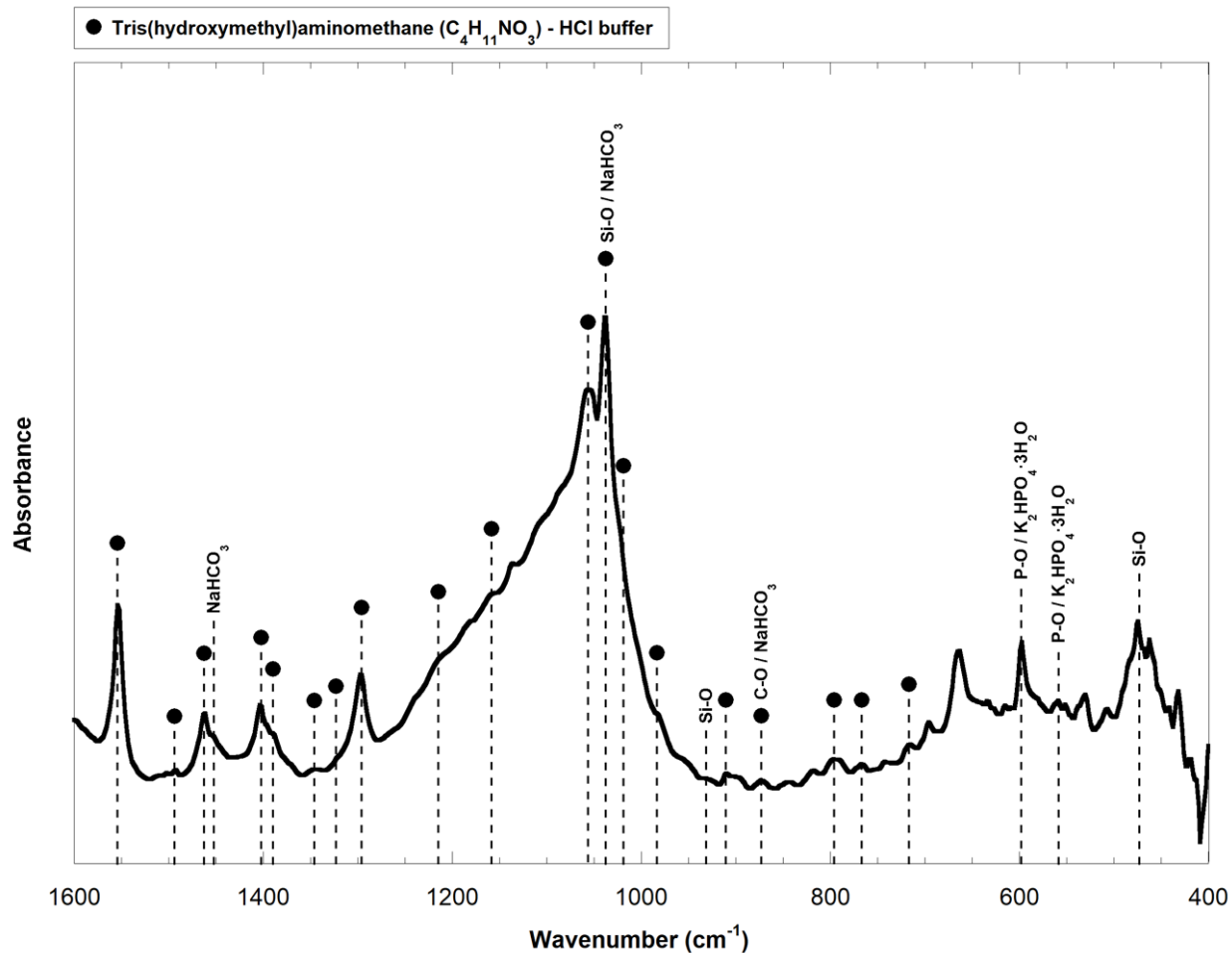


Figure A5-2. FTIR spectra of residue obtained from 11.4 vol% specimen after 3 days *in vitro* immersion. As indicated by the black dots, much of the spectra can be attributed to the presence of Tris(hydroxymethyl)aminomethane-HCl buffer, which was used in the fabrication of SBF. Additionally, peaks that may be attributed to other species present in SBF, such as sodium bicarbonate (NaHCO_3) and dipotassium phosphate-trihydrate ($\text{K}_2\text{HPO}_4 \cdot 3\text{H}_2\text{O}$), are not distinguishable amid the Tris-HCl signal. The location of peaks that may be attributable to bonds present in the mineralised composite (P-O and Si-O) are indicated on the spectra, but again, cannot be parsed from the SBF species present in the residue. For these reasons, FTIR was not considered a reliable means to assess the chemical nature of the residue present in petri dishes after *in vitro* immersion.

Bibliography – Appendix V

- [1] National Institute for Standards and Technology, “Tromethane,” in *NIST Chemistry WebBook, SRD 69*, Gaithersburg, MD, U.S. Secretary of Commerce, 2018.
- [2] I. Notingher and et al., “Application of FTIR and Raman spectroscopy to characterisation of bioactive materials and living cells,” *Spectroscopy*, vol. 17, no. 2-3, pp. 275-288, 2003.
- [3] O. P. Filho, G. P. Latorre and L. L. Hench, “Effect of crystallization on apatite-layer formation of bioactive glass 45S5,” *J Biomed Mater Res*, vol. 30, no. 4, pp. 509-514, 1996.
- [4] Y. Yu, Z. Bacsik and M. Eden, “Contrasting in vitro apatite growth from bioactive glass surfaces with that of spontaneous precipitation,” *Materials*, vol. 11, no. p, pp. 20-22, 2018.
- [5] National Institute for Standards and Technology, “Sodium bicarbonate,” in *NIST Chemistry WebBook, SRD 69*, Gaithersburg, MD, U.S. Secretary of Commerce, 2018.
- [6] National Institute for Standards and Technology, “Sodium chloride,” in *NIST Chemistry WebBook, SRD 69*, Gaithersburg, MD, U.S. Secretary of Commerce, 2018.
- [7] National Institute for Standards and Technology, “Sodium sulphate,” in *NIST Chemistry WebBook, SRD 69*, Gaithersburg, MD, U.S. Secretary of Commerce, 2018.
- [8] National Institute for Standards and Technology, “Calcium chloride,” in *NIST Chemistry WebBook, SRD 69*, Gaithersburg, MD, U.S. Secretary of Commerce, 2018.